Master thesis and internship[BR]- Master's thesis : Study of the optical design of an elementary spacebased interferometer for the detection and characterisation of exoplanets[BR]- Integration internship

Auteur : Thiry, Eliott
Promoteur(s) : Loicq, Jerome
Faculté : Faculté des Sciences appliquées
Diplôme : Master en ingénieur civil en aérospatiale, à finalité spécialisée en "aerospace engineering"
Année académique : 2020-2021
URI/URL : http://hdl.handle.net/2268.2/11720

Study of the optical design of an elementary spacebased interferometer for the detection and characterisation of exoplanets

University of Liège - School of Engineering and Computer Science

Master Thesis presented with the objective to acquire the degree of Master of Science in Aerospace Engineering specialised in Satellite and Space Optics Engineering.

Eliott Thiry

Professor
Pr. Jérôme Loicq

Assistant
Colin Dandumont

Research Centre
CSL - Centre Spatial de Liège

Academic year
2020 - 2021

Table of Contents

List of Figures

List of Tables

Abstract

This master thesis is dedicated to the optical design of an elementary spacebased interferometer for the detection and characterisation of exoplanets. More precisely, this work proposes a Bracewell-type interferometer design allowing light reduction and collimation with the use of two telescopes composed of two 45° off-axis afocal parabolic mirrors. This design aims at minimising the number of optical surfaces required to perform interferometric measurements as well as the complexity of the design in order to maximise the compactness and decrease the development costs. The sensitivity of this system to telescope pointing errors is investigated. The beam propagation deviations are corrected by a tip-tilt mirror. The position of this tip-tilt mirror is optimised to minimise the transverse shift of the beams induced after reflection. The use of a single mode fibre as modal filtering reduces the sensitivity of the system to wavefront distortions. However, the final design presents a variation in optical path length for the rays entering the entrance pupil at its extremities, namely the sagittal and meridional rays. Theses rays experience an optical path variation (with respect to the chief ray) proportional to $\pm 1.74\alpha$, where α is the ray field angle in degrees with respect to the line of sight incident on the telescope. Thus, given the current capabilities of deformable mirrors which are able to perform a maximum stroke of ~ 15 μm (compensating therefore about 30 μm of maximum wavefront distortion), this limits the telescope pointing accuracy to 0.02 degrees. Considering the capabilities of current attitude determination and control systems as well as pointing sensors precision this seems to be a totally achievable accuracy without significant costs increase. Finally, options for adapting the design to manage higher error field angles are proposed.

Key Words: Interferometry, pointing error, Zernike polynomial, single mode fibre.

Acknowledgement

First and foremost, I want to express my gratitude to Jérôme Loicq, the supervisor of my master thesis. His excellent advices and his benevolence during the entire development of this study have greatly contributed to its final outcome.

I am also deeply grateful to my co-supervisor Colin Dandumont, for his investment and his wise comments which guided my steps towards the completion of this work. His large bibliographic collection has also been of great help to me.

I warmly welcome the help, participation and psychological support of three students who are now my friends and with whom I have had the opportunity to work, study, and live. Armand Dubuc, Casimir Fayt, and Hadrien Delatte, you are each exceptional people and have the competence to do great things. I wish you from the bottom of my heart good luck in your future projects.

I would also like to thank the staff of the Centre Spatial de Liège (CSL) and especially Alexandra Mazolli and Victor Laborde for their voluntary help mainly on the use of the CodeV software.

These 5 months of work would not have been this productive without the support of the family, and I would like to thank them very much, especially my sister and my parents who have always believed in my abilities and who have always supported me in my choices. If I am here today, it is mainly thanks to all three of you.

To conclude, I would like to tenderly embrace Aline who has never ceased to be a valuable source of positive energy during these 2 years of Master here in Liège. Her cheerfulness and her smile were with me all along.

Preambule

This work is a continuation from previously conducted researches on the use of nulling interferometry as a technology for the detection and characterisation of exoplanets. These investigations are taking place within the framework of the SCIFY (Self-Calibrated Interferometry For exoplanet spectroscopY) project, which has as an ultimate goal the implementation of *Hi-5*[1], a high-contrast nulling interferometer in the thermal infrared (3.8 μm), on the VLTI (Very Large Telescope Interferometer).

This master thesis consists therefore in one of the first development steps of the SCIFY project and aims at reinforcing the knowledge on the capabilities and the performance of nulling interferometry when previously implemented on reduced scale designs (PROBA type). As a matter of fact, the main goal is to obtain useful scientific results at low cost and with minimum complexity.

This study is thus built on previous work carried out by the core members of the SCIFY project[2] in collaboration with the Centre Spatial de Liège (CSL) and extends the analysis of the Bracewell interferometer as a first approach to perform interferometric measurements on extrasolar systems.

More particularly, in this work I will first briefly discuss the principal methods used for detecting exoplanets. Then, in Chapter 2, I will discuss more extensively the basic principles of nulling interferometry. In particular, I will outline the main components of Bracewell's system as well as its instrumental performance and limitations. In Chapter 3, I will address several space missions and projects that have also relied on nulling interferometry. The strengths and weaknesses of these studies will be used to guide the design choices for the subsequent development of the optical system of this master thesis. The different stages of the telescope design will be presented in Chapter 4, giving the initial decisions made on the observing wavelengths and satellite dimensions. The functional aspects of the design will also be studied on the basis of the throughput which has been identified as one of the most critical parameters of the system. Thus, the initial capabilities of the telescope are introduced before being discussed in more detail in the following chapter with the benefit of the ray tracing software CodeV. The impact of pointing errors on the beam propagation will be analysed, giving therefore the type of adaptive optics that might be required for stable observations. Chapter 6 is dedicated to the optimisation of the design in order to reach the best possible performance. Finally, the limitations of the system will also be highlighted in order to define the elements that still need to be studied to improve the ultimate capabilities of the interferometer.

[1] http://www.biosignatures.ulg.ac.be/ddefrere/hi5.php
[2] https://fys.kuleuven.be/ster/research-projects/scify/scify

Chapter 1

General Introduction

The understanding of Earth's surrounding universe is a recent concept. Even nowadays, with a significant amount of knowledge acquired about subjects such as planets and stars' movements, composition, life and death, we still have a vast amount of questions that haven't been answered. One of these is related to the possible existence of other habitable planets. Human investigations related to extraterrestrial life discovery have started way before the 21st century. Christian Huygens, in the 17th century, was one of the first astronomers to consider the use of observational instruments to detect planets revolving around other stars. A first attempt to search for clues was made by the Viking space probe sent by NASA to the surface of the red planet in 1975 [1]. But until the early 1990s, despite numerous attempts, no observations could be made mainly because of the insufficient technological capabilities. The first confirmed exoplanet discovery occurred in 1992 thanks to *A. Wolszczan* and *D. A. Frail* observations [2] of millisecond pulsar PSR1257. However, the first extrasolar planet around a main-sequence star, 51 Pegasi b, was discovered by *M. Mayor & D. Queloz* in 1995 [3]. In the following years, observations increased, mainly thanks to the advent of the Kepler space telescope launched in 2009. It carries out a systematic census of the planets present in a small portion of the sky, less than 2 000 light-years away, using the transit method [4]. Real progress has thus only been made in the recent decades with the development of space telescopes and missions toward deep space. Humanity's desire to discover and explore has always been present and it is only thanks to the latest technological advancement that we are now able to push our understanding of new systems to the next level.

1.1 Exoplanets detection methods

Before settling down on another planet, consequent observations have to be made to gather enough data that can be used to determine the planet's temperature, atmosphere, chemical composition,...etc. We have already done this for Mars and other planets of our solar system, but the conclusion was never really in favour of life development as we know it here on Earth.

Therefore, scientists turned their studies toward further horizons. The identification of planets around a star is not an easy task and characterising the star's revolving planets is even more difficult. However, several detection methods have been developed in order to locate these exoplanets. Some of the most effective ones are summarised here after and separated between indirect and direct detection techniques.

1.1.1 Indirect detection technique

Such type of detection is related to the observation of several external phenomenons caused by the presence of an exoplanet in its surrounding environment. These impacts can be luminosity variations or light path deviation due to the gravitational field. Indirect detection is more used than direct observation since the latter implies that the observed planet has to be first, close to its star, and secondly, big enough such that a sufficient photon flux variation can be detected. Moreover, an excellent angular resolution, as well as an efficient technology for the planet radiation flux extraction, are required for direct observation. Nowadays, mainly four indirect methods have been proven to be effective [5].

Radial velocity

The radial velocity method, also known as Doppler spectroscopy, is based on the observation of the star spectrum of emission. It is assumed that an object orbiting the star will affect the star movement and cause it to rotate around the system's centre of mass. This slight movement of the star can be revealed by extremely sensitive spectrographs. The consequence of such periodical oscillations translates into a regular red-shift when the star moves away from the observer and a blue-shift of the spectrum in the opposite case as illustrated in Figure 1.1. This is a direct consequence of the Doppler effect, which describes the change in the perceived frequency of a wave as the distance between the transmitter and receiver varies over time. A reduction of that distance will cause the light observed to shift to shorter wavelengths (contraction of the oscillation period), which is called a blue shift because of its higher emission frequency. Such variation in brightness gives information about the speed of displacement of the object in orbit and if its deduced mass is small enough ($\leq 10 M_{Jup}$), then it is eventually called a planet [6].

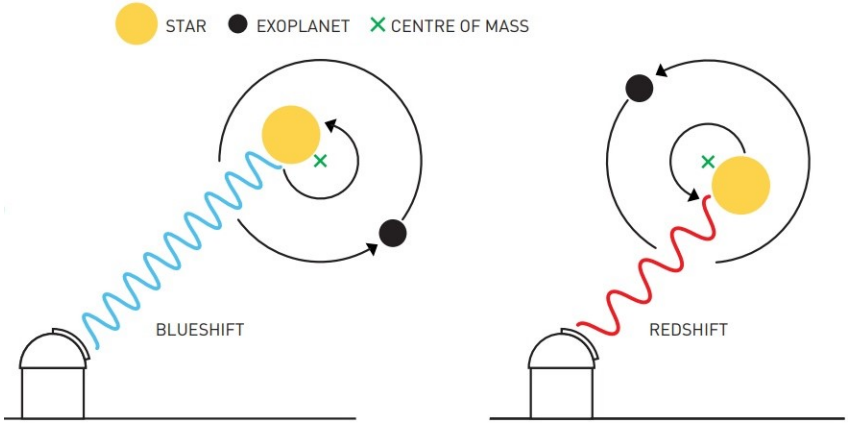

Figure 1.1: Radial velocity illustration [7].

Mathematically, the radial velocity semi-amplitude K_* of the star can be expressed in units of cms^{-1} with the planet mass in units of $M_\oplus$ and is given by [8]

$$K_* = \frac{8.95 \text{ cm s}^{-1}}{\sqrt{1-e^2}} \frac{M_P \sin i}{M_\oplus} \left(\frac{M_* + M_P}{M_\odot}\right)^{-2/3} \left(\frac{P}{yr}\right)^{-1/3}. \tag{1.1}$$

The velocity semi-amplitude K_*, the orbital period P and the eccentricity e are the observed parameters used to calculate a minimum mass of the planet $M_P . \sin i$ considering that the mass

of the star M_* is known and that i represents the orbital inclination of the planet-star system with respect to the observer.

Therefore, it does not provide a true value of the mass of the planet (M_P) since the star's movement with respect to the observer depends on the orbital plane inclination angle i which is often not known precisely. Therefore, the results from radial detection have to be considered very carefully before affirming the presence of a planet.

Notable observatories where this method is used are the Keck Telescope in Hawaii and the La Silla Observatory in Chile. Radial velocity measurement was the first successful way to find exoplanets and continues to be one of the most productive methods with more than 842 planets already discovered (from [5],20 May 2021).

Transit photometry

This is the most effective method for locating extrasolar planets according to existing technology. It is based on the simple fact that when a planet crosses the line of sight between the observer and the star, the light received by the observer is dimmed. The passage of a planet between its star and the Earth is called a "transit". If the light attenuation incurred lasts for a fixed amount of time and periodically occurs then it is very likely that a planet has been detected. The advantage of such an observation technique is that the approximate size of the planet can be deduced from the level of light mitigation. Transit photometry is therefore an excellent complement to radial velocity detection to retrieve the mass and size of a planet [5][9].

Moreover, further information can be obtained from transit detection. The light from the star passing through the hypothetical planet's atmosphere is strongly or poorly absorbed at different wavelengths which can be related to the presence of particular elements. By monitoring the depth of transit at various wavelengths scientists are able to deduce the atmosphere's composition as well as the complete stellar spectrum of emission.

The *a-priori* probability of a planet to be observed in transit is a function of the planet and star radii as well as the planetary orbit. The formula, expressed in [8], is

$$P_{tr} = 0.0045 \left(\frac{\mathrm{AU}}{a}\right) \left(\frac{R_* + R_P}{R_\odot}\right) \left[\frac{1 + e\cos(\pi/2 - \omega)}{1 - e^2}\right], \tag{1.2}$$

where ω is the angle at which periastron occurs such that $\omega = 90°$ indicates transit, and e represents the orbital eccentricity of the planet.

The drawback of this method is that it requires an almost perfect alignment of the planet's orbital plane with the line of sight, which is a very rare configuration. Furthermore, the orbital period of a planet can last up to a few years, rendering the number of transits even more scarce. For instance an Earth-sized planet in an Earth-like orbit around a solar-type star has a transit probability according to Equation1.2 $P_{tr} = 0.0046$ ($\sim 0.5\%$). And since for robust analysis a lot of data needs to be gathered, this requires observing a system during extended periods. Nonetheless, more than 3325 exoplanets have currently been detected with this method and more than 2000 other candidates have been identified and are waiting for confirmation ([10], 10 May 2021). Most of the telescopes working with this method are ground-based such as the two telescopes of TRAPPIST, the 7 telescopes of HATNet, the 2 telescopes of the MEarth project, and the forthcoming 4-telescope SPECULOOS survey which is a project led, among others, by the University of Liège. Kepler and CoRoT are an example of two satellites that greatly

participated in the search for exoplanets via the transit method [4][11]. They were succeeded by the Transiting Exoplanet Survey Satellite (TESS), which has been surveying for new planets since 2018, and the Characterising Exoplanet Satellite (CHEOPS), which was launched in December 2019.

Gravitational microlensing

This technique complements the first two as it is the only one capable of detecting exoplanets at truly large distances. While radial velocity and transit methods can observe our galactic neighbourhood up to a hundred light-years, gravitational lensing can push the observations up to thousands of light years, reaching a star closer to the galactic centre or within other galaxies. This is because it uses the effect of gravity on the light path instead of the two previously cited methods which rely on detecting light intensity variations from the target star. The process is depicted in Figure 1.2.

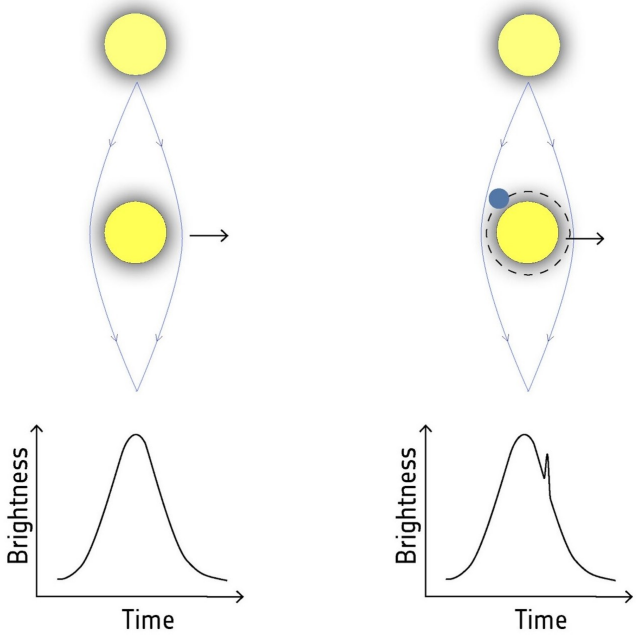

Figure 1.2: Illustration of the microlensing detection process [12].

This method was predicted by Albert Einstein in his general theory of relativity. It is based on the fact that massive objects can bend the light around them. Therefore when a star crosses the line of sight between the observer and the background distant star, the light travelling towards the observer is deviated by this travelling body which acts as a lens. The background light is brought to a focus by the closest star making the farthest one appear brighter. Eventually, if the forefront star hosts a planet, a brief blip of brightness from the lensing action of this planet can be detected by optical instruments. The first microlensed planet was revealed in 2004 [13]. This technique is still used nowadays as it is extremely sensitive and can detect very small planets. However, it has a very low probability of occurrence due to the precise geometrical alignment required and the singularity and non-repeatability of the event.

Astrometry

Astrometry relies on the observation of a star apparent position in the sky with respect to other stars. This star wobble, eventually caused by the presence of a planet, is extremely difficult to detect and this is the reason why only one planet has been discovered by this method. To track this movement, a series of images of the star and surrounding stars are taken, allowing later computation of their relatives distances and therefore deduction of the target star movement. The detection principle is based, as for radial velocities, on the relative motion of the star with respect to its surroundings, except that here we are interested in the star displacement in the image plane rather than in its perceived variation of the light spectrum.

1.1.2 Direct detection technique

Direct imaging is based on the straight observation of spatially resolved host stars and their orbiting planets. It is a powerful complement to the previously discussed techniques. It is primarily sensitive to planets with wide orbits (> 5 AU) and allows spectroscopic or photometric characterisation of the atmosphere by analysing the energy of the directly recorded photons [8].

Coronography

Although direct imaging of stars permitted the detection of 53 exoplanets [5], this technique is constantly confronted with the same issue: the host star is millions of times brighter than its planet. For instance, the Sun apparent magnitude is $m_V = -26.74$ whereas the magnitude of an Earth-like planet at a distance of 1 AU from the Earth and the Sun would have an apparent magnitude $m_V = -3.99$ [14]. This makes à luminosity ratio of $\sim 10^9$. Therefore, the faint source of light reflected by the planet is drowned out by the massive amount of radiation emanating from the star. One solution to this recurring problem is to block the light of the star. This can be done by coronography where the starlight is blocked inside the telescope assembly before reaching the detector. Similar concepts are based on "starshades" which are devices positioned in front of the telescope to prevent the light from the star to enter it. For space-based telescopes, starshades consist of an additional spacecraft designed to position itself at the right distance and angle from the telescope to block the starlight.

Interferometry

Another technique used to get rid of the excessive stellar radiation is to use interferometry. Interferometric measurement relies on the wave-like properties of light to superimpose electromagnetic radiations and produce an interference pattern that can be analysed. If designed correctly, the starlight can be positioned onto a dark fringe of the interference pattern, whereas the light coming from the planet is placed on a bright one, increasing therefore the contrast between the two. This method, called "nulling interferometry", is the one considered in this master thesis and is more extensively discussed in the following chapter.

Chapter 2

Concept of Interferometry

2.1 Diffraction property of light

The phenomenon of diffraction, caused by the dual wave-particle properties of light, relates to the interaction of a wavefront with something in its path and the description of how it propagates following that interaction. Since every imaging optical systems have finite aperture dimensions, the image of a point source will therefore not be a point but rather a figure of diffraction (with potential aberrations degrading this figure). As a matter of fact, the focalisation of a light beam passing through a circular aperture will give rise to an Airy pattern such as in Figure 2.1a with a radius

$$R_{Airy} = 1.22\frac{\lambda f}{D}$$

where D corresponds to the aperture diameter, f the focal length and λ the observed wavelength. Therefore, the larger the telescope's diameter the smaller the Airy disk and the higher the ability to distinguish small object features. This is described by the Rayleigh criterion which says that an imaging process is diffraction-limited when the first diffraction minimum of the image of one source point coincides with the maximum of another. Such a conclusion explains why we keep going toward larger and larger telescopes such as the E-ELT (European Extremely Large Telescope) project.

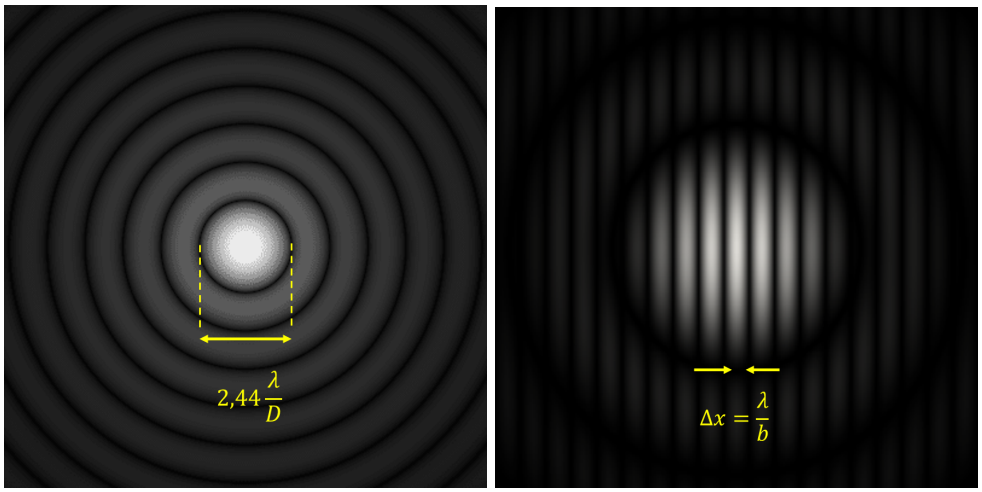

(a) Airy disk pattern for aperture diameter D (b) Fringe pattern for baseline length b

Figure 2.1: Patterns of interference for single and double telescopes with circular apertures [15].

In astronomy, the minimum angular resolution of a telescope is linked to this Airy disk dimension by the relation

$$\theta = 1.22\frac{\lambda}{D}. \tag{2.1}$$

For a 2 telescopes interferometer, the diffraction pattern caused by the coherent recombination of the light is illustrated on Figure 2.1b and the Equation 2.1 becomes

$$\theta = \frac{\lambda}{2b} \tag{2.2}$$

where b is the baseline length of the interferometer (which is the separation of the primary mirrors). The interference pattern is a set of periodical alternations between rectilinear bright and dark fringes with angular spacing λ/b modulating the Airy disk pattern. This interference structure is analogous to the one obtained by Young in its double-slit experiment where the bright and dark fringes are characterised by optical path differences between the two beams, which directly depends on the separation of the slits.

2.1.1 Fringes contrast

The contrast between fringes depends on the angular size of the object as well as on the separation between the two telescopes, as stated by Equation 2.2. The longer the baseline, the smaller the fringe spacing and the fainter the resolvable details. The fringe contrast progressively fades away until coherence is lost at $\theta = \lambda/2b$ as described by the Rayleigh criterion. This means the object angular size is equal to the size of the Airy disk as illustrated by Figure 2.2.

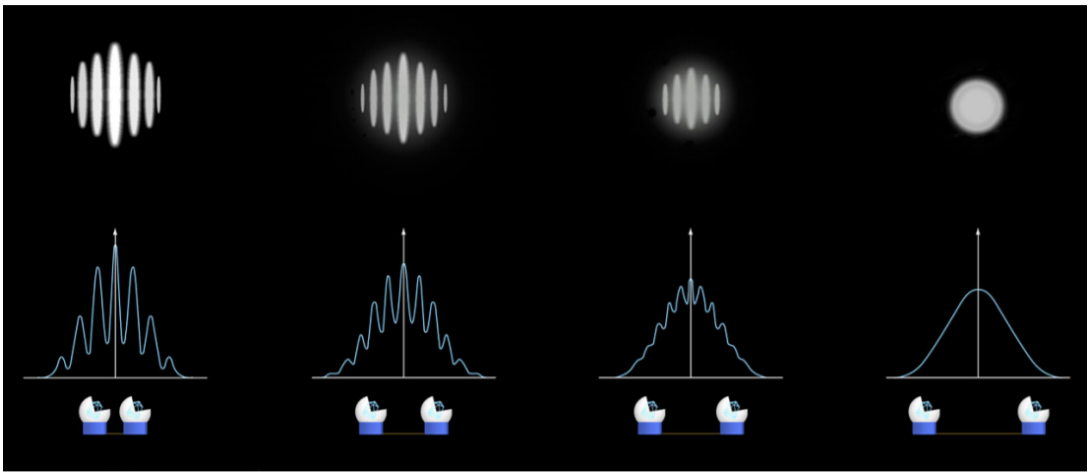

Figure 2.2: Coherence evolution with baseline length [15].

In interferometry it is convenient to define a metric that evaluates the quality of a fringe pattern. Mathematically, the contrast between destructive and constructive fringes is quantified through the concept of visibility where

$$V = \frac{I_{max} - I_{min}}{I_{max} + I_{min}}. \tag{2.3}$$

From this equation it is easy to see that $0 \leq V \leq 1$ with values closer to one corresponding to a higher contrast. For circular objects this visibility can be expressed

$$V = \frac{2J_1(\pi\theta b/\lambda)}{\pi\theta B/\lambda} \tag{2.4}$$

where J_1 is a Bessel function of order one [16].

2.2 Bracewell interferometer

The simplest structure for an interferometer requires two different beams to be collected. Their recombination then allows the production of the interference pattern shown previously. However, if the light paths are identical between the two beams (from both telescopes apertures to the detector), the resulting fringe pattern will produce constructive interference at the focal plane centre. Since we are interested in the planet electromagnetic emission, it is a necessity to get rid of the excess starlight. This nulling interferometry technique, schematically represented in Figure 2.3, was first proposed by Bracewell in a letter to Nature in 1978 [17]. It consists of two telescopes pointing toward the same direction (the star) whose signals are recombined to produce destructive interference for the on-axis target. This is achieved by introducing an achromatic π phase shift in one of the two arms, resulting in an interference pattern where the central fringe corresponds thus to a destructive process.

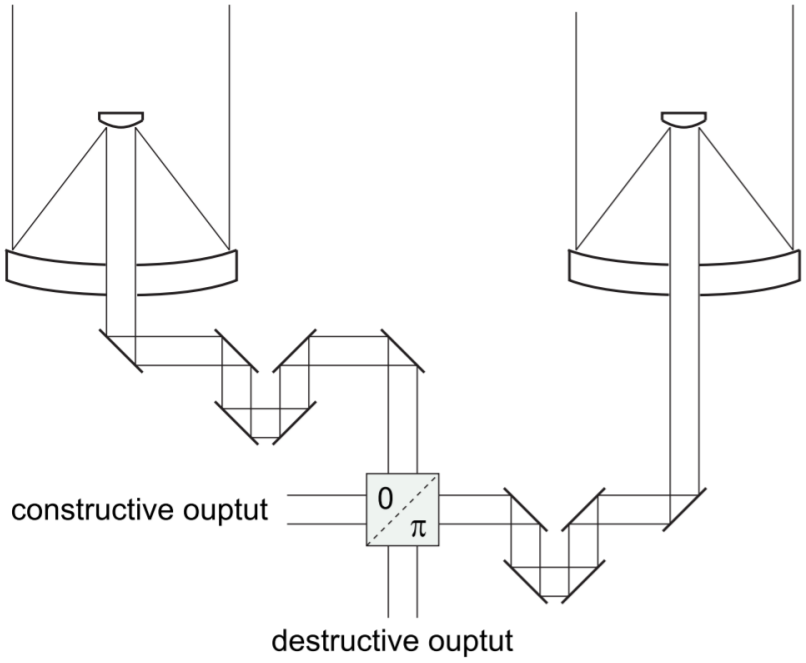

Figure 2.3: Bracewell nulling interferometer representation [18].

By this mean, the star photon flux can be significantly reduced. The closer to this phase inversion, the darker the central fringe and the higher the contrast between the star and its companion. The latter is expected to fall exactly on a constructive interference fringe. But since the position of the planet orbiting the star is unknown, its signal could end up on a dark fringe and therefore not be detected. In addition, other light sources in the field of view create background noise that interferes with the study of the observed system. To overcome this problem Bracewell added the possibility to rotate the interferometer. As a matter of fact, this allows the observation of planets that would have initially ended up on a dark fringe since the satellite rotation will make the off-axis planet move across bright and dark regions periodically. This converts into a modulated signal intensity variation that can be recorded and associated with the presence of a planet with a specific size and semi-major axis as illustrated in Figure 2.4.

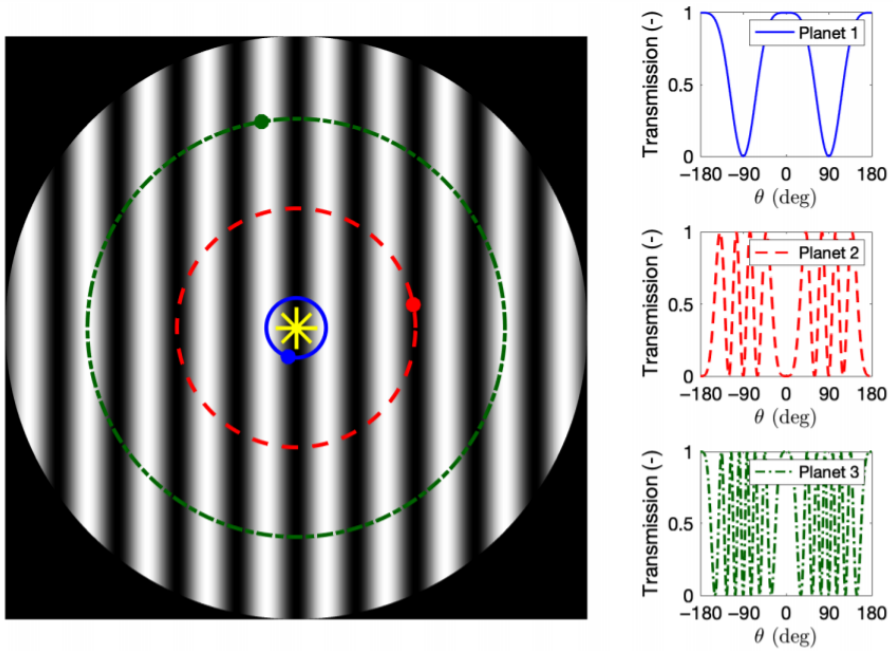

Figure 2.4: Modulation of the planet signal thanks to the rotation of the nulling interferometer [19].

2.2.1 Beam combination

Stellar light is always emitted on the entire spectral range making it poly-chromatic (associated with a black body). Therefore, the interference pattern will be affected by the different light frequencies such that constructive and destructive interferences do not occur anymore on the same spots. This results in a decrease of the contrast between the bright and dark fringes and therefore a reduction of the visibility (Equation 2.3). Thus, measurements are generally made on isolated frequencies such that high contrasts are achievable. To maintain a significant level of coherence when combining light from different beams, two strategies can be adopted. Depending on the system configuration, the beam combination can be done co-axially or multi-axially as depicted in Figure 2.5. While the first one superimposes the beams on a single pixel of the detector and modulates the delay between them (*temporal coherence*), the multi-axial combination scheme records the interferogram at one time but spreads in space (*spatial coherence*)

Co-axial beam combination

The co-axial combination is made in the pupil plane. The scheme consists of superimposing the beams on a 50/50 beam splitter before reaching a detector at both ends. The principle of this technique is illustrated in Figure 2.5a. The signals exiting the beam combiner are focused at the detector so that the fringes are encoded temporally and only intensities are recorded. It thus produces an Airy disk without spatial fringes. To temporally modulate the signals, an optical delay line is used to systematically modify the optical path between both arms. This optical delay of known amplitude can be introduced technically, for instance, by using piezo-electric mirrors. Nowadays this technique has largely been implemented in existing interferometers such

as CHARA/FLUOR [20], VLTI/PIONIER [21] and LBTI/NOMIC [22].

The co-axial combination has the advantage of efficiently using the detector pixel as all the light is focused on one single pixel that records time-intensity variations. The fact that both beams are being treated coplanarly allows the usage of spatial filtering techniques such as optical fibres to clean the beams. It provides an easy way of transporting the beam over large distances if required and makes high accuracy calibration possible. Nevertheless, the co-axial beam combination also has some limitations. Firstly, the information across individual apertures is erased and therefore can not be retrieved for analysis. Secondly, it is limited to a small field of view since a large deviation in the direction of propagation makes the collimation much more difficult. Usually, the maximum field angle corresponds to the diffraction limit of a single aperture. Finally, the beam splitters arrangements become more complex as the number of apertures grows.

Multi-axial beam combination

In a multiaxial beam combination, the different beams, coming from different directions, are brought together at a common focus in the image plane, producing the equivalent of Young's fringes. The fringe signal recorded is spread in the image plane over many pixels on the detector plane for one single time exposure. The spatial fringe coding is achieved by placing the exit pupils at certain distances to each other and then by the superimposition of the beams using, for instance, a lens that will introduce geometric path differences. For telescopes with more than two apertures, confusion between the fringes can be avoided by placing the corresponding exit pupils at varying distances relative to each other, as illustrated in Figure 2.5b. This results in different frequencies in the carrying waves, which allows the separation of the interferograms from the different baselines during data reduction. Multi-axial (Fizeau) combination is required for a wide field of view and is attractive when the telescope's aperture is comparable to the baseline length. This method is currently used on VLTI/MATISSE [23] as well as LBTI/LMIRCam [22].

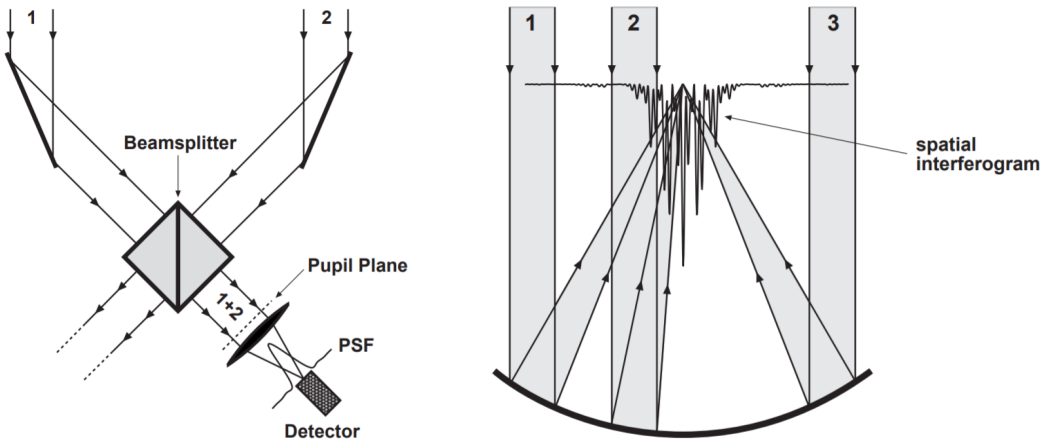

(a) Coaxial combination (b) Mulitaxial combination.

Figure 2.5: Different methods of beam combination in an interferogram [24].

2.2.2 Instrument response

The response of an interferometer is characterised by what is called its transmission map. Although this quantity is defined slightly differently according to considerations, the expression

used in this study is based on the geometrical configuration of Figure 2.6. In this figure, the two angular coordinates (θ, α) denote the planet's position in the sky plane and the line-of-sight is assumed perpendicular to the interferometer plane.

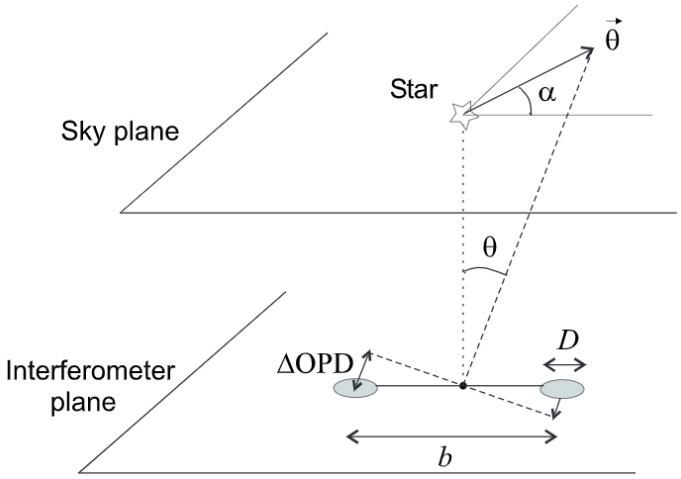

Figure 2.6: Geometrical configuration of the interferometer and of the stellar system [18].

Considering units apertures dimensions and equivalent light intensity distribution between both arms, the response of the interferometer writes as

$$R(\theta, \alpha) = 2\sin^2\left(\pi \frac{b\theta}{\lambda}\cos(\alpha)\right) \tag{2.5}$$

which can be approximated by

$$R(\theta, \alpha) \simeq 2\left(\pi \frac{b\theta}{\lambda}\cos(\alpha)\right)^2 \tag{2.6}$$

for $\theta << \lambda/b$ which means that the off-axis angle is small compared to the fringe spacing. Furthermore, Equation 2.6 implies that a perfect null response only occurs for $\theta = 0$. Since stars are not point-sources but have some angular extend, the light emanating from their corona is not perfectly cancelled by the interferometer. This undesired persistent emission is called "geometric stellar leakage" and is difficult to get rid of. It is related to the physical arrangement of the telescopes and to the angular size of the stellar photosphere.

Another metric useful to describe the performance of an interferometer, and closely related to the visibility function defined previously, is that of *geometric null depth* or *geometric nulling ratio*. This quantity expresses the ratio between the transmitted stellar flux and the initial stellar flux at the input of the beam combiner. Considering the observation of a star with angular radius θ_* at wavelength λ, the null depth can be expressed as follows

$$N = \frac{\pi^2}{4}\left(\frac{b\theta_*}{\lambda}\right)^2 = \frac{I_{min}}{I_{max}}, \tag{2.7}$$

where I_{min} and I_{max} are respectively the intensities recorded at the destructive and constructive outputs. The closer N is to 0, the higher the intensity of the null and the better the contrast. Generally, the difference in emitted intensity between a star and its revolving terrestrial planet is considered around $10^5 - 10^6$ in the thermal infrared. Thus, a nulling ratio $N = 10^{-5} - 10^{-6}$

is a minimum value for clear detection. Similarly, the rejection ratio ρ is defined as the inverse of N:

$$\rho = \frac{1}{N} = \frac{4}{\pi^2}\left(\frac{\lambda}{b\theta_*}\right)^2. \tag{2.8}$$

It depends on the wavelength to baseline ratio λ/b which sets the angular resolution of the interferometer, and the star angular radius θ_*. The rejection ratio decreases for longer baselines (or shorter wavelengths) as the star gets increasingly resolved.

2.2.3 Instrumental limitations

Additionally to geometrical constraints, there are also instrumental limitations mainly due to manufacturing imperfections or calibration and measurement imprecisions such as bad noise cancellation or inaccurate wavefront correction. The expression 2.8 is thus only valid for a perfect Bracewell interferometer, free of any error and aberration sources. However, in a more realistic case, the rejection rate is deteriorated by thermal turbulence and various instrumental effects causing inaccurate phase adjustment of the light beams, wavefront errors, intensity mismatches and error of polarisation. The works of *Lay,2004* [25] and *Ollivier,1999* [26] extensively discuss the contributions of both random noise and systematic errors on the null depth of an interferometer. The main errors they have identified are summarised hereafter.

Phase error

Phase error within each of the two beams implies that the wavefront is not flat before reaching the beam combiner. The effect is to shift the position of the fringes in the transmission map: the dark fringe is not centred any longer on the optical axis. Considering two incoming waves with the same intensity and with a relative phase difference $\pi + \delta\phi$, the nulling ratio becomes [27]:

$$N = \frac{I_{min}}{I_{max}} = \frac{2I_0 + 2I_0\cos(\pi + \delta\phi)}{4I_0} \simeq \frac{\delta\phi^2}{4}. \tag{2.9}$$

To maintain a null depth of 10^{-6} the maximum relative phase error admissible between both arms of the satellite is $\delta\phi = 2{\cdot}10^{-3}$ rad rms which corresponds to a $\lambda/1000$ wavefront quality. To decrease the measurement inaccuracies caused by such effects, one would need prior calibration of visibility loss by observing another star. Good adaptive optics, by means of deformable mirrors, for instance, as well as modal filtering thanks to optical fibres to clean the beams are both good solutions although the latter is made at the expense of flux.

Wavefront error

The corrugation of the wavefronts due to turbulence or imperfect optics produces a mismatch between the shapes of the two beams to be combined. Assuming the two wavefronts coming from two pupils are aberrated with a phase variance σ^2_ϕ, where $\phi(r)$ is the phase by which the wavefront is distorted at r (with "r" the radial distance from pupil centre), then the null depth becomes

$$N = \frac{1}{4}\left(\sigma^2_{\phi_1} + \sigma^2_{\phi_2}\right), \tag{2.10}$$

where the subscripts 1 and 2 relate to the pupil 1 and 2 of the interferometer. The distortion of the wavefront can be expressed as a linear combination of Zernike polynomials, where each of the different polynomials in the considered basis corresponds to a different category of aberrations

such as tip-tilt errors, asphericity and higher spatial frequency defects such as polishing errors. The tolerance on the wavefront quality for a null depth of 10^{-6} is

$$\text{WFE} = \frac{\lambda}{2\pi}\delta\phi = 0.955 \text{ nm rms} \tag{2.11}$$

where WFE is the standard deviation of the amplitude of the wavefront defect for an observation wavelength $\lambda = 3\mu$m. This constraint on the wavefront quality of $\lambda/3142$ is extremely demanding. Although mirrors can be polished to such a high level of accuracy, it is much more difficult to maintain wavefront errors in this field as these also depend on the differences in refractive index "n" of the media encountered during light propagation. However, with the help of modal filtering, this constraint on the quality of the wavefront can be relaxed. The process consists of injecting the beams into a single-mode waveguide (optical fibre, hollow waveguide, planar waveguide,...etc). As a matter of fact, in a perfect single-mode waveguide, there is only one possible spatial distribution of the propagating electric field: the guided mode. If two beams are injected into an optical fibre at the output, the two beams are strictly superimposed and the wavefronts are strictly identical. In fact, the only effect of these wavefront defects is to produce coupling differences between the two waves (i.e., differences in intensity between the electric fields coupled into the waveguide when the wavefronts are disturbed). The use of modal filtering gives a nulling ratio, according to *Mennesson et al. (2002a)* [28]

$$N = \frac{1}{16}\left(\sigma_{\phi_1}^2 + \sigma_{\phi_2}^2\right)^2 = \frac{\Delta\phi^4}{16} \tag{2.12}$$

where $\Delta\phi$ is the phase standard deviation which can reach a value $\Delta\phi = 6.3 \cdot 10^{-2}$ rad for a null depth of $N = 10^{-6}$ (and $\Delta\phi = 0.11$ rad for $N = 10^{-5}$). This gives a required wavefront quality of $\lambda/100$ which is less stringent than the previous value obtained.

Intensity mismatch

The unequal intensity in the two arms of the interferometer induces a non-null transmission on the optical axis. The additional amount of light in one of the beams will not interfere and thus contribute as a background emission. Letting I_0 being the intensity in the first arm and $I_0(1 + dI)$ the intensity in the second one, the expression of the nulling ratio is [27]

$$N = \frac{2I_0(1 + dI) - 2I_0 sqrt(1 + dI)}{4I_0} \simeq \frac{dI^2}{16}. \tag{2.13}$$

To avoid the reduction of fringe visibility by an amplitude difference between both arms, $N \leq 10^{-6}$ requires $dI \leq 0.4\%$, one can use knife edges to even out the propagated intensities.

Error of polarisation

There are various types of polarisation errors, but they can always be converted into phase or intensity errors. For instance, a differential phase shift between the two components s and p of light can be seen as a phase error between the two beams for each component separately, while differential rotation can be seen as an intensity error when projecting the rotated polarisation components onto the initial direction of the s and p vectors. In practice, *Serabyn (2000)* [29] has shown that polarisation errors lead to the following central transmission:

$$R_\lambda(0,0) = \frac{1}{4}\left(\Delta\phi_{s-p}^2(\lambda) + \alpha_{rot}^2(\lambda)\right) \tag{2.14}$$

Polarisation errors are strongly impacted by the optical configuration such that the beam transport and delay lines have to be designed to minimise differential polarisation effects.

2.3 Extinction and stellar leakage

The leakage of stellar photons depends on the extinction profile defined by the shape of the dark central fringe. The latter is fixed by the interferometric configuration (entrance pupil geometry, phase shift implemented). The final capability of the interferometer to mitigate the starlight is measured by the extinction rate which is the ratio between the residual energy after starlight cancellation and the total amount of energy collected by the telescopes,

$$\text{Ext} = \frac{E_{residual}}{E_{collected}}. \tag{2.15}$$

The extinction is maximised in the perfect case where the recombined wavefronts are identical in amplitude, phase, and polarisation.

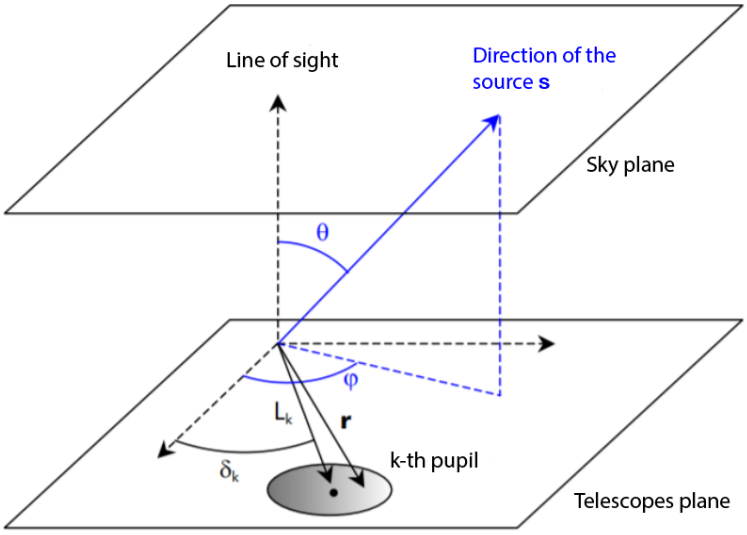

Figure 2.7: Representation of the coordinates of the k^{th} pupil in the telescopes plane and the angular coordinates of a source s [30].

Using the notations of Figure 2.7 and for a source whose direction in the sky-plane is given by $\vec{s}$, the phase of the field collected by the k$^{\text{th}}$ telescope, identified by the vector $\vec{L_k}$, is written

$$\Theta_k = \frac{2\pi}{\lambda}\vec{L_k} \cdot \vec{s} = \frac{2\pi}{\lambda}\left(L_k \cos\delta_k \sin\theta \cos\varphi + L_k \sin\delta_k \sin\theta \sin\varphi\right). \tag{2.16}$$

The angular distance θ from the source to the star being small, $\sin\theta \simeq \theta$ which gives

$$\Theta_k = \frac{2\pi}{\lambda} L_k \theta \cos\left(\delta_k - \varphi\right). \tag{2.17}$$

The complex amplitude, resulting from the superposition of the wavefronts from each telescope, is expressed as a sum

$$\Psi(\theta,\delta) \propto \sum_k D_k . e^{i(\Theta_k + \phi_k)} = \sum_k D_k . e^{\left(\frac{2\pi}{\lambda} L_k \theta \cos(\delta_k - \varphi)\right)} e^{i\phi_k} \tag{2.18}$$

where ϕ_k is the phase arbitrarily introduced in the kth arm to achieve extinction on the axis of the instrument. Again, the angular distance θ being very small, Equation 2.18 can be developed in the vicinity of 0 such that

$$\Psi(\theta,\delta) \propto \sum_k D_k.e^{i\phi_k}\left[1 + i\frac{2\pi}{\lambda}L_k\theta\cos\left(\delta_k-\varphi\right) - \frac{4\pi^2}{\lambda^2}L_k^2.\theta^2\cos^2\left(\delta_k-\varphi\right) + O(\theta^3)\right]. \quad (2.19)$$

This equation is parameterised by the interferometer characteristics (introduced phase shifts, diameters and position of collecting pupils). Thus, the extinction directly depends on the ability of an interferometric configuration to cancel out successive terms of Equation 2.19. For a Bracewell-type interferometer, only the first-order term is cancelled, which indicates that the interferometric configuration extinguishes any light source in the centre of the field (as stated in Section 2.2.2).

Mathematically, for $(\theta = 0, \varphi = 0)$ and considering unit apertures dimensions, the condition is

$$\sum_k^2 D_k.e^{i\phi_k} = e^{i\phi_1} + e^{i\phi_2} = 0 \quad (2.20)$$

which is verified for $\phi_1 = 0$ and $\phi_2 = \pi$. Furthermore, the condition for second term cancellation is

$$\sum_k^2 D_k.e^{i\phi_k}L_k\theta\cos\left(\delta_k-\varphi\right) = 0 \quad (2.21)$$

Considering again a two telescope interferometer with previously defined phase shifts, arms of equal length $b/2$ and unit apertures dimensions, the left-hand side of the equation can be developed

$$\begin{aligned}\sum_k^2 D_k.e^{i\phi_k}i\frac{2\pi}{\lambda}L_k\theta\cos\left(\delta_k-\varphi\right) &= i\frac{2\pi}{\lambda}\left(\frac{b}{2}e^{i.0}\theta\cos(0-\varphi) + \frac{b}{2}e^{i.\pi}\theta\cos(\pi-\varphi)\right)\\ &= i\frac{2\pi}{\lambda}\left(\frac{b}{2}\theta\cos\varphi + \frac{b}{2}\theta\cos\varphi\right)\\ &= i\frac{2\pi}{\lambda}b\theta\cos\varphi\end{aligned} \quad (2.22)$$

where $(\delta_1, \delta_2) = (0, \pi)$. Therefore, the amplitude is varying according to a θ^2 function, while the extinction rate which is proportional to the square of the amplitude, depends on θ^4 such that

$$\text{Ext} \propto 4\left(\frac{b\pi\theta}{\lambda}\right)^2\cos^2(\varphi) \quad (2.23)$$

which is a similar result to the one obtained in Equation 2.6 for the interferometer response. Thus, the extinction is varying according to a quadratic function (θ^2) for a Bracewell like interferometer. To reach a higher order of variation (θ^4), at least 3 apertures are needed. Such a higher order profile induces better extinction of the starlight than a θ^2 profile, as its shape is more curved (see Figure 2.8). The dark fringe therefore better "covers" the surface of the star as it is closer to the ideal gate function. In other words, the transition between bright and dark regions is steeper.

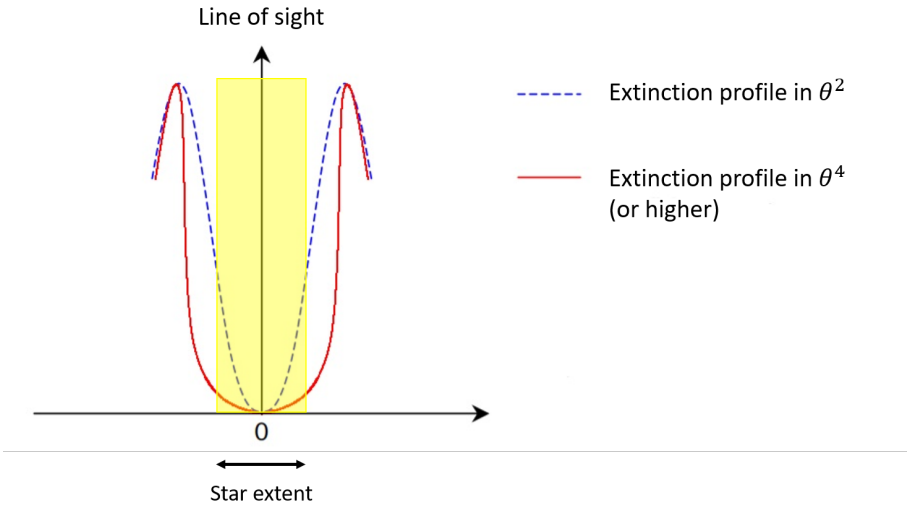

Figure 2.8: Schematic illustration of the θ^2 and θ^4 (or higher order) extinction profiles of the destructive central fringe [30].

2.4 Nulling systems

A dual-arm nulling interferometer requires the π phase shift between the two beams to be as exact as possible. This is easily done for monochromatic light by adjusting the optical path difference between each telescope. However, when moving to poly-chromatic light, the situation becomes more complex. In order to achieve an achromatic phase shift over the entire spectral band considered, more sophisticated recombination systems are required. An example of those is the Achromatic Interferential Coronograph (AIC) designed for the Darwin mission and the Mach-Zender beam combiner used for instance in the FKSI satellite.

2.4.1 Achromatic Interferential Coronograph (AIC)

To work with a telescope, the AIC splits the collected wave into two waves and phase shifts them by π. This phase shift is achromatic, as it is based on a property of light involving that the passage of a wave through a focus causes a phase shift of π at any wavelength.

The AIC is a Michelson Fourier interferometer modified by the insertion of a focus on one of the arms, which induces a 180° rotation of the pupil and introduces a π achromatic phase shift. The passage through the focus is provided by a cat's eye system on one of the arms, while a train of three flat mirrors on the other arm balances the optical paths as represented in Figure 2.9.

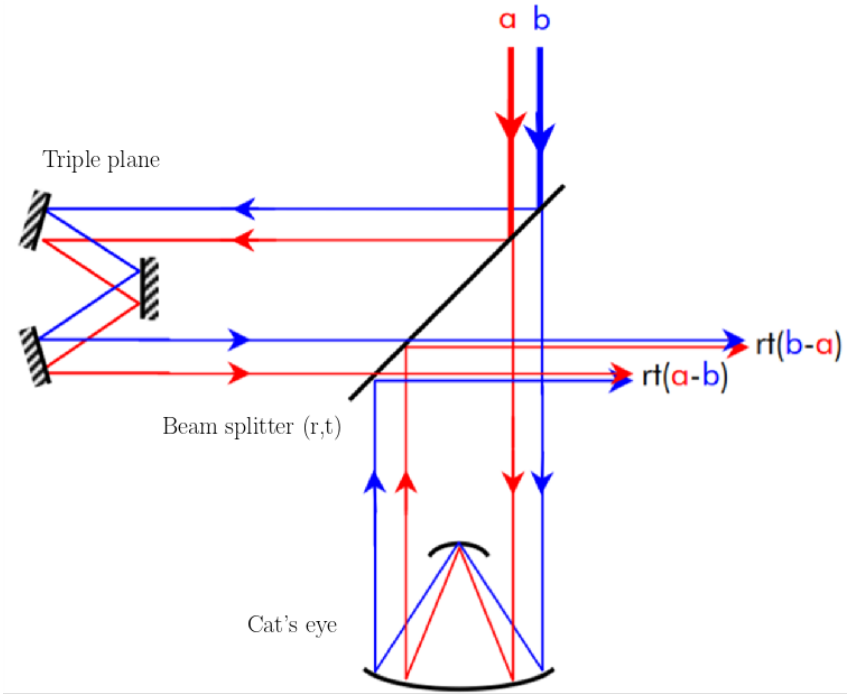

(a) Starlight nulling system

(b) Co-axial beam recombination.

Figure 2.9: Schematic representation of the IAC structure [30].

The two incoming beams a and b are divided equally into two sub-beams. In the cat's eye path, the wave is phase-shifted by π. In the triple-plane path, the wave does not undergo any transformation. This structure generates two beams $s_1 = rt(b-a)$ and $s_2 = rt(a-b)$ with opposite intensities and for which the starlight at the centre of the pupil has been suppressed. This suppression is more clearly illustrated in Figure 2.10, where it can be seen that the cat's eye path imposes a phase shift of π as well as a rotation of the pupil by 180° (central symmetry). The triple plane on the other hand has axial symmetry. After combination, the pupil central illumination is cancelled while the off-axis emission from the planet is still recorded with two twin images with opposite intensities.

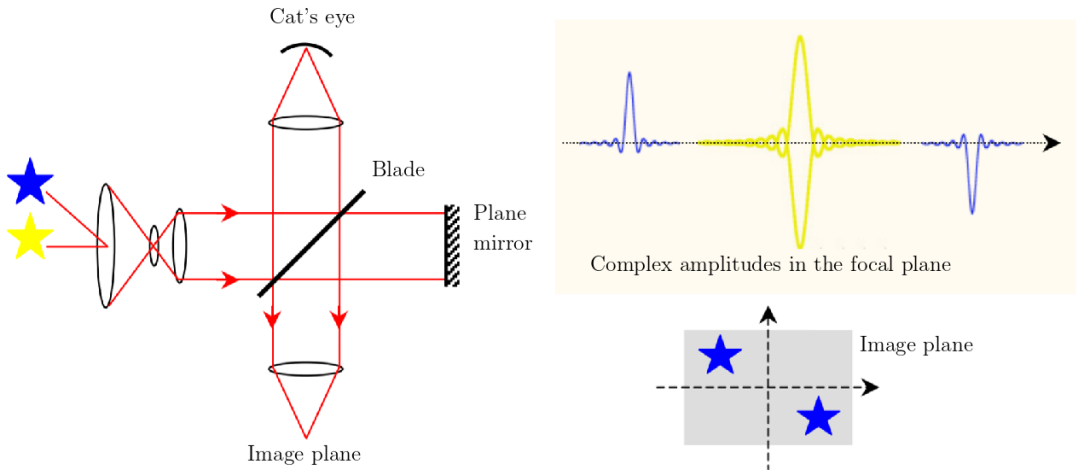

Figure 2.10: Schematic illustration of the AIC impact on image formation [30].

If we assume that the separating blade on Figure 2.9b has a coefficient of reflection and transmission r' and t', and that the energy, of the two complex amplitudes s_1 and s_2 at the input, is redistributed into two channels s'_1 and s'_2, the output complex amplitudes are

$$s'_1 = r's_1 + it's_2, \tag{2.24}$$
$$s'_2 = r's_2 + it's_1. \tag{2.25}$$

Since the blade induces a $\pi/2$ phase shift between the transmitted and reflected wave, a $\pi/2$ phase shift must be introduced in one of the arms to obtain a destructive interference in one of the two exiting beams. The complex amplitudes s'_1 and s'_2 can thus be rewritten

$$s'_1 = r's_1 + it'(s_2 + e^{i\pi/2}) = rt(b-a)(r'+t'), \tag{2.26}$$
$$s'_2 = r'(s_2 + e^{i\pi/2}) + it's_1 = irt(a-b)(r'-t'), \tag{2.27}$$

according to the definition of s_1 and s_2 and considering that $e^{i\pi/2} = i$. We can express the intensity at both exits

$$I_1 = |s'_1|^2 = r^2t^2|b-a|^2(r'+t')^2, \tag{2.28}$$
$$I_2 = |s'_2|^2 = -r^2t^2|a-b|^2(r'-t')^2. \tag{2.29}$$

Assuming the blades are perfect and considering the beams' amplitudes such that

$$\begin{aligned} &A = |a|^2; \qquad B = |b|^2; \\ &R = |r|^2; \qquad R' = |r'|^2; \\ &T = |t|^2; \qquad T' = |t'|^2 \\ &\text{with} \quad R = R' = T = T' = \frac{1}{2} \text{ and } A = B, \end{aligned} \tag{2.30}$$

the intensities become

$$I_1 = \frac{1}{2}\left(A + B - 2\sqrt{AB}\cos(\phi_{ab})\right) = A\left(1 - \cos(\phi_{ab})\right) \tag{2.31}$$
$$I_2 = \frac{-1}{4}\left(A + B - 2\sqrt{AB}\cos(\phi_{ab})\right) \cdot (1-1) = 0. \tag{2.32}$$

The intensity I_2 of the s'_2 path is zero whatever the situation. However, the intensity I_1 (path s'_1) depends on ϕ_{ab} which represents the relative phase shift between the two beams. If we consider the telescope to be perfectly pointed to the star such that it is centred on the aperture, then no optical path difference is present between both arms ($\phi_{ab} = 0$) and therefore no photons are recorded at the exit s'_1 neither. However, the planet is not perfectly aligned with the satellite line of sight, which means its signal will follow a different path in the two beams of the telescope, resulting in a non-null phase shift ϕ_{ab}. By rotating the interferometer or by adjusting the transmission map of the satellite, the signal of the planet can be placed on a bright fringe such that $\phi_{ab} = \pi$. The intensity I_1 is, therefore, no more zero and becomes $I_1 = 2A$ which corresponds to the total collected energy of the planet. The channel s'_1 contains therefore the entire energy of s_1 and s_2.

2.4.2 Mach-Zehnder interferometer

The Mach-Zehnder interferometer is an optical interferometer created in 1891 and 1892 by Ludwig Mach whose principle is very close to that of the Michelson interferometer. It consists of two plane mirrors and two semi-reflecting mirrors used to make a single beam interfere with itself constructively or destructively depending on the output. For the case of two inputs, the design has to be slightly adapted and is presented in Figure 2.11.

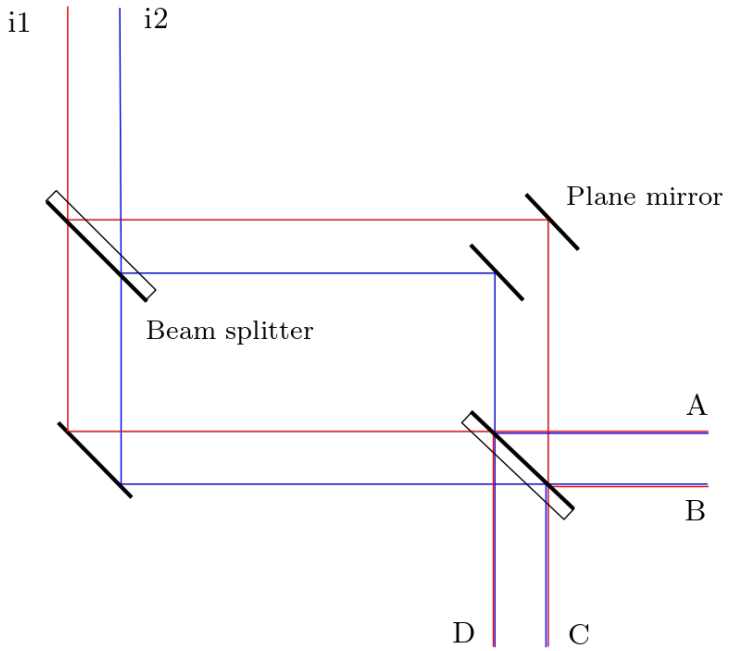

Figure 2.11: Schematic illustration of a dual input beams Mach-Zehnder interferometer.

This design, studied in [29], has the advantage to be fully symmetric as well as very simple (requires only flat optics). This greatly eases several design constraints. To reach a stable and deep null of the central starlight, one of the beam has to be subjected to a field reversal, which is a relative rotation by 180° with respect to the other one. This can be done by the use of a cat's eye system such as for the achromatic interferential coronograph of the Darwin mission. However, another concept based on the use of right angle periscopes for both beams can be used. It is conceived such that each beam experiences a rotation by 90° making thus a relative rotation of 180° between the beams because of the oppositely directed middle beam segments illustrated in Figure 2.12.

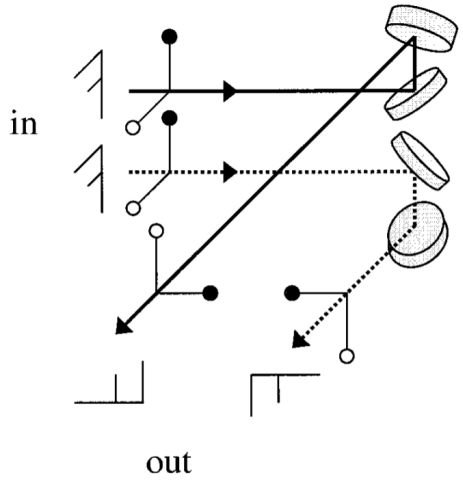

Figure 2.12: Illustration of a mirror-reflected pair of right-angle periscopes where each polarisation component undergoes one s- and one p-plane reflection [29].

With such field reversal the Mach-Zehnder interferometer, presented in Figure 2.11, can be used for starlight nulling. The images within the two beams at the system's entry have been rotated by 180° with respect to the line of sight. Thus, one only needs now to combine both beams and to introduce a relative π phase shift between the two to guarantee the cancellation of the centrosymmetric data corresponding to the star's emission. The distribution of intensity is therefore similar to the one illustrated in Figure 2.10 for the AIC. But, the correct cancellation of the star's emission requires equal amplitudes at the combiner input and identical reflection and transmission coefficients at the beam splitters. Otherwise, there will be an energy difference between the two arms at the recombination stage. This would lead to incomplete suppression of the axial signal and therefore the measurement of a photon flux coming directly from the star generating important noise. Furthermore, in order to ensure coherent interference of the beams, the path i_1, from Figure 2.11, must be extended by a distance equivalent to the path difference with respect to beam i_2. This is a consequence of the Mach-Zehnder interferometer geometry. Once the OPD is corrected, the outputs A and B are constructive while outputs C and D are destructive because of the π phase shift generated by the uneven number of metallic reflections (from the surface of a medium with a higher refractive index than that of the medium in which they are travelling). These output beams can now be focused on a detector to measure the temporal variation of the signal. Mathematically, we can define the amplitudes of the beams i_1 and i_2 by "a" and "b". Considering that the pupil rotation can be seen, from the intensity point of view, as a phase shift of π, the amplitudes of the four outputs A, B, C, and D are written

$$\begin{aligned} o_A &= a\ rt' + b\ e^{i\pi} tr \\ o_B &= a\ tr + b\ e^{i\pi} rt' \\ o_C &= a\ e^{i\pi} tt + b\ e^{i\pi} rr' \\ o_D &= a\ rr' + b\ e^{2i\pi} tt \end{aligned} \tag{2.33}$$

where r, t and r', t' are respectively the coefficient of reflection and transmission of the first and second beam splitter. Taking the same assumptions as for the AIC (Equation 2.30), the intensities at the four exits are

$$\begin{aligned} I_A &= RT\left(A + B - 2\sqrt{AB}\cos\left(\phi_{ab}\right)\right) = \frac{A}{2}\left(1 - \cos\left(\phi_{ab}\right)\right) \\ I_B &= I_A \\ I_C &= AR^2 + BT^2 + 2RT\sqrt{AB}\cos\left(\phi_{ab}\right) = \frac{A}{2}\left(1 + \cos\left(\phi_{ab}\right)\right) \\ I_D &= I_C \end{aligned} \tag{2.34}$$

For an on-axis source, the relative phase shift between the two beams i_1 and i_2 of the interferometer is zero, which gives intensities $I_A = I_B = 0$ corresponding to the destructive outputs, and intensities $I_C = I_D = A$ representing the bright outputs (where the starlight has not been cancelled). However, for an off-axis source, the relative phase difference between the two interferometers arms is no longer zero and will vary according to the satellite's baseline orientation with respect to the star-planet alignment. Therefore, the rotation of the interferometer will produce a time modulation of the signal such that the intensities recorded at each exit will vary according to the planet's signal passing from dark to bright fringes periodically. This intensity time variation is what is recorded by the detector and allows the detection of an eventual planet.

2.5 Fringe tracker

In an interferometer, a fringe tracker is an essential device to allow the observation of faint sources. As a matter of fact, the throughput of an interferometer is often low ($\sim 1\%$ to $\sim 10\%$), due to a large number of optical elements (telescope, beam transport, tip-tilt corrector, wavefront corrector, delay lines, beam combiner) and degradation of coating with time [31]. For on-ground interferometer, atmospheric turbulence and vibrations move fringes very rapidly. Generally, the coherence time is used to express the time extent over which the optical path variation generates rms phase aberrations smaller than 1 radian. In the visible range, this period is only a few milliseconds [32]. Measurement is therefore only possible if the individual exposure time is much smaller than the time it takes for the fringes to move by a wavelength. Without a phase tracking system, observation of faint targets is thus very difficult. Typical limiting stellar magnitudes for interferometers are in the range of 5 to 10 for the visible to near-infrared domain [33]. To extend this limit, one needs to track and lock the fringes to enable long exposures. A fringe tracker rapidly measures the fringe position and actively controls optical path length correctors (fast delay lines) at the input of the beam combiner.

Chapter 3

Previous Missions

Investigating previously developed missions can be very helpful to gain insight into the driving requirements inherent to such type of system. It helps to highlight the different design possibilities and associated performance. The most sensitive design parameters can be identified which helps to define what is limiting the performance of the system and what could improve it. For this purpose, the important characteristics of several missions in the field of exoplanet research are summarised hereafter.

3.1 Large Interferometer For Exoplanets (LIFE)

The LIFE project was initiated in 2017 and officially kicked off in 2018. It consists of the development of a space-based MIR nulling interferometer capable of detecting and characterizing the thermal emission of (temperate) rocky exoplanets. LIFE is stacking on the heritage of ESA's Darwin and NASA's TPF-I concepts. These projects were not implemented because of technical issues, but also because our understanding of the exoplanet population was significantly more restricted at the time. Nowadays, most technologies required to fly a space-based nulling interferometer have now reached a Technology Readiness Level (TRL) of 5 [34], meaning that the components have been tested and validated in their appropriate environment. Therefore LIFE aims at reassessing such a mission concept and quantifying its potential scientific return using the current technology. The present project baseline envisages a nulling interferometer concept consisting of several collecting telescopes flying in formation with a beam-combining spacecraft at their centre as illustrated in Figure 3.1. The high spatial resolution required to separate the exoplanet signal from that of the host star will be achieved by the separation between the telescopes, which, in principle, can be adapted depending on the scientific specifications.

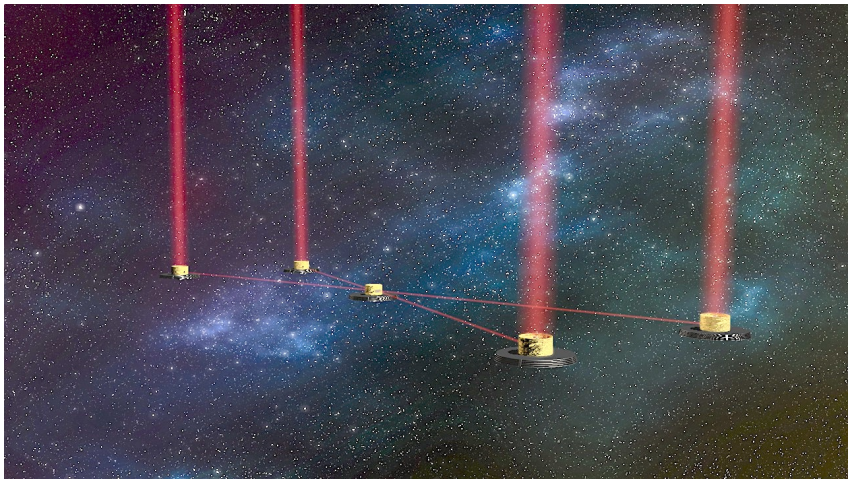

Figure 3.1: Artist impression of the LIFE mission concept. [34]

LIFE is currently in a first study phase and the main activities being currently executed are summarised on the project web-page[1]. The mission is planned to be divided into two distinct phases. The first one consists of a search phase to directly detect a large sample of exoplanets orbiting nearby stars. The second phase is a characterisation phase aiming to re-observe a sub-sample of these exoplanets and study their properties and atmospheres in more detail. The mission is estimated to last about 5 to 6 years with 2 years dedicated to the initial search phase.

The number of detected planets depends on the threshold one puts on the SNR of the planets, which in turn depends on the assumed aperture size of the collector spacecraft and the assumed number of planets detected per time interval δt. Considering a SNR of 7 and an aperture diameter D = 2 m, the satellite should be able to detect more than 200 hot rocky and Super-Earths planets and more than 150 hot Sub-Neptunes in the range of wavelengths from 4 to 18.5 μm [35].

3.2 The Fourier Kelvin Stellar Interferometer (FSKI)

The Fourier-Kelvin Stellar Interferometer (FKSI) is a mission concept, proposed in 2003, developed under NASA supervision for an imaging and nulling interferometer for the near-infrared to the mid-infrared spectral region (3-8 microns). The satellite was planned to be launched at the Lagrange L2 point to begin its observations. Such a site was chosen in order to reach a passive cooling of the spacecraft to 65 K. Its scientific objectives were to directly detect extrasolar giant planets (EGP), study debris disks and the evolution of protostellar and evolved stellar systems, and to facilitate the study of extra-galactic star formation regions and the extended neighbourhoods of active galactic nuclei [36].

[1] https://www.life-space-mission.com

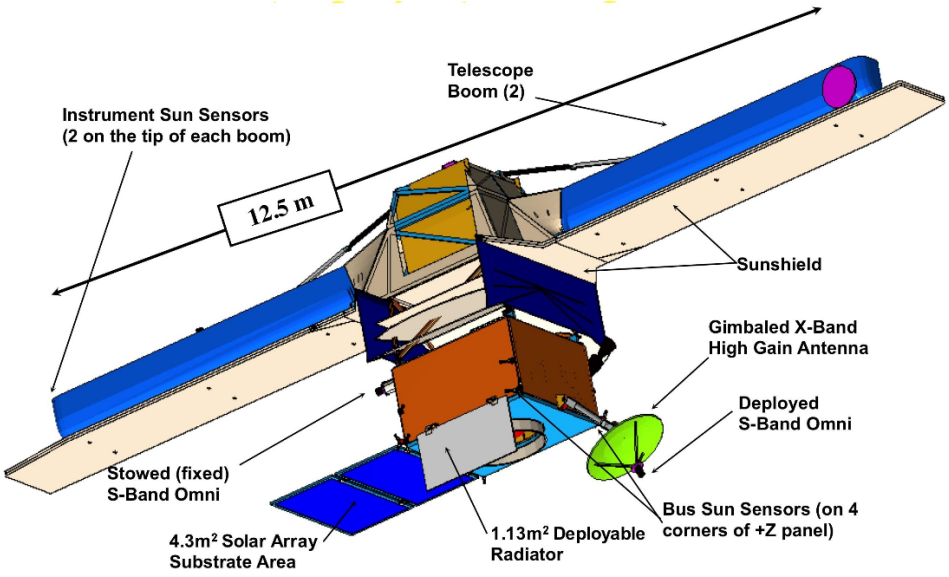

Figure 1. Mechanical design of current version of FKSI.

Figure 3.2: FKSI design overview [36].

3.2.1 Technical specifications

The final design was a nulling interferometer configuration with two 0.5 meter telescopes spaced by a distance of 12.5 meters thanks to a boom forming the basis of the interferometer. This allows a resolution of 25 to 66 mas across depending on the wavelength (from 3 to 8 μm with higher wavelengths corresponding to a lower resolution). Both telescopes are siderostats plane mirrors inclined by 45° in order to bring the light toward the centre of the satellite. There, the light is collimated by an off-axis parabola on a symmetric Mach-Zehnder beam combiner followed by a null tracker and a hollow-core fibre allows creating the required null depth of 10^4 for such type of mission. The light from the bright output of the Mach-Zehnder beam combiner is finally focused on a 35 K detector array as illustrated in Figure 3.3 which permits later scientific analysis.

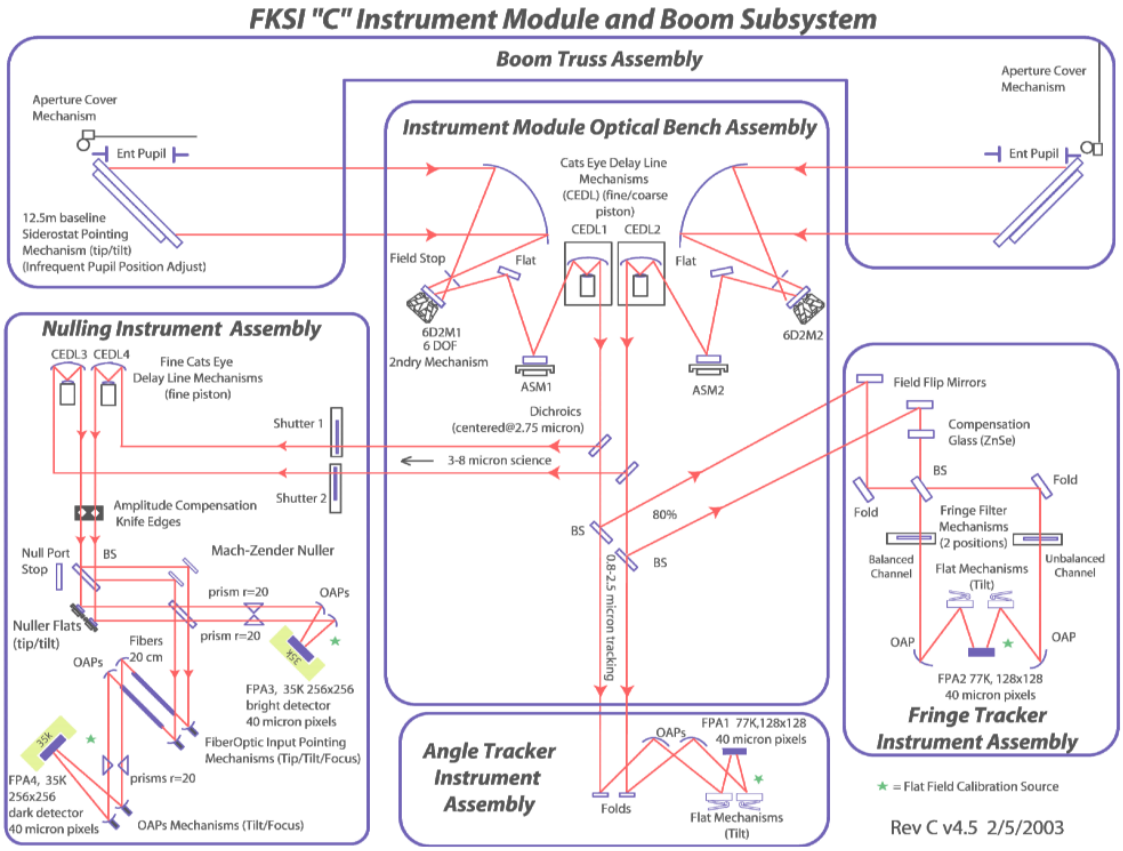

Figure 3.3: Layout of the FKSI optical system [36].

3.3 Darwin/TPF-I

The Terrestrial Path Finder Interferometer (TPF-I) from NASA and the Darwin interferometer from ESA were similar missions aiming at detecting and characterizing exoplanets at mid-infrared wavelengths through the use of nulling interferometry and formation-flying telescopes. Although some aspects of the missions differed, they had almost identical science and technology requirements as well as very similar target lists. Both missions remained at the development stage and have never been launched due to financial issues.

3.3.1 Darwin

ESA received Darwin proposal in 1993 and the mission concept was selected for a further industrial study in 1997. The mission was specifically designed for the detection of terrestrial exoplanets around nearby stars (1000 of them) with a first objective to search for CO_2 at 15 μm [37]. Darwin proposed to conduct observations in the mid-infrared because at these wavelengths the star-planet contrast drops to a million to one instead of thousands of millions to one in the visible. It was originally using 6 telescopes, placed on individual free-flying satellites, with 1.5 meters mirrors on 5 of them, as illustrated in Figure 3.4. The last one (at the centre) was equipped with a beam combination system (a free-flying optical bench) and a communication system.

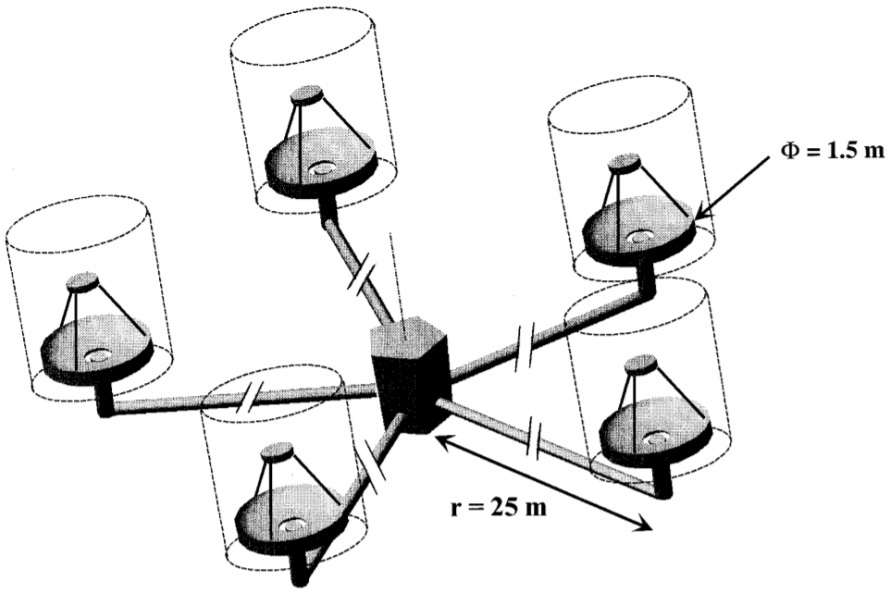

Figure 3.4: View of initial Darwin configuration [37].

The design has then been significantly simplified later on to a configuration consisting of 3 telescopes of more than 3 meters (up to 4 meters) in diameter spaced by a hundred meters. But the constellation would have stayed in formation with millimetre precision which was not enough for Darwin to work as a deviation larger than 0.1 mm could importantly degrade the detection [38].

3.3.2 TPF-I

TPF-I mission study started in 2000. It aimed principally at characterising terrestrial planets environments with mid-infrared spectroscopy, determining which planets have conditions suitable for life and searching for signs of life. The constellation was based on a long-baseline interferometer operating in the mid-infrared (6–20 μm) with 3 to 4-meter telescopes configured as an array operating on separate spacecraft over distances of a hundred meters. The resolution was defined to be 20 mas at 10 μm and the field of view was 1 arc-second at 12 μm. The telescopes operating temperature were set to 40 K [39][40].

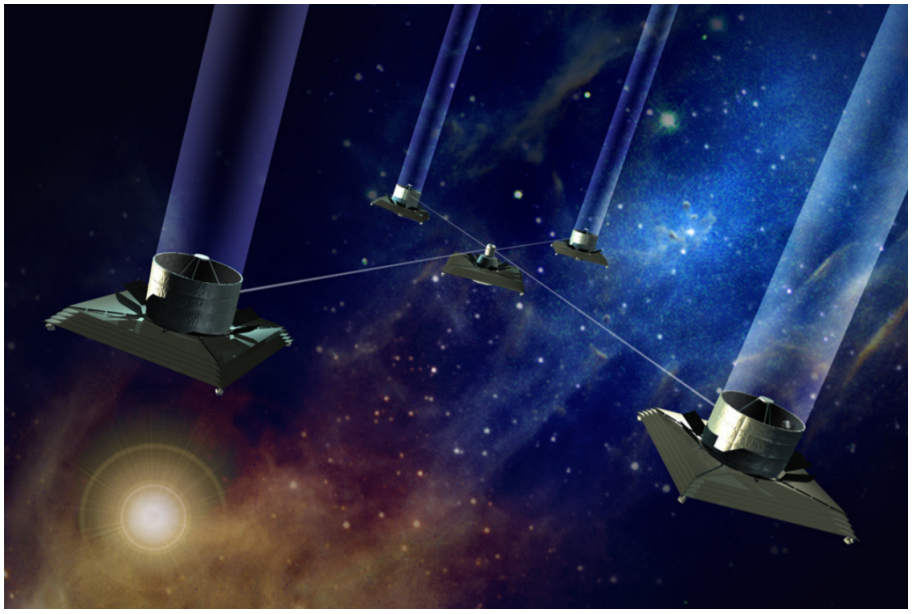

Figure 3.5: NASA TPF-I satellite representation [39].

The main characteristics of the mission are summarised in Table 3.1 from [40].

Parameter	**Value**
Telescopes	4 with 2m diameter, diffraction limited at 2 μm
Optics temperature	40 K
Baseline length	40 - 100 m
Wavelength range	6.5 - 15 μm (goal of 6.5 - 18)
Angular resolution	50- 75 mas
Field of view	1 arcsec at 12 μm
Spectral resolution	25 (goal of 50) $\Delta\lambda/\lambda$
Sensitivity	0.35 μJ at 12 μm
Orbit	L2 Halo orbit
Mission duration	5 years (goal of 10)

Table 3.1: TPF-I 4-Telescope Dual Chopped Bracewell Design important parameters.

3.3.3 The Emma-X-array configuration

The Emma-X-array architecture is the final result of the collaboration between NASA and ESA. It features four 2 meters diameter mirrors arranged in a square formation [41]. In this design, the combiner is moved out towards the star by about 1 km, and the collectors are reduced to simple spherical mirrors as illustrated in Figure 3.6.

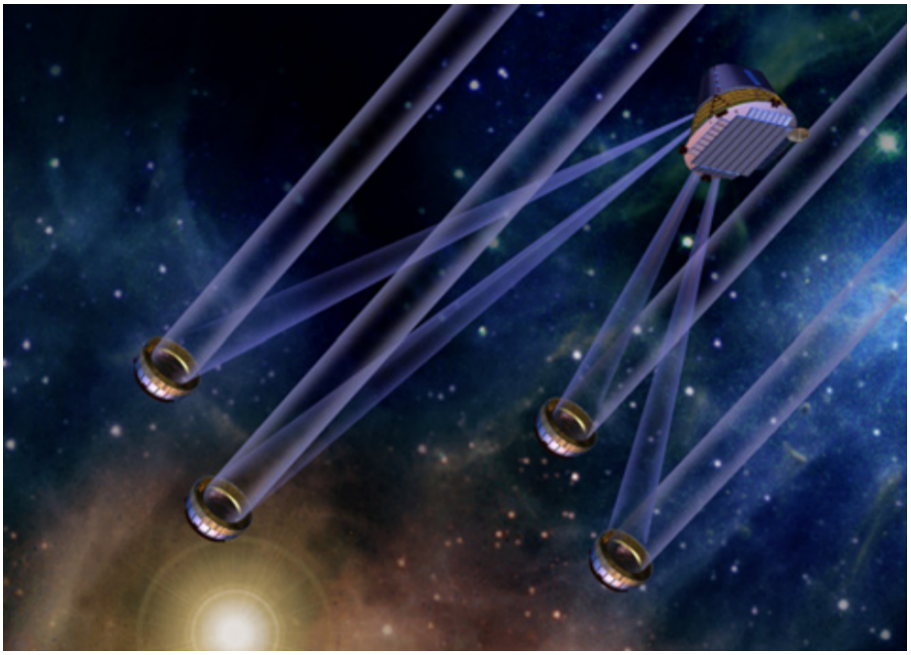

Figure 3.6: NASA TPF-I satellite representation. (Spacecraft image courtesy of T. Herbst, MPIA)

Telescopes work by pairs acting as separate nulling interferometers. The distance between telescopes in each pair therefore can be tuned to best suppress background stellar leakage around the null. Then the distance between one pair and the other can be adjusted to provide the angular resolution necessary to unambiguously isolate the light from a planet. The collector diameter can be scaled up or down to fit the mission performance requirements, with minimal impact on the combiner design. Compared to previous designs this architecture significantly reduces the complexity of the collector spacecraft and offers almost full sky coverage over a year of observation [41]. The important characteristics of the Emma-X-array design are retrieved on Table 3.2 from [42].

Parameter	**Value**
Telescopes	4 with 2m diameter spherical mirrors, diffraction limited at 2 μm
Optics temperature	50 K
Array size	400 x 67 m to 120 x 20 m
Wavelength range	6 - 20 μm
Angular resolution	2.4 mas to 8.2 mas (at 10 μm, scaling with array size)
Field of view	1 arcsec at 10 μm
Null depth	10^{-5} at 10 μm (without stellar size leakage)
Spectral resolution	25 $\Delta\lambda/\lambda$ (for planets)
Sensitivity	0.3 μJ at 12 μm
Orbit	L2 Halo orbit
Mission duration	5 years (goal of 10)

Table 3.2: 4-Telescope Chopped X-Array Emma Design parameters

3.4 PEGASE

The PEGASE mission was proposed in 2004 by a consortium of scientific laboratories in response to a call from the CNES for spaceborne formation flying missions [43]. It is the precursor of Darwin/TPF and served mainly as a technology demonstrator. It consists of a nulling interferometer with two apertures similarly to the Bracewell interferometer. It is composed of three free-flying satellites (2 siderostats and 1 beam combiner) with a baseline varying from 50 to 500 m. The goals of PEGASE were the spectroscopy of hot Jupiter (Pegasides) and brown dwarves, the exploration of the inner part of protoplanetary disks, and the validation in real space conditions of nulling and visibility interferometry with formation flying. To reach this purpose, it was designed to be launched at the Lagrange L2 point where it would have been passively cooled to 90 K (55 K for the optics). Although the mission was selected to proceed through a phase 0 process and estimated to become viable after a further 8-9 years of development, it has not been selected by ESA for its Cosmis Vision Program [44].

3.4.1 Technical specifications

PEGASE aimed at observing compact sources which emission peaks between 1.5 and 6 μm corresponding to a temperature range from 500 to 3 000 K. In such spectral range, the angular resolution was presumed to be about 0.5 to 30 mas depending on the satellites' separation. The two apertures were limited to a diameter of 0.4 meters due to accommodation constraints under a Soyuz fairing [45]. The general structure can be seen in Figure 3.3 where the primary mirrors (M1) are flat siderostat with a 45° angle. M2 and M3 form a simple afocal with a magnification of 20.

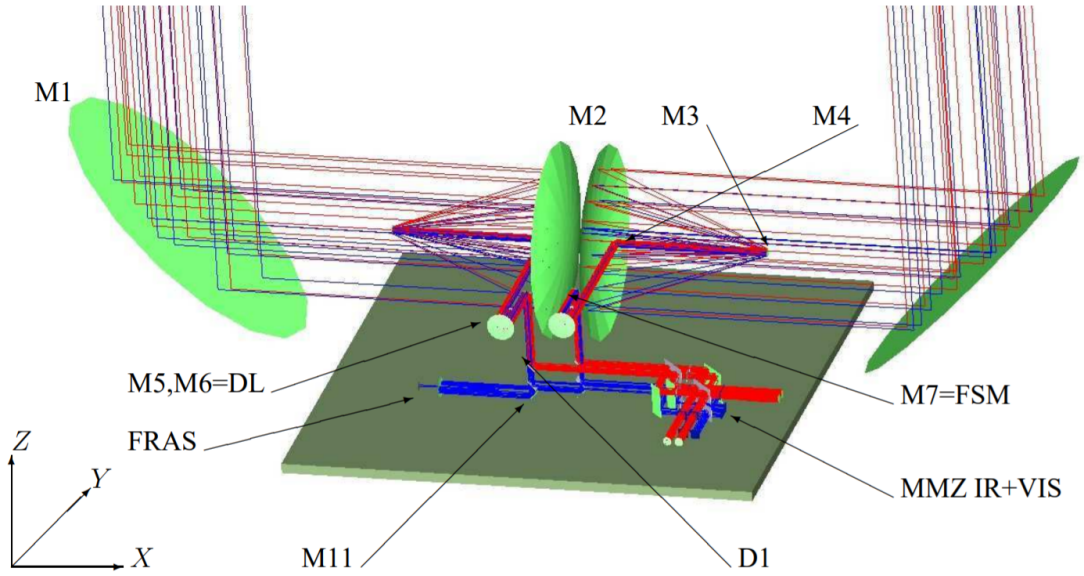

Figure 3.7: Representation of the optical system made by the three PEGASE satellites [45].

The fourth mirror (M4) consists of a small flat mirror, which directs the rays towards the active stage and, in combination with M1, creates an achromatic π phase shifter using field reversal by reflection. Subsequently, an optical delay line with cat's eye reflectors is used to correct the optical path length. It is followed by a modified Mach-Zehnder beam combiner whose four outputs are focused into single-mode fibres with a different composition according to the spectral range to be observed. A fluoride glass fibre can cover the spectral range from 1.5 to

3 μm whereas a chalcogenide fibre is required for the spectral range between 3 and 6 μm. The light is finally focused on a detector array with a goal to reach a signal to noise ratio (SNR) of 10.

3.5 Cold Interferometric Nulling Demonstration in Space (CINDIS)

CINDIS is a modest cost technology demonstration mission, proposed in 2003 in response to NASA Extra-Solar Planets Advanced Concepts, aiming at validating the key technologies needed to build, test, and fly mid-infrared interferometer architectures for Terrestrial Planet Finder (TPF) rather than improving science capability [46]. Thus, it renounces scientific objectives from the beginning and focuses on a low-risk implementation of the mission as well as a cost below 300 millions dollars. Such significant cost saving enables the demonstration of important features of an interferometer for terrestrial planets detection such as high-contrast nulling interferometry at a wavelength of 10 μm, vibration control techniques, instrument pointing and path control, stray light management and eventually four apertures combined nulling process. The primary objective was to demonstrate a stable null on several stars in the specified passband. CINDIS was predicted to be launched in June 2007 on a Delta launcher and intended to perform the first nulling interferometry in space, using small apertures ($\sim$40 cm diameter) and a short structurally fixed baseline ($\sim$2 m). This forms a simple Bracewell nulling interferometer with a null depth around 10^{-5} which is a typical allocation for TPF. A heliocentric drift-away orbit[1]was chosen due to its good thermal stability and easy passive cooling achievable. A Sun-synchronous orbit was also an envisaged alternative but the estimated cost savings were small compared to the increase in mission risk.

3.5.1 Technical specifications

The observing waveband of CINDIS is 6-12 μm with the use of cryogenic optics to maintain a low instrumental background. Stored cryogen is used since it is the cheapest and most reliable cooling system for a short (6-9 months) mission. Both apertures are 40 cm in diameter and create off-axis Cassegrain telescopes which direct the collected light onto a fast steering mirror (FSM). The primary and secondary of each telescope are confocal coaxial paraboloids and are used with off-axis pupils so that the 4 cm diameter output beams are unobstructed, as illustrated by Figure 3.8. The two subsequent FSMs control the tip-tilt to ensure the wavefronts are exactly parallel in the nulling beam combiner. An optical delay (piston) actuator with a total stroke of about 30 μm in one arm of the interferometer adjusts the optical path difference of the two beams to find the centre of the null. The whole satellite body is pointed to within $\pm$ 1.5 arcsec of the star direction[46].

[1]Heliocentric drift-away orbit: Earth-trailing (or leading) orbit rotating around the Sun with a period of 372,5 days. In this orbit the spacecraft slowly drifts away from the Earth and is at a distance of 0.5 Astronomical Unit (AU) (worst case) at the end of four years. **www.nasa.gov**

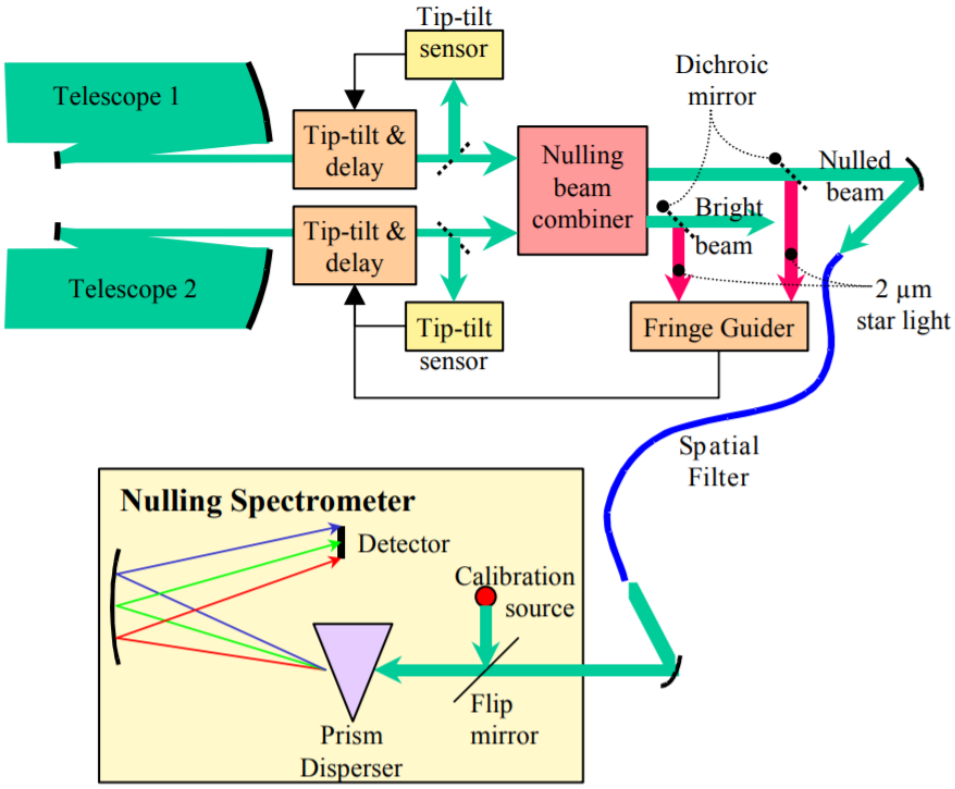

Figure 3.8: Optical layout of CINDIS spacecraft [46]

Chapter 4

System Conception

4.1 Project objectives

This work focuses on the theoretical conception of a spatial interferometer for exoplanet detection aimed to be accommodated on a PROBA-sized satellite. It is a satellite class designed around innovation at a reduced cost which belongs to the micro-satellite family according to ESA specifications which encompass satellites with masses smaller than 150 kg. More precisely it aims mainly at conceiving a simple and functional optical configuration for the interferometer arms and beam transport up to the detection. First of all, we need to define the wavelengths at which our system will perform its measurements. To do this, we must remember that the underlying objective, in addition to the detection of exoplanets, is to characterise the composition of their atmosphere. Analysing the planets atmosphere is indeed a necessary condition for understanding not only the planet itself, but also its formation, evolution, and potential habitability. Therefore, we are particularly interested in detecting chemical components that are abundant on Earth. The absorption spectrum of Earth atmosphere is illustrated in Figure 4.1, where we can see that it is almost transparent in the visible while it becomes nearly opaque in the UV ($< 300nm$) and the thermal infrared ($> 10\mu m$). In the near to mid-infrared, however, the absorption level greatly varies according to the gaseous components that are present. This is one of the reason space-based interferometers are chosen over ground-based ones. On the ground, the Earth's atmosphere will absorb a large part of the light spectrum in the UV and far-IR. For the wavelengths of interest (mid-IR) we are faced with absorption peaks linked to particular components. Thus, trying to observe the presence of water or carbon on an extra-solar planet from the ground is hardly feasible because the Earth's atmosphere will absorb most of the signal, so that it becomes almost impossible to distinguish the effect of the atmosphere of a potential exoplanet.

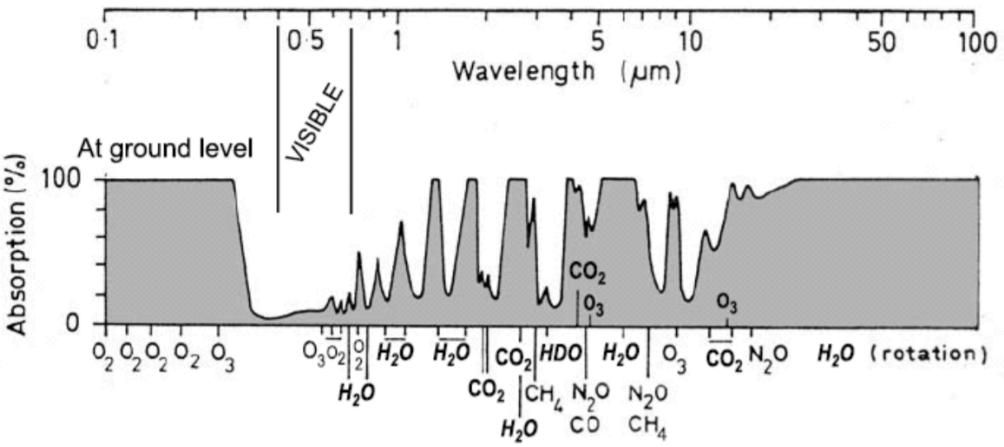

Figure 4.1: Absorption of spectra of atmospheric gases in the short-wave and long-wave range [47].

Each molecule has a particular absorption wavelength which corresponds to the absorption of energetic photons and the conversion of this energy into vibration mode of the molecule, or electronic processes, such as the release of one electron. The different Earth atmospheric constituents and their related absorption frequencies are listed in Table 4.1.

Constituent	Wavelengths of absorption (in the IR) [μm]
O_2	0.69 - 0.76 - 1.26
H_2O	1.1 - 1.4 - 1.9 - (2.6)
CH_4	0.6 - 1 - 1.7 - 2.4 - 7.6
CO_2	1.06 - 1.2 - 1.6
O_3	9.6
CO	5.8
CC	6.1
N_2O	1.55 - 4.4 to 5.4

Table 4.1: List of some Earth atmosphere constituents and their related wavelength of absorption.

Our atmosphere is mainly composed of water vapor (H_2O) at 80%, carbon dioxide (CO_2) around 19% and nitrogen (N) with less than 1%. The latter is present in our atmosphere in various forms, because of its catalytic cycle, such as N_2, NO, NO_2 and N_2O which is a greenhouse gas. Moreover, according to [48], diatomic oxygen is the most reliable bio-signature gas and observing its related spectrum of absorption is therefore of high priority. H_2O instead is not a bio-indicator. However, its presence in liquid form on a planet's surface is considered essential to life. Thus observing part of the water spectrum is also strongly desirable. The carbon-containing gases CO_2 and CH_4 can each provide useful information. In the mid-infrared range, CO_2 is the easiest of all species to observe. CO_2 is required for photosynthesis and other important metabolic pathways. Furthermore, it provides good evidence that a terrestrial planet is being observed. Methane can be a good indicator of the presence of ocean or volcanic activity.

In conclusion, the range of wavelength between 1 and 5 μm is a very interesting spectrum for astronomical observations since important gases helpful for planet characterisation and bio-signatures assessment absorb in that range. Nevertheless, although increasing the observation

wavelength would have given access to more data and different types of absorption, this increase is limited by the thermal emission of the instrument, which becomes dominant at longer wavelengths. To reach such higher values, the instrument has to be cooled down and more thermally stable. At a shorter wavelength, on the contrary, the planet photonic emission becomes too faint compared to the stellar flux, reducing the contrast. Furthermore, *Dandumont et al., 2020* [19] have investigated the possible exoplanet detection yield for different satellite configurations (CubeSat 6U, CubeSat 12U, PROBA-size and FKSI-concept summarised on Table 4.2) for different wavelengths as illustrated on Figure 4.2.

	CubeSat 6U	CubeSat 12U	PROBA-size	FKSI-concept
Size	$0.6 \times 0.1 \times 0.1$ m	$1.1 \times 0.1 \times 0.1$ m	1 m^3	
Baseline (m)	0.1	1	5	12.5
Pupil diameter (m)	0.08	0.08	0.25	0.5
Optical train temperature (K)	150	150	100	60

Table 4.2: Nano- to Medium-size inteferometer configurations studied [19].

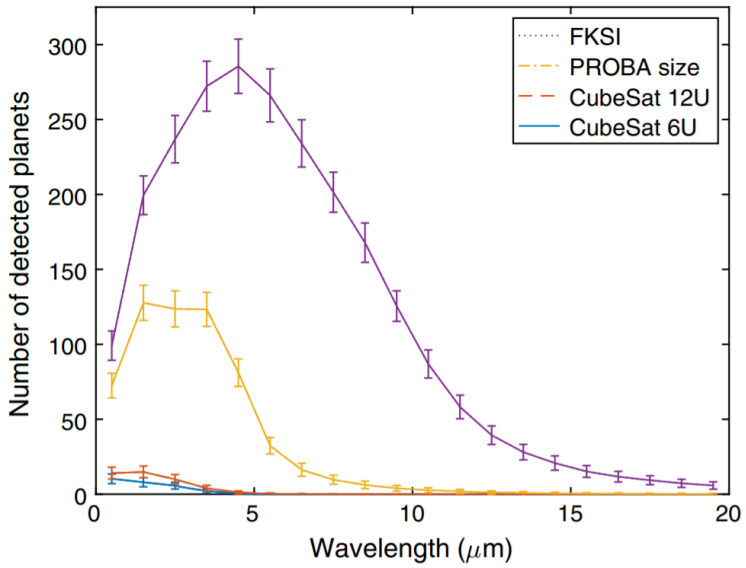

Figure 4.2: Representation of the mean potential number of detected planets for four different configurations with at least a SNR of 5 and a integration time of 24 h. Platform stability constraints (tip/tilt and OPD) are not considered. The resolution parameter $R = 1.2$. The error bars represent the standard deviation [19].

Each mission detects different planet types based on their physical parameters and therefore has a different optimum operating wavelength range. In agreement with the results of Figure 4.2 for a PROBA-size satellite, the scope of monitored wavelengths will firstly be restricted from 1 to 5 μm and might be subject to later changes if required.

Furthermore, in addition to defining the spectral range of observation, we have also kept the compactness of the design as a driving requirement. Thus, the main objective is not to maximise the number of exoplanets detected but first to limit the dimensions of the system (and indirectly therefore the costs) and to determine the associated performances. Thus, we decide to initially

set the arm length of the interferometer at 2 m and the size of the primary mirrors at 20 cm. The work now consists, based on these constraints, of maximising the performance of the system and determining the stellar systems that it is capable of observing. The first step will therefore be to characterise each of the optical components of the telescope as well as its general structure. The second step will aim to determine the performance of the telescope. In particular, its robustness, throughput, coupling efficiency, and detection capability will be investigated. The last step will finally focus on the analysis and variation of the different parameters defined initially, such as wavelength and magnification, and particularly the impact that they have on the performance of the system.

4.2 Interferometer structure

The design of a functional spacebased interferometer involves the specification of each of the different optical elements that make up the complete instrument. The general structure of the dual arm interferometer chosen for this work can be represented by the scheme shown on Figure 4.3.

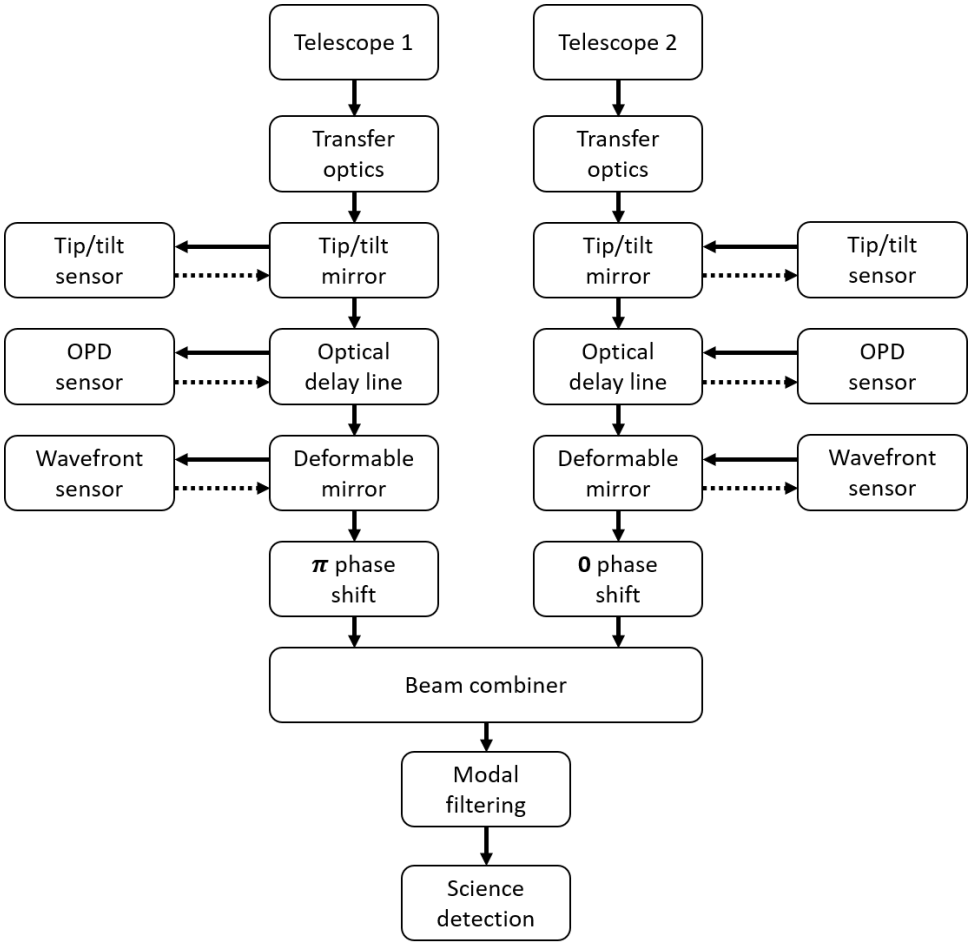

Figure 4.3: Representation of the structure of the interferometer considered for this work. Each of the two arms is symmetrical and is equipped with its own tip-tilt mirror, delay line and deformable mirror. Then a phase shift is applied to one of the arms before recombination. Modal filtering is applied to both arms thanks to the use of a single-mode fibre. This modal filtering can be considered before recombination. The science detection box is not discussed in this work and includes the spectrograph and detectors components.

The light is first collected by the primary mirrors and the beam is reduced to a diameter that can be used to make various subsequent beam deflections and corrections. Then several mirrors can be used to redirect the light beam to the centre of the satellite where the scientific measurements are made. Once the light is centralised in the satellite, various correction stages can be started (in a variable order depending on the mission). In our case, the beam from each of the telescopes is first reflected by a tip-tilt mirror that corrects for propagation direction errors. It is controlled by a sensor that measures the angle of deviation from the nominal propagation of the incident beam. The potential path difference between the two arms of the interferometer is then measured by an optical path difference (OPD) sensor and corrected through the use of an optical delay line. In addition, wavefront deformations may occur and will also have to be subsequently corrected by a deformable mirror responding to the measurements made by an associated wavefront sensor. Once each beam has been adequately corrected for their wavefront and propagation errors, they are recombined using a beam combiner. In nulling interferometry, an achromatic π phase shift is applied to one of the beams to produce the desired phase opposition in the line of sight and therefore suppress the starlight. At the output of the combiner, a

modal filter can be added to improve the quality of the wavefront before focusing on the detector. Depending on the system, two outputs can be monitored consisting of a destructive (dark output) and constructive process (bright output).

Each of these different steps necessary for the operation of the interferometer will be described and detailed in the following sections. The choices made as the design progresses will have an impact on its final performance, which will be discussed in the next chapter. Besides, since the interferometer considered is symmetrical, the rest of the work will focus on the study of one single arm (the right one). The results obtained are therefore transferable to the other arm as well (the left one).

4.3 Telescope design

Before investigating the optical performance and aberrations, the process through which the light beam is brought to the centre of the satellite and then reduced to a smaller collimated beam, with which it is possible to carry out scientific measurements, has to be defined. Several missions have shown a similar strategy where the primary mirror consists of a flat siderostat with a 45-degree angle deviating the light toward the centre of the satellite before achieving the beam reduction (cfr. FKSI and PEGASE). This configuration, in addition to having an easy implementation, reduces the possible aberrations induced by the primary mirror since its surface is flat and thus easier to manufacture than more complex mirror shapes with strong optical power. Nevertheless, it has the inconvenience of redirecting a very large beam toward the satellite centre, making the secondary mirror as large as the first. Such configuration decreases the compactness of the design as well as increases the satellite total weight which can impact the production, launch, and operating costs as well as the dynamic stability of the system.

Another solution for the light collecting process involves therefore to directly use mirrors with optical power. A wide variety of telescopes exist with different configurations. However, telescopes with obstruction of the light path (such as Newton or Cassegrain telescopes) will be discarded at first since such obstruction decreases the amount of light passing through the system and thus hinders the detection of small faint objects. This implies the use of off-axis telescopes where the secondary has been moved out of the optical path.

Moreover, the objective is not to bring the light directly to a focus but to achieve the collimation of the light into a beam of reasonable width. The simplest configuration required to reach this purpose is made of two confocal, off-axis parabolas.

The different steps of the design described hereafter have been implemented in the optical ray-tracing software CodeV and the performance has been assessed based on the study of aberrations, light-collecting and focusing capabilities.

4.3.1 Primary mirror design

Since the structure is a Bracewell-type interferometer and the objective is to simplify the design as much as possible by minimising the number of optical surfaces, the concept chosen will use parabolic mirrors to directly focus the light beam. This allows an immediate reduction of the beam width and thus a smaller secondary mirror. This avoids having to work with an additional reflecting surface used for redirecting the beam toward the satellite centre before performing the beam reduction. Such a design involves that a very wide beam propagates along the base of the

interferometer, which also implies large optics and therefore an increase in the overall weight and dimensions of the satellite. Furthermore working with a parabolic mirror directly allows to get rid of the spherical aberration. However, to validate the use of a primary parabolic mirror, its curvature and orientation must be defined. Two configurations are possible here. The first one collimates the beam at the end of the arm, as shown on Figure 4.4.

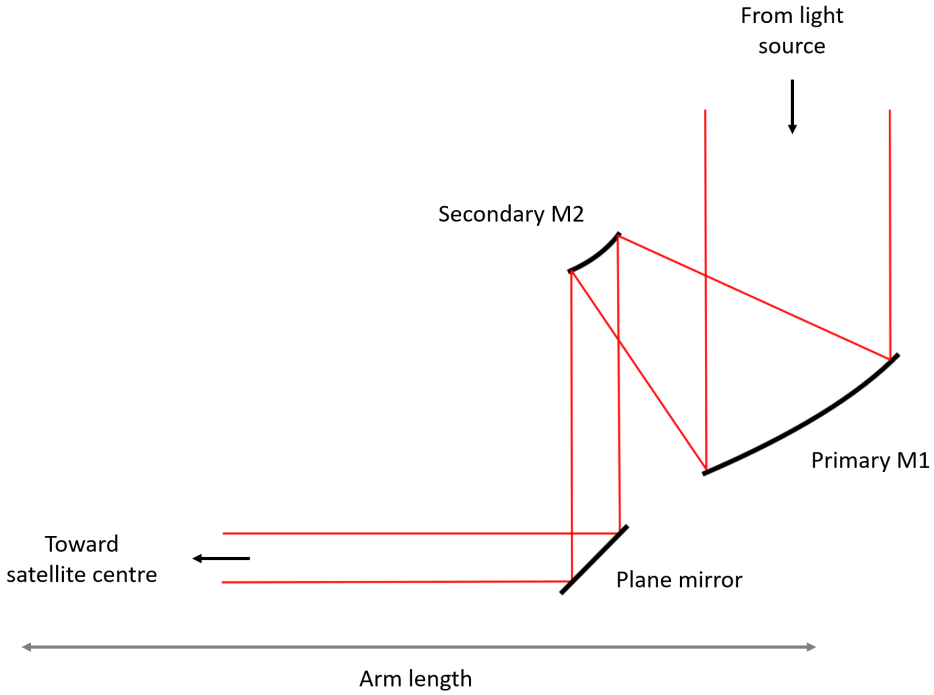

Figure 4.4: Representation of the first configuration for the interferometer right arm. It consists in the use of two afocal mirrors reducing the beam width at the tip the interferometer arm before redirecting the light towards the satellite centre.

The design is then optimised to be as compact as possible and several examples are presented in Luca Shifano's work [49]. The two parabolas have to be placed in such a way that the angle of reflection of the beam is minimised. This limits the beam polarisation which can in some situations be detrimental for detection. A third plane mirror completes the system to redirect the light towards the centre of the satellite where the interferential measurements are performed. Although this design is functional, it has one main drawback. The fact that the three mirrors used to collimate and redirect the light beam are positioned at the end of the arm generates an important mechanical lever arm, much larger than if all the optics were centralised. To avoid oscillations, and therefore decrease the sensitivity to mechanical vibrations that could degrade the detection, a solid structure made of a very robust material is required. This implies an increase in the weight of the structure that could also impact fuel consumption during manoeuvres, making the satellite more expansive to operate..

Furthermore, the radius of curvature of the mirrors impacts the system sensitivity to aberration. As a matter of fact, we consider 2 mirrors M_a and M_b such that they both have different radius of curvature $R_a = 100$ mm and $R_b = 1000$ mm. Assuming that the manufacturing imperfections are independent of mirror shape and surface curvature, we can fix the absolute curvature error to be $\Delta R = \pm 1$ mm. Therefore, the effective focal length of both mirrors $f_{a,b} = R_{a,b}/2$ will vary by 2% and 0.2% for M_a and M_b respectively. This highlight the fact that manufac-

turing imprecisions are more impacting mirrors with a smaller radius of curvature and therefore smaller focal length. This makes it desirable to move towards maximisation of the focal length. According to *Claudia Brückner et al.,2010* [50], within the off-axis apertures, the 90° deviation is the one that enables the highest possible focal length at a given aperture diameter.

This is why a second configuration is studied. It is based on the simple idea of adapting the curvature and orientation of the primary so that it focuses on the centre of the satellite, therefore generating the 90° deviation maximising the focal length. This allows the secondary to be placed at the centre of the satellite which maximises its compactness compared to a decentralised system or a system using a flat primary mirror. This also allows for better alignment of the mirrors as mechanical vibration and bending errors only affect now the primary mirror compared to the first configuration where the secondary mirror and tip-tilt mirror were subject to arm bending and mechanical vibration. Finally, the lever arm and the total weight are also reduced, which decreases the satellite inertia and fuel consumption. Additionally, this design, illustrated in Figure 4.5 , facilitates the creation of a focus upstream of the secondary mirror, which allows the addition of a field stop. This field stop could be used to limit the different field angles propagated by the system and therefore the stray light reaching the detector.

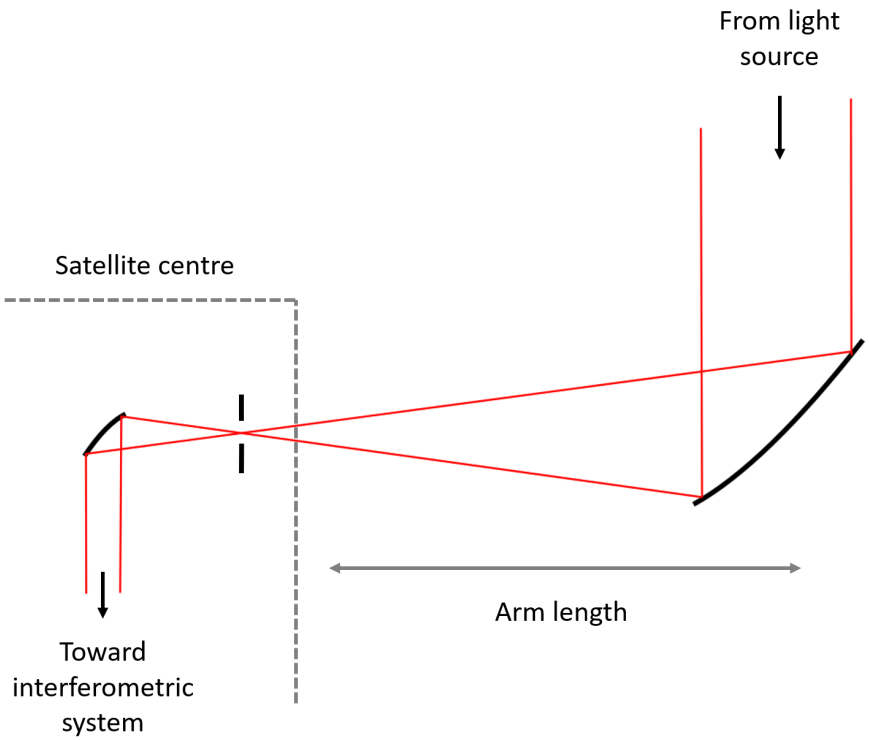

Figure 4.5: Representation of the second configuration for the interferometer right arm. It consists in the use of two afocal mirrors with a common focus designed to reflect the light with a 90° angle. The light is therefore directly redirected towards the satellite centre without the use of a third optical surface. The passage of the beam by a focal point allows the addition of a field stop limiting the field angles propagated in the interferometer.

The characteristics of the primary mirror, according to the configuration illustrated on Figure 4.5 are summarised in Table 4.3.

Apparent focal length	2 m
Diameter	20 cm
Effective focal length	1 m

Table 4.3: Primary mirror characteristics.

The mirror has a parabolic shape described by the following expression:

$$y = A \cdot x^2 \qquad \text{with coefficient A} = 0.25.$$

4.3.2 Secondary mirror design

The beam must be collimated after reflection on the secondary mirror to be able to make the various optical corrections necessary before recombination. Thus, the shape of this mirror is directly depending on the profile of the incident wavefront. However, there is still a degree of freedom regarding its curvature, which allows the width of the collimated beam to be adapted at the output. Since this mirror is not considered as a deformable one, the work consists therefore in defining which beam size is the most appropriate for our system in order to design this second mirror. Assuming that the beam propagation exhibits a Gaussian profile limited by diffraction allows expressing its divergence according to the following equation

$$\theta = \frac{\lambda}{\pi\omega}, \tag{4.1}$$

where λ is the propagating wavelength and ω described the beam half-width minimum, which is often called the "waist" of the beam. As a matter of fact, the intensity of the beam decreases in a Gaussian manner as one moves away from the axis of propagation. The waist is thus defined as the distance from the propagation axis where the intensity as dropped to a value of $1/e^2$. The divergence of a light beam in terms of its waist is shown on Figure 4.6.

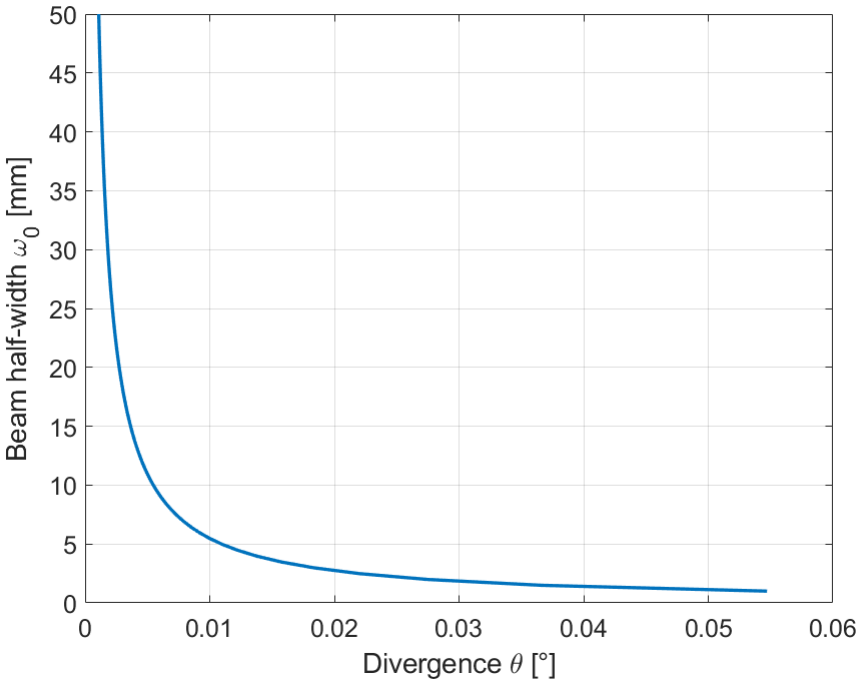

Figure 4.6: Gaussian beam divergence in function of beam diameter.

It can be seen that a very large beam-half width involves a tiny divergence and that a very narrow beam experiences stronger divergence effects. In this work, the compactness of the system is one of the main objectives and it is linked to the minimisation of mirror dimensions. Therefore, a very large beam with low divergence is not more adapted than the narrowest one with a large divergence as both will require large optical components. A trade-off limiting both impacts is thus made, and 3 different beams are considered whose characteristics are listed in Table 4.4.

Output beam diameter	4 mm	1 cm	2 cm
Beam divergence	0.0274 deg	0.0109 deg	0.0055 deg
Apparent focal length	40 cm	10 cm	20 cm
Mirror diameter	$\sim$ 4 mm	$\sim$ 1 cm	$\sim$ 2 cm
Effective Focal Length	20 cm	5 cm	10 cm

Table 4.4: Secondary mirror characteristics.

Since no information allows, for now, the selection of one specific beam diameter, the rest of the work will simply consider compactness to be the biggest issue to address. Therefore, the 4 mm beam is selected as a first choice and if it utterly leads to a significant decrease in the system performance, cost, or compactness, then the diameter will be adapted.

4.4 Tip-tilt mirror

The role of the tip/tilt mirror is to correct deviations in the direction of propagation of the light in the optical system. As a matter of fact, a satellite is oriented in space thanks to actuators and sensors, which all have a limited accuracy impacting the stability and the degree of precision with which the satellite's orientation is known and maintained. The resulting pointing errors can greatly impact the quality and detection rate of an on-board optical system. Therefore, they must be taken into account in the design to ensure an acceptable and controlled range of orientation error. Some of the sensors and actuators that are typically used in satellite attitude determination and control are listed in Table 4.5 and Table 4.6 respectively with their related accuracy.

Sensor	Performance [deg]	Availability
Gyroscope	0.003 to 1/h (drift)	Continuous coverage
Sun Sensor	0.005 to 3 (angle that the Sun subtends)	Outside of eclipse (intermittent use)
Magnetometers	0.5 to 3 (variability and uncertainty of the magnetic field)	Continuous coverage, but below 6000 km
Horizon Sensor	0.05 to 1 (Earth oblateness + fuziness of horizon)	Continuous coverage
Star Tracker	0.0003 to 0.01	Not blocked by the Earth or the Sun in the FoV (intermittent use)

Table 4.5: Overview of Sensors available in space and there performance.[51]

Actuator	Performance [deg]	Availability
Thrusters	0.05	Used in any environment, but needs propellant (limits lifetime)
Magnetorquers	1-5	Need a strong magnetic field (near Earth usage)
Reaction Wheels	0.005	Used in any environment, but need external torque device for momentum damping
Control Moment Gyros	0.005	Used in any environment

Table 4.6: Overview of space available actuators and their performance [52].

Actuators and sensors performance vary according to their weight and power. The elements used for active attitude determination and control of a satellite depend on its mission purpose. In recent years, technological advancement has allowed the ADCS components size reduction while maintaining if not enhancing their performance. With the increasing demand for small satellites conception which provides missions cost reduction, standardisation of the equipment and reduction of delivery times, miniaturisation of ADCS has allowed the production of small satellites with impressive pointing capabilities. A clear evolution of pointing accuracy for small satellites during recent years is illustrated in Figure 4.7.

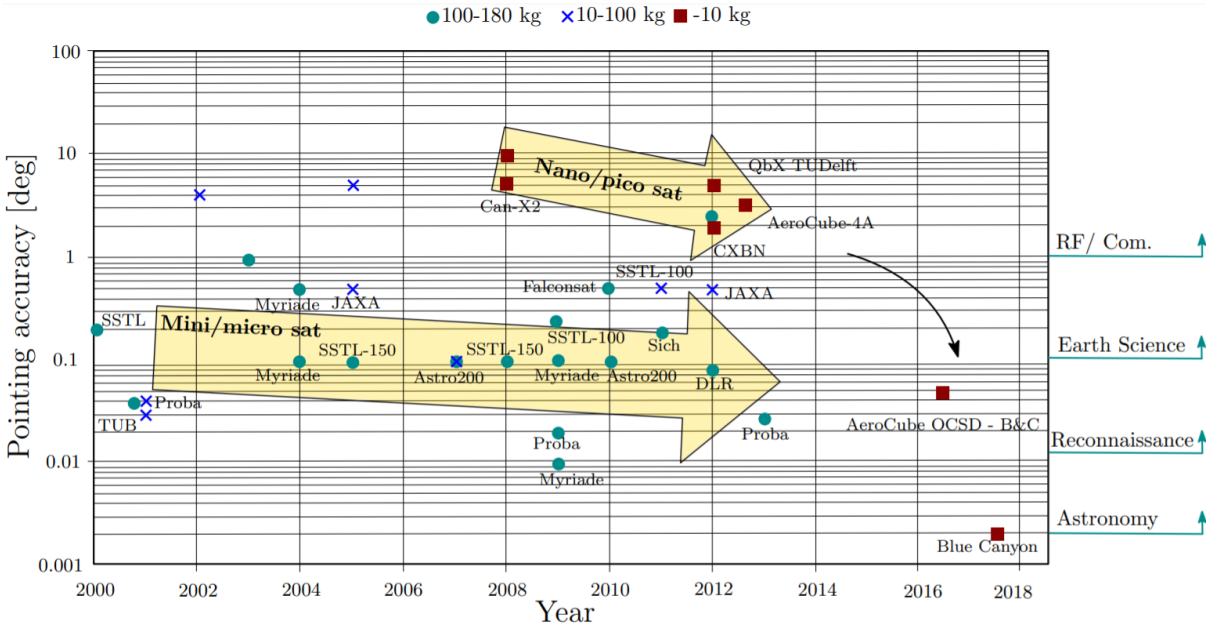

Figure 4.7: Evolution of small satellite pointing capabilities throughout the years [53].

It can be noticed that for a satellite having dimensions similar to PROBA-type spacecraft (100-180 kg), represented by green dots, the typical pointing accuracy is around $0.02 - 0.03$ degrees. Since the system to be conceived in this paper is designed to remain in this mass range, the pointing capabilities of the spacecraft are assumed to be as good as the one for the PROBA satellites. Thus, we will consider for now the satellite pointing errors to be comprised within $\pm 0.03°$ around the line of sight.

The implementation of the tip-tilt mirror goes with the use of a wavefront sensor whose

different types are discussed in Section 4.8. This sensor detects variation in the angle of propagation of the light and sends the information to the tip-tilt device such that it will correct pointing anomalies. To limit the propagation of deflected beams due to pointing errors in the optical system, it is preferable to place the tip-tilt mirror directly after the reduction of the beam to the desired size. It is essential to work with fixed incidence beams (or at least with very little variation) to guarantee the optimal use of the optics and the maximum performance of the system while limiting aberrations and losses due to dispersion, diffraction or optical path difference. Thus, by adding the tip-tilt mirror right after the primary and secondary mirrors already defined, we obtain the structure shown in Figure 4.8.

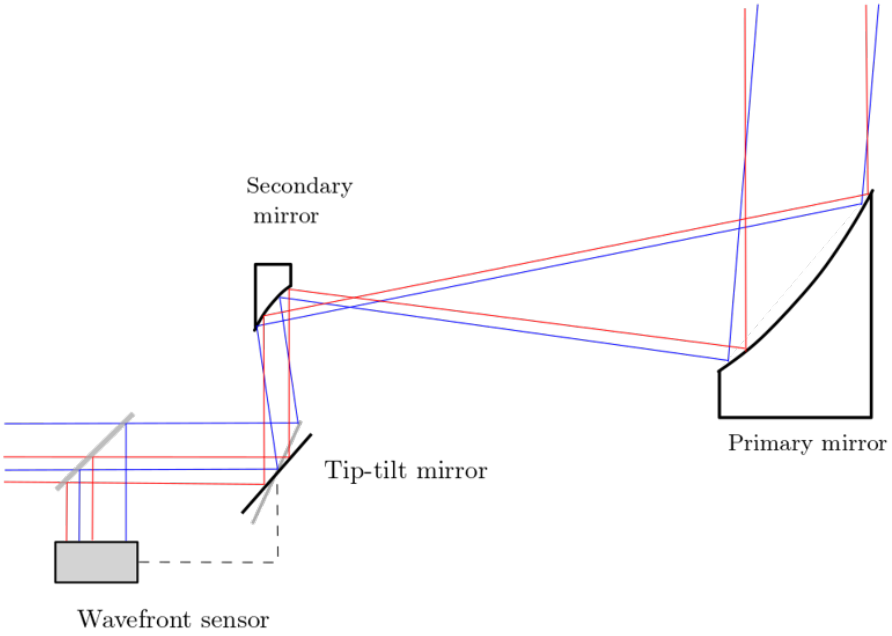

Figure 4.8: Utility of tip-tilt mirror in correcting the propagation direction of beams with initially inappropriate angle of incidence. The red rays correspond to nominal pointing while the blue are associated to a certain pointing inaccuracy. (The system is not to scale)

It is noticeable that after the tip-tilt mirror all beams propagate in the same direction. However, although the beams are parallels to one another, they do not superimpose. Depending on the correction angle applied by the tip-tilt mirror, they will actually be offset from the main optical axis. This deviation should be quantified and limited if it is proven to be detrimental to the system's performance.

4.5 Delay line

The path length between the two arms of an interferometer needs to be precisely known to guarantee the conservation of coherent recombination at the telescope detector. Furthermore, depending on the pointing situation, the light from an off-axis source will travel different distances before reaching each arm of the interferometer. This variation in the path length can also be caused by variation in the index of refraction of the crossed media. It thus needs to be corrected by an optical tunable delay line. Fortunately, for a space-borne interferometer, the light path variations are much smaller than for on-ground telescopes which are subject to strong atmospheric turbulences. Therefore the optical path length that must be corrected by

the delay lines is generally smaller, involving more compact delay line systems. Nonetheless, the instrument must be able to reach a high level of accuracy, much smaller than the observing wavelength. The management of the delay is done by imposing additional reflections on the beam to be delayed as shown in Figure 4.9. By linearly displacing two 45° mirrors placed on a mobile part, we can manage the distance that the beam travels and thus delay it by a specific amount of time.

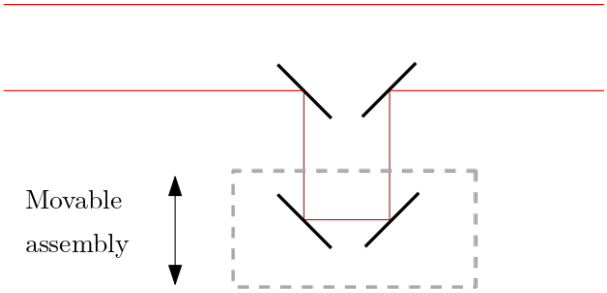

Figure 4.9: Delay line illustration.

4.6 Aberration Theory

The image quality of a telescope is severely limited by the quasi-static errors inside the telescope itself and by the very dynamic atmospheric turbulence of the atmosphere inside and outside the optical system. While the quasi-static errors can be managed by active-optics, the second limitation requires adaptive optics to overcome these aberrations to ultimately obtain near diffraction limit detection. Although the use of spaceborne telescopes limits the impact of the atmosphere, external deformations of the wavefront can influence the detection quality such as temperature gradients or mechanical stresses.

Aberrations affecting an optical system can be either chromatic or monochromatic. The first category is caused by the fact that the focal length of a lens depends on the refractive index. And this refractive index is varying with the wavelength of light going through it. Therefore different wavelength can be focused at different distances (longitudinal aberration) or different position (transverse aberration) on the focal plane. This type of aberration does not apply to mirrors which is one of the main reasons why mirrors are used in astronomy instead of lenses.

Nevertheless, even though the use of mirrors allows the cancellation of chromatic aberrations, it does not suppress the monochromatic ones. These aberrations are typically related to the paraxial approximation which is derived from the Gaussian Beam formalism and allows to simplify propagation equation to the first order. The light is considered as a geometrical ray whose deviation from the optical axis is small such that $\sin(\theta) = \theta$ where θ is the beam divergence. However, such simplifications do not account for certain optical effects such as diffraction and interference. Nevertheless, this formalism allows the definition and quantification of wavefront deviations from their nominal shape and therefore the characterisation of errors.

4.6.1 Strehl ratio

The Strehl ratio is a criterium for quantifying the resolving power of an optical system. In imaging optics, when a beam is focused, a PSF (point spread function) is observed which corresponds to a deformation of the Airy disk due to aberrations. These distortions are manifested

by a loss of intensity at the maximum of the function and by the amplification of the secondary lobes. The Strehl ratio corresponds to the ratio of the maximum illumination of the PSF and the Airy disk. This ratio is therefore comprised between 0 and 1. According to the Marechal approximation, it is written

$$S = \exp(-\sigma^2) \tag{4.2}$$

where σ is the standard deviation of the wavefront from its diffraction limited structure. The wavefront maximum distortion for a null depth of 10^{-6}, obtained in Section 2.2.3 was reduced to $\sigma = 6.3 \cdot 10^{-2}$ rad thanks to the use of a single mode fibre. This gives a Strehl ratio of $S = 0.996$. Therefore, we see that requirements on optics quality remain stringent since the Strehl ratio is very high (close to the ideal case where $S = 1$).

4.6.2 Zernike polynomials

Typically, the distortion of the wavefront is defined in terms of phase error across the pupil $\Phi(r, \theta)$ as representend on Figure 4.10.

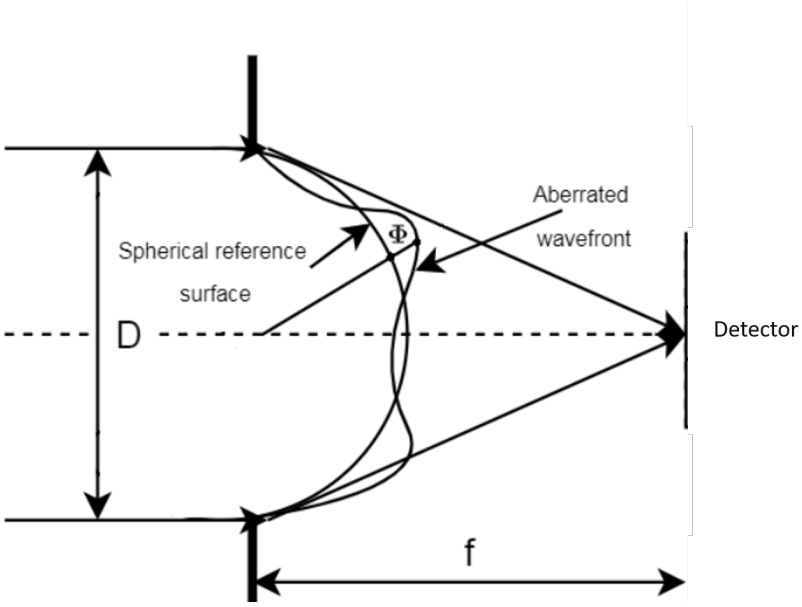

Figure 4.10: Illustration of wavefront distortion at the focus of a telescope where f is the focal length and D the pupil diameter. The ideal diffraction limited wavefront is represented by the spherical reference surface. The aberration function Φ describes the difference between the aberrated wavefront and the reference one [54].

Such phase errors are usually defined as a linear combination of Zernike circular polynomials, Z_i, representing different aberration types such that

$$\Phi(r, \theta) = \sum_{i=1}^{\infty} a_i Z_i(r, \theta), \tag{4.3}$$

where a_i designates the weight associated to a specific Zernike polynomial Z_i and (r, θ) are polar coordinates. These polynomials are defined on a unit circular aperture without obstruction and are well suited to aberration theory since low-order Zernike polynomials have a similar structure to common aberrations such as tilt, defocus, coma, astigmatism or spherical aberrations. A

review of the properties of the Zernike modes relevant to the description of atmospherically distorted wave-fronts can be found in a paper by *Robert J. Noll* [55]. Using polar coordinates (r, θ), the Zernike modes are defined by:

$$\begin{aligned} Z_i(r,\theta) &= \sqrt{n+1}R_n^0(r), && \text{if } m = 0, \\ Z_i(r,\theta) &= \sqrt{n+1}R_n^m(r)\sqrt{2}\cos(m'\theta), && \text{if } m > 0 \text{ and } i \text{ is even}, \\ Z_i(r,\theta) &= \sqrt{n+1}R_n^m(r)\sqrt{2}\sin(m'\theta), && \text{if } m < 0 \text{ and } i \text{ is odd}, \end{aligned} \tag{4.4}$$

where

$$R_n^m(r) = \sum_{s=0}^{(n-|m|)/2} \frac{(-1)^s(n-s)!}{s!\,[(n+|m|)/2-s]!\,[(n-|m|)/2-s]!} r^{n-2s}. \tag{4.5}$$

The index n is called the radial degree, the index m the azimuthal frequency. The radial coordinate r goes from 0 to 1, θ is the azimuthal coordinate and range from 0 to 2π. The values of n, m are integers respecting $m \leq n$ and $n - |m| =$ even. Therefore, only polynomials with a particular combination of (n, m) exist and form the so-called Zernike modes. The index i is a usual ordering number where even i values correspond to cosine terms. The 12 first Zernike polynomial along with their 2D representations are given in Table A.1 and Figure A.2 of the Appendix for the reader convenience. One particularity is that every polynomials are orthogonal to one another and their integration over the pupil surface always makes zero except for the piston aberration (Z_1). Therefore, the mean phase value, the RMS, and the phase variance can be computed such that:

$$\begin{aligned} \langle\Phi\rangle &= \frac{1}{\pi}\int_0^1\int_0^{2\pi}\Phi(r,\theta)r\,dr\,d\theta = a_1, \\ RMS &= \sqrt{\langle\Phi^2\rangle} = \sqrt{\sum_{i=1}^{\infty}a_i^2} \\ \sigma &= \langle(\Phi - \langle\Phi\rangle)^2\rangle = \sum_{i=2}^{\infty}a_i. \end{aligned} \tag{4.6}$$

4.7 Deformable mirrors

Adaptive optics works by measuring the distortions in a wavefront and compensating for them with a device that corrects those errors such as a deformable mirror or a liquid crystal array. It thus actively shapes the telescope's mirror to convey an optimal wavefront shape and improve the system performance. Adaptive optics should not be confused with active optics, which works on a longer timescale to correct the primary mirror geometry.

By introducing the appropriate mirror deformation, the distorted incoming wavefront can be improved, as illustrated in Figure 4.11 where the signal is separated in two by a beam splitter. The system precision is at its maximum when the wavelength being sensed is equal to the one measured for scientific purpose. It ensures the exact knowledge of the wavefront structure at this specific wavelength. However, this implies a splitting of the signal of interest in two different parts, one for the wavefront sensor and one for the scientific measurements. Therefore, some of the precious photons of interest are not reaching the final detector which decreases the signal to noise ratio. One solution is therefore to operate the adaptive-optics-sensing system at a different

than the one used for the scientific analyses. This results in a decrease in precision since the wavefront deformation is chromatic. However, *B. Hogge & R. Butts, 1982* [56] have shown that it is still a practicable technique as the phase variance generated is considerably small and manageable. In a closed-loop system, the wavefront sensor measurements are recorded by a control system which sends an adapted response to the adaptive system, changing thus the mirror surface's shape. Alternatively, the shape of the mirror can be derived from a set of pre-calculated or stored profiles and this becomes hence an open-loop system.

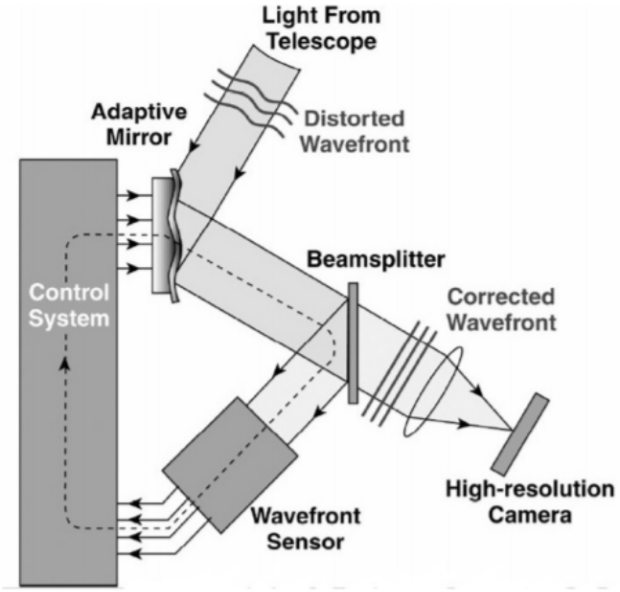

Figure 4.11: Adaptive optic system overall structure [54].

The quality and accuracy with which a wavefront can be corrected depend firstly on the actuation technology used. Deformable mirrors can either be segmented or continuous. Segmented mirrors have many smaller rigid mirror sections that can be controlled individually. The larger the number of segments, the more precise the control of the mirror shape. Tip–tilt mirrors are, for instance, segmented mirrors having only one segment which can tip and tilt, rather than having an array of multiple segments that can tip and tilt independently. The segments are positioned by actuators using pistons, even sometimes tip-tilt (illustrated in Figure 4.12a), values or Zernike coefficients. The main drawback of segmented mirrors is their high fitting error compared with a continuous face-sheet deformable mirror with the same number of actuators. If the elementary mirror is activated by a sole actuator, the motion is therefore limited to piston. Another drawback is that between the mirror segments, they are necessarily some gaps, which cause some loss of light and edge diffraction effect. Additional diffraction losses can arise when neighbored mirror segments are set such that a step arises on the surface.

Oppositely, continuous membrane mirrors consist of a single surface that can be deformed at different spots, which minimises the fitting errors. There are several actuation options for continuous surfaces, ranging from the mechanical actuator to magnets or piezoelectric elements. These actuation technologies are presented in Figure 4.12b and are discussed hereafter.

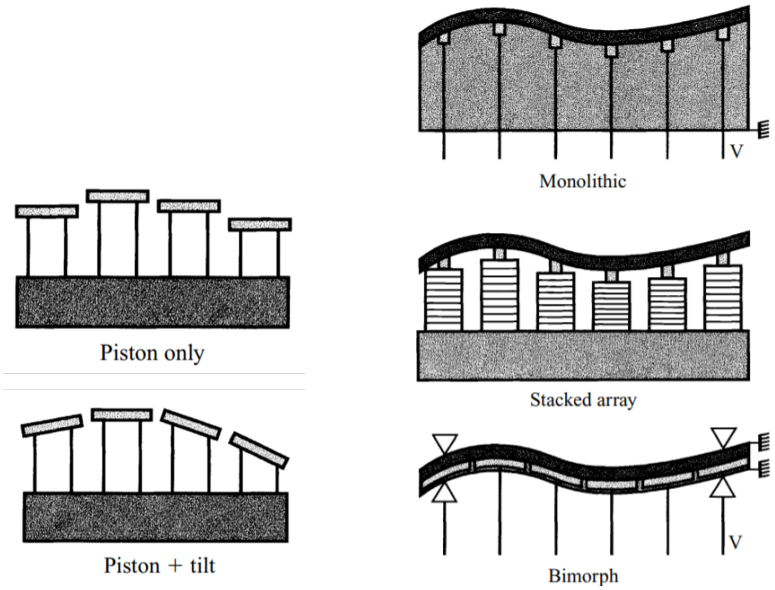

(a) Segmented deformable mirror

(b) Continuous deformable mirror.

Figure 4.12: Representation of various actuation technology [57].

4.7.1 Monolithic piezoelectric mirrors (MPM)

Such type of mirror uses a thin reflecting glass plate bonded to the upper face of a monolithic piezoelectric disk. A set of actuators is represented on the upper surface by an electrode network and the electrical wires pass through holes made in the disc. When a voltage is applied to an electrode, mechanical deformation is induced in the piezoelectric materials which translate into a deformation of the mirror. Piezoelectric materials are almost insensitive to temperature, but the main drawback of a MPM is its small stroke (< 2 μm) limiting the utilisation to small-sized telescope [57]. Furthermore, a significantly thick block of piezoelectric material is required for the deformation to only occur at the mirror surface and not at the bottom [58].

4.7.2 Stacked array mirror

Stacked array deformable mirrors are using ferroelectrics actuators made of stacks of individual plates or disks. It uses the inverse longitudinal piezoelectric effect to elongate the pole ceramic and thus deform the mirror resting on it. The procedure is very similar to the one used for MPMs except that here the issue of small stroke is handled by stacking multiple PZT(Lead zirconate titanate) plates on top of each other. This amplifies the elongation proportionally to the number of plates used. For instance, PZT actuators made out of 40 plates can provide a $\pm 5\mu$m stroke for a ± 400 V control voltage [59]. They are easily manufactured allowing massive production and cost reduction.

4.7.3 Bimorph mirror

A bimorph mirror consists of two piezoelectric ceramic plates bonded together and polarised in opposite directions, parallel to their axis. A network of electrodes is placed between the two plates. Their front and bottom surfaces are grounded. When a voltage is applied to one electrode, one plate contracts locally and laterally while the other plate expands. This is called

a bimorph effect giving rise to mirror bending. A disadvantage of this solution is its sensitivity to temperature changes and the high driving voltages requiring bulky electronics racks.

4.7.4 MEMS mirror

Micro-Electro-Mechanical Systems concepts are based on the use of a thin mirror membrane attached to an intermediate flexible support actuated by electrostatic or electromagnetic fields. It is based on a scalable array of parallel plate electrostatic actuators, fabricated in silicon by discontinuous semiconductor processing. Each square actuator plate is rigidly connected to the substrate along with two of its edges and is suspended above an addressable electrode as illustrated in Figure 4.13. The voltage applied to that electrode imposes an electrostatic attractive force on the electrically grounded actuator plate, causing it to bend toward the substrate.

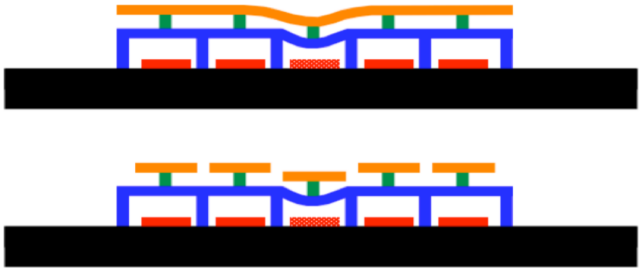

Figure 4.13: MEMS deformable mirror concept. [60].

They all share the characteristics of sub-millimetre pitch, low power consumption, capabilities of a very high number of actuators, and low mass. When the actuation is based on an electrostatic field, the displacement of the membrane is proportional to the square of the applied voltage and requires applying up to 200 V to get a 5 to 8 μm stroke[59].

Besides cost reduction and compactness, one important interest in MEMS technology is the scaling capability of up to thousands of actuators within a relatively small mirror device. The main drawbacks of this technology are the small inter-actuator pitch and the limited stroke. This makes them more appropriate for a small telescope with a small aberration range needing very precise correction. All in all, the choice of a deformable mirror depends on several optical parameters such as the mechanical stroke required to correct stronger aberrations, the number of actuators needed for complex shape reproduction (which defines the number of degrees of freedom of the system) as well as the dimension of the mirror to deform and of course the manufacturing costs.

Boston University (BU), in partnership with Boston Micromachines Corporation (BMC) commercialise MEMS DM systems (including driver) at about 150$ per actuator, which is one-tenth that of conventional deformable mirrors (1500$/actuator) [60]. Considering in addition their sub-nanometer repeatability, sub-nanometer stability, and sub-nanometer hysteresis over a wide range of operating conditions, MEMS deformable mirrors seem an excellent choice for this project. In fact, such devices have already flown to space with missions like PICTURE [61] (in 2015) and DeMi [62] (in 2020) where the latter was carrying a 5 mm wide MEMS DM which incorporated 140 actuators.

4.8 Wavefront sensors

A deformable mirror cannot function properly without a system sensing the aberrations to be corrected. This is the purpose of a wavefront sensor which provides a direct measurement of the phase and intensity of the wavefront. The most common type of wavefront sensor is the Shack–Hartmann wavefront sensor (SHWFS), which is based on the determination of the angle of arrival of the rays, which corresponds to the local slope of the wavefront or expressed more mathematically, its spatial first derivative (the gradient). Another technique, measures the second derivative of the phase (its Laplacian) and is called curvature sensing and therefore uses curvature sensors.

The control system is typically a specialised computer that calculates, from the wavefront sensor measurements, the commands to be sent to the deformable mirror actuators. For ground-based measurements, the calculation must be performed quickly (within 0.5 to 1 ms), otherwise, the state of the atmosphere may have evolved, making the wavefront correction inaccurate. For space satellites, the time response can be more relaxed. As in active optics systems, zonal or modal control methods can be used. In the case of zonal control, each zone or segment of the mirror is independently controlled by wavefront signals that are measured for the sub-aperture associated with that zone. In the case of modal control, the wavefront is expressed as the linear combination of the modes that best fit the atmospheric disturbances. The basic requirements for an adaptive optic wavefront sensor are high quantum efficiency, very low readout noise, ability to take very short exposures and fast readout speed.

4.8.1 Shack-Hartmann wavefront sensor (SHWFS)

This sensor is fabricated with a microlens array mounted in front of a CCD or CMOS detector array as illustrated in Figure 4.14. When a planar wavefront is incident on the sensor, each lenslet focuses the light at the centre of a predefined set of detector pixels located at the focal plane of the lenslet matrix. This generates a grid of equidistant focal spots. When a distorted wavefront arrives on the microlens array, phase fluctuations alter the spots positions (the focal points are moved to different locations within the pixels of each lenslet). By analysing the locations of the individual points on the detector array, it is possible to retrieve the shape of the incident wavefront on the sensor. This information is then used to determine the deformation to be induced on the surface of the deformable mirror to correct the wave distortion.

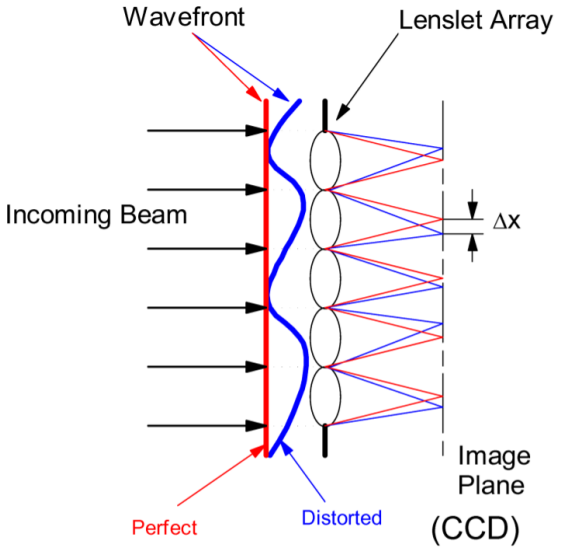

Figure 4.14: Shack-Hartmann wavefront sensor working principle [63].

The resolution at which phase variations can be measured across the wavefront is determined by the number of lenslets across the aperture. The number of lenslets is often determined by the likely signal-to-noise ratio as enough photons must reach each sub-aperture per exposure to determine the spot position. The best SHWFS can provide nanometric accuracy ($\sim \lambda/100$ rms). They are insensitive to vibration, have short response delays, and are considered achromatic across their dedicated spectral band.

4.8.2 Curvature wavefront sensor (CWS)

CWSs uses a lens with two out-of-focus images before (intra-focal) and after (extra-focal) the focal point as illustrated in Figure 4.15. A local wavefront curvature error makes the light converge closer to one plane than the other, producing an excess of illumination in this plane and a lack of illumination in the other one. The normalised difference between the two illuminations, therefore, provides a measure of the local wavefront curvature and allows its complete reconstruction. The result is insensitive to non-uniformities of the light distribution in the pupil plane since they produce a similar excess or lack of illumination in both planes that cancels out when taking the difference.

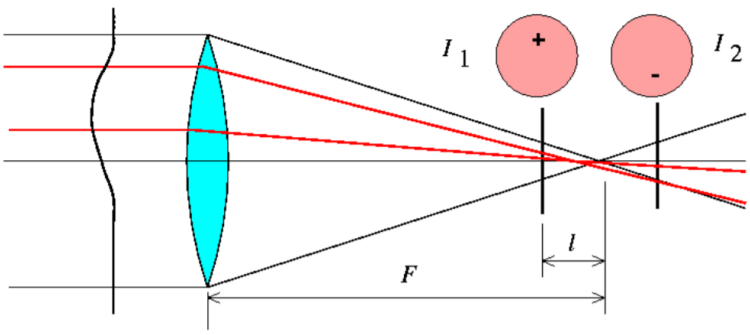

Figure 4.15: Curvature sensor illustration [63].

Theoretically, only one out-of-focus image is required, but using two of them offers the advantage of removing systematic errors such as readout and detection noise while cancelling out small scintillation effects [64]. As an alternative to using two imaging systems to obtain intra- and extra-focal images, a membrane can be employed to alternate between both positions. Unlike a SHWFS, a CWS detects modal aberrations and, although high order aberrations can be detected, it is better at detecting low order terms. Adaptive optics systems that use CWS generally arrange the deformable mirror actuators in a circular pattern, rather than the grid structure used by SHWFS.

4.8.3 Pyramid wavefront sensor (PWS)

PWSs work on the principle of the Foucault knife-edge test, with a pyramid lens placed at the focal point. The incoming light is focused by a lens onto the prism apex. The four facets of the pyramid split the incoming light into four beams, propagated in slightly different directions. Finally, a relay lens is placed behind the prism to re-image the four beams on a CCD camera. The aberrations in the wavefront can be determined from the intensity patterns over the four sub-apertures. Any distortion in the wavefront will cause the ray to fall predominantly onto one of the four sides, increasing the intensity in one sub-aperture and hence causing a reduction in the other three. However, even with a perfect wavefront, the intensity is distributed slightly differently inside each of the four sub-images I_{ij}, due to the different optical paths for each of the beams. This inequality in the intensity distribution serves as a starting point for restoring the wavefront perturbations. Dynamic circular modulation of the incoming beam, which can be accomplished either by oscillating the pyramid itself or by a steering mirror, allows increasing the linear and dynamic range of the pyramid sensor at the cost of a reduced sensitivity [65].

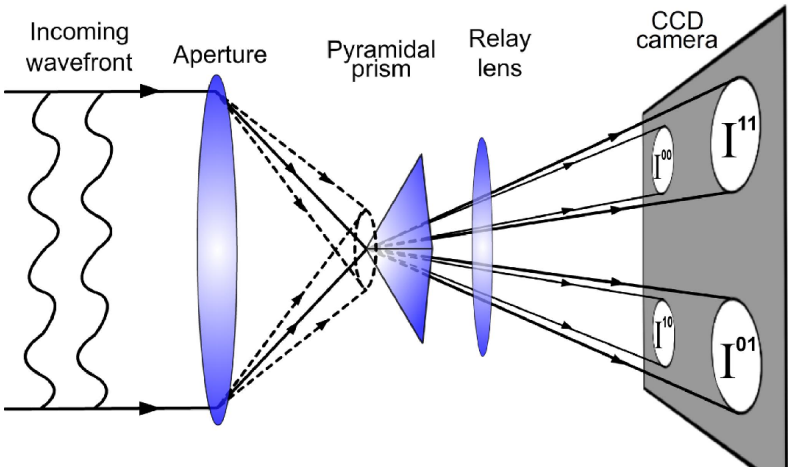

Figure 4.16: Pyramid wavefront sensor general structure [66].

It is similar to a SHWFS in dividing the beam into sub-apertures, but also comparable to a CWS in that it detects modal aberrations. PWS shows promising improvements over SHWFS since only four sub-apertures are required, reducing thus the number of photons needed for wavefront reconstruction. This will allow the use of lower magnitude stars as guide stars to eliminate atmospheric effects for instance.

4.9 Single mode fibre theory

An optical fibre is generally made of a cylindrical dielectric waveguide (nonconducting waveguide) that transmits light along its axis, over longer distances and faster than other mediums, by the process of total internal reflection. The fibre consists of a core surrounded by a cladding layer, both of which are made of dielectric materials.

The cladding material must be of a lower refractive index than the core such that if light travelling through the core eventually reaches the interface between the core and the cladding, it is reflected back into the fibre, rather than escaping, thanks to this difference in the refractive index of the two layers.

We have already mentioned the benefits of using fibres in the relaxation of the requirements on optical surface quality in Section 2.2.3. The fibre helps to achieve the desired null depth with reduced tolerances on the preceding optical components (in order to reduce manufacturing costs). We saw that larger phase errors were allowed while maintaining a null depth of $N = 10^{-6}$ thanks to the optical fibre intrinsic property to spatially filter the signal such that at the fibre exit it is only composed of the fibre propagated modes. Modes designate the transverse electric field distributions which remain constant during propagation in the fibre.

When a unique mode is propagated by the optical fibre, it is called a single-mode fibre, whereas when several modes can circulate inside it, then it is a multi-mode fibre. Physically, the main difference between the two is that the attenuation of multimode fibre is higher than SM fibre because of its larger core diameter. The fibre core of a single-mode cable is very narrow, so the light that passes through these fibre optical cables experiences less reflection, which keeps the attenuation to a minimum [67].

However, better wavefront quality thanks to fibre spatial filtering come at the expense of signal intensity. In fact, the shape of the electric field at a fibre exit remains the same whatever the incident wavefront structure, but the intensity retrieved at the end is inversely proportional to the incident wavefront deviation from the fibre propagated mode(s) shape. The efficiency with which the incident optical power is transmitted through the fibre is called "coupling efficiency" and is comprised between 0 and 1. Zeros coupling means no energy has been transferred from the incoming light beam to the fibre and the signal is lost. On the other hand, a coupling of 100% indicates that the incident energy has been entirely transmitted through the waveguide and that, if it is considered lossless, the same amount of energy will be retrieved at the fibre end. Thus, to enable enough photons to reach the detector, the coupling efficiency "ρ" must be maximised.

4.9.1 Normalised frequency

The normalised frequency V, is an adimensional parameter helpful to determine if a specific optical fibre will be single mode or multi-mode for a certain wavelength. It is defined by

$$V = \frac{2\pi a NA}{\lambda}, \tag{4.7}$$

where a is the fibre core radius, NA its numerical aperture and λ the wavelength considered. For only one mode to be propagated by the fibre (the fundamental one LP_{01}), the condition $V \leq 2.405$ must be respected. If $V \geq 2.405$, then higher order modes can circulate through the

fibre which is thus qualified as multimode. $V = 2.405$ is defined as the fibre cutoff frequency V_c and correspond to the smallest frequency that supports LP_{11} mode.

The numerical aperture is defined by

$$NA = \sqrt{n_{core}^2 - n_{cladding}^2} \tag{4.8}$$

where n_{core} designates the index of refraction of the fibre's core and $n_{cladding}$ the one of the cladding. The numerical aperture typically characterises the acceptance cone of an optical fibre, which defines the range of incident ray angles that can be injected in the core of the fibre without light leakage in the cladding. It can be expressed as

$$\sin(\theta_{max}) = NA, \tag{4.9}$$

where θ_{max} is the maximum angle of incidence for optimal fibre transmission. Typical values of numerical apertures are between 0.20 and 0.29 for multi-modes [68] and between 0.10 and 0.14 for single-mode fibres [68]. A list of commonly manufactured single mode fibres is provided in Table 4.7

Manufacturer	Fiber type	Wavelength	NA
Fibercore	SM300	375 nm	0.12 - 0.14
Thorlabs	SM450	488 - 633 nm	0.10 - 0.14
Nufern	780-HP	780 nm	0.13
Thorlabs	SM2000	1700 - 2300 nm	0.12
Corning	SMF-28	1550 nm	0.14
MKS	F-SM980-4.5/80	980 - 1550 nm	0.11 - 0.13
MKS	F-SY-C	980 - 1550 nm	0.13 - 0.15
MKS	F-SM1500	1550 - 1650 nm	0.23 - 0.25

Table 4.7: Typical single mode fibres characteristics.

We can see that most single-mode fibres have a short operating wavelength range. Optimising a fibre over a large spectrum such that all the wavelengths are highly transmitted is very difficult. This has been highlighted by *Aït Hocine,2019*[54], the acceptable range of working wavelength for a single-mode fibre is $[\lambda_c, 2\lambda_c]$. At a higher wavelength, the losses become too important. Therefore, we will first restrict our observing wavelengths between 2 and 4 μm. Considering $NA = 0.16$ as a first approximation, we can thus determine the maximum fibre core radius a_{core} for which all the wavelengths will be propagating only via the fundamental mode (when $V \leq 2.405$). This maximum radius is obtained for the smallest wavelength considered $\lambda_c = 2$ μm which is also called the cutoff wavelength. We obtain

$$a_{core} = \frac{V_c \lambda_c}{2\pi NA} = 4.785 \ \mu m. \tag{4.10}$$

The fibre is effectively single mode over the spectral band since the cutoff frequency is comprised between 1.202 and 2.405 (for $\lambda = 4$ μm and 2 μm respectively).

4.9.2 Coupling efficiency

The shape of the fundamental mode propagated by a SMF is determined by solving Maxwell's equations with the correct boundary conditions. Each of these modes varies radially as a Bessel

function of the first kind ($J_0(r)$) in the core, and as a modified Bessel function of the second kind ($K_0(r)$) in the cladding. However, for the sake of simplicity, this behaviour can be approximated by a Gaussian profile [69] such that the electric field amplitude distribution can be written

$$E(r) \simeq E_0 \exp\left(-\left(\frac{r}{\omega_g}\right)^2\right) \tag{4.11}$$

where ω_g is a parameter representing the field radius of the fundamental mode. This parameter is chromatic and depends on the physical fibre's radius as described by the following equation [70]

$$\omega_g = a_{core}\left(0.65 + \frac{1.619}{V^{3/2}} + \frac{2.879}{V^6}\right) \tag{4.12}$$

with a_{core} the fibre core radius and V the normalised frequency. Based on this Gaussian approximation, the analytical expression for the coupling efficiency of the fibre in function of central obstruction α can be deduced [71] such that

$$\rho_\alpha(\beta) = 2\left[\frac{\exp(-\beta^2)\left(1 - \exp(\beta^2(1-\alpha^2))\right)}{\beta\sqrt{1-\alpha^2}}\right]^2 \tag{4.13}$$

with

$$\beta = \frac{\pi D \omega_g}{2\lambda f}. \tag{4.14}$$

In our case $\alpha = 0$ and Equation 4.15 becomes

$$\rho(\beta) = 2\left[\frac{\exp(-\beta^2) - 1}{\beta}\right]^2. \tag{4.15}$$

This function has a maximum at $\rho = 0.8145$ (81.45%) for a value $\beta = 1.1209$ as shown on Figure 4.17.

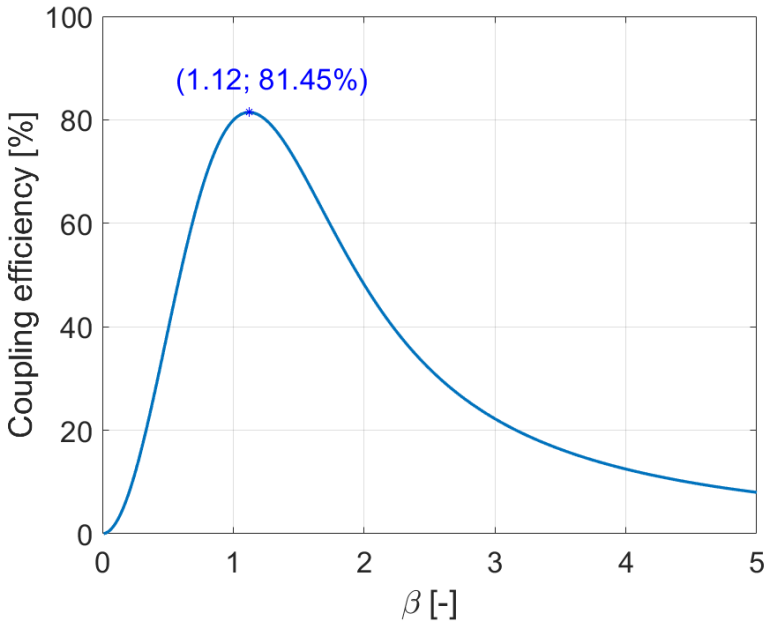

Figure 4.17: Evolution of fibre coupling efficiency in function of the design parameter β.

Considering that the core radius is adapted for the cutoff wavelength, the optimal F-number which maximises the coupling efficiency can be computed :

$$F\#_{design} = \frac{\pi}{2\beta_{max}\lambda_{mid}}\omega_g = 3.6139 \tag{4.16}$$

with $\beta_{max} = 1.1209$ and $\lambda_{mid} = 3$ μm being the design central wavelength. The evolution of the optimal F-number in function of the wavelength is shown on Figure 4.18 while Figure 4.19 displays the evolution of the coupling efficiency with the observing wavelength. For the sake of clarity, the design parameters are reminded in Table 4.8.

Design parameter	Value
NA	0.16
λ_c	2 μm
λ_{mid}	3 μm
a_{core}	4.785 μm
F#	3.6139
ω_g	7.7364 μm

Table 4.8: Design parameters

To conserve a high coupling efficiency, the f-number must increase with the wavelength. For a fixed beam diameter, this translates into a focal length increase. Since it is not feasible to adapt the focal length of a mirror for each wavelength, the central wavelength is the one at which it will be optimised. This translates in a decrease in the coupling efficiency as the wavelength increases. As shown in Figure 4.18 at $\lambda = 2\lambda_c = 4\mu m$ the coupling efficiency has decreased to a value of 72.4% and at $\lambda = 5\mu m$ it drops even further to $\rho = 32\%$. However, for the range of wavelength comprised between 2 and 3.5 μm it is relatively constant around 81.45%. This result is nevertheless only valid for an ideal diffraction-limited system, but as it will be discussed utterly in this report, aberrations are often present and can strongly deteriorate the performance.

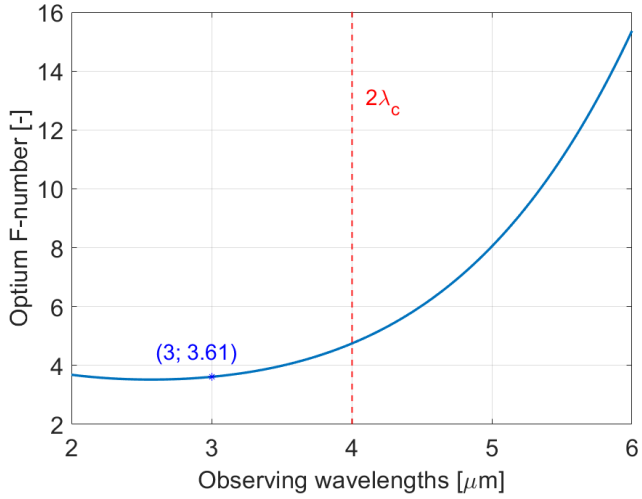

Figure 4.18: Evolution of optimum F-number for best coupling efficiency for different wavelength values. The cutoff wavelength $\lambda_c = 2\mu$m.

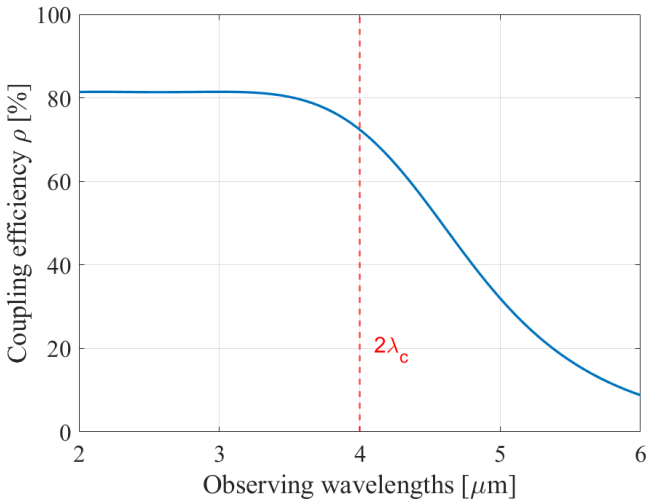

Figure 4.19: Evolution of fibre coupling efficiency with wavelength considering fixed F-number, a_{core}, NA and λ_c given in Table 4.8.

4.10 Light beam focalisation

Once the two beams of the interferometer have been correctly cleared from optical path variation, main wavefront deformations and that a correct recombination and achromatic π-phase have been applied, its width must then be reduced in order to fit into a fibre. An optical reflecting surface consisting of an off-axis parabola has been considered here to perform this task. The choice of a parabolic mirror is supported by the fact that the incoming rays, although they have been oriented correctly by the tip-tilt mirror, still experience some shift transverse to their propagation direction. Parabolic surfaces have the ability to focus every incident ray parallel to the parent mirror axis of symmetry to one single focal point as illustrated by the sketch of Figure 4.20.

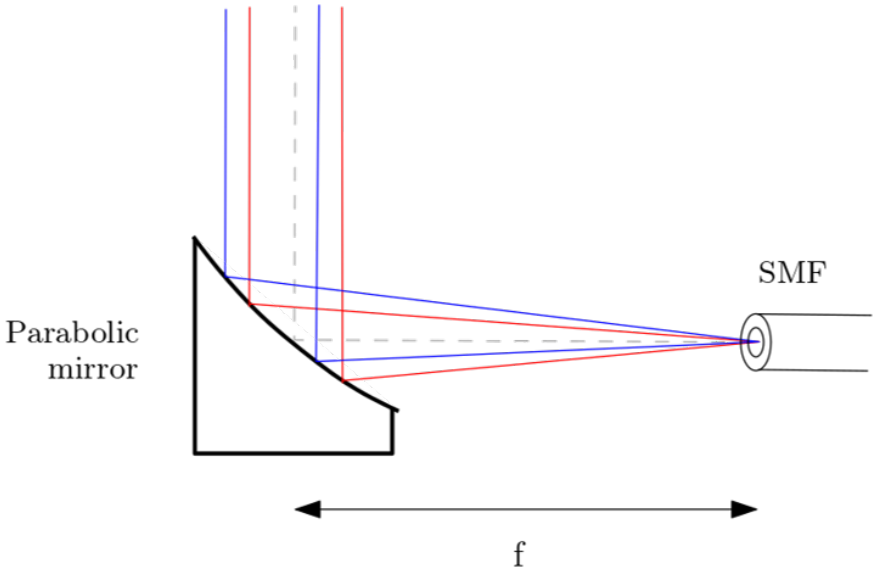

Figure 4.20: Illustration of the off-axis parabolic mirror focusing into a fibre. The red rays correspond to nominal illumination while the blue ones are slightly shifted as a result of the tip-tilt mirror correction applied on deviated beams.

Rays displaced by a telescope pointing errors will focus at the same point on the fibre. The position of the focus is therefore constant regardless of the initial pointing error. The design of this parabolic off-axis mirror is however dependent on the characteristics of the fibre it focuses on. The shape of the wavefront incident on the fibre must indeed correspond as closely as possible to the structure of the fundamental mode propagated by the fibre in order to maximise the coupling efficiency. This wavefront shape is notably impacted by the focal ratio. As obtained in previous Section, for a fibre with $NA = 0.16$ the optimum f-number is 3.6139. Considering an incoming beam with a 2 mm radius, the focal length is, therefore, $f = 14.4556$ mm.

Chapter 5

System Performance

The analysis of the optical system performance has been performed thanks to the implementation of the optical design into the ray-tracing software CodeV. This software allows to check the optical performance of the telescope and to optimise its initial design if necessary so that it is limited by diffraction (or the closest as possible to this limit). It is important to specify here that only one arm of the interferometer has been studied. The other arm is assumed to be symmetrical and therefore to have identical optical performance. This means that the beam combiner, the achromatic phase shift of π or the separation of different wavelengths on a spectrograph are not studied in this work. For more information on the process of implementing an achromatic π phase shift using optical waveguides and on the design of a spectrometer for wavelengths ranging from 3.5 to 4 μm I invite the reader to respectively consult the work of Casimir Fayt [72] and Armand Dubuc [73]. Moreover, in the framework of the telescope implemented in CodeV, optical surfaces such as wavefront sensors, deformable mirrors, delay line and beam splitters are assumed to have no impact on the beam propagation and are therefore also neglected for the performance calculation. The software has thus made possible the computation of several figures of merit depicting its sensitivity to pointing errors, optical path difference, and focalisation properties. The complete optical structure of the telescope described in the previous chapter and implemented in CodeV is represented in Figure 5.1 along with the system of axes used for calculations.

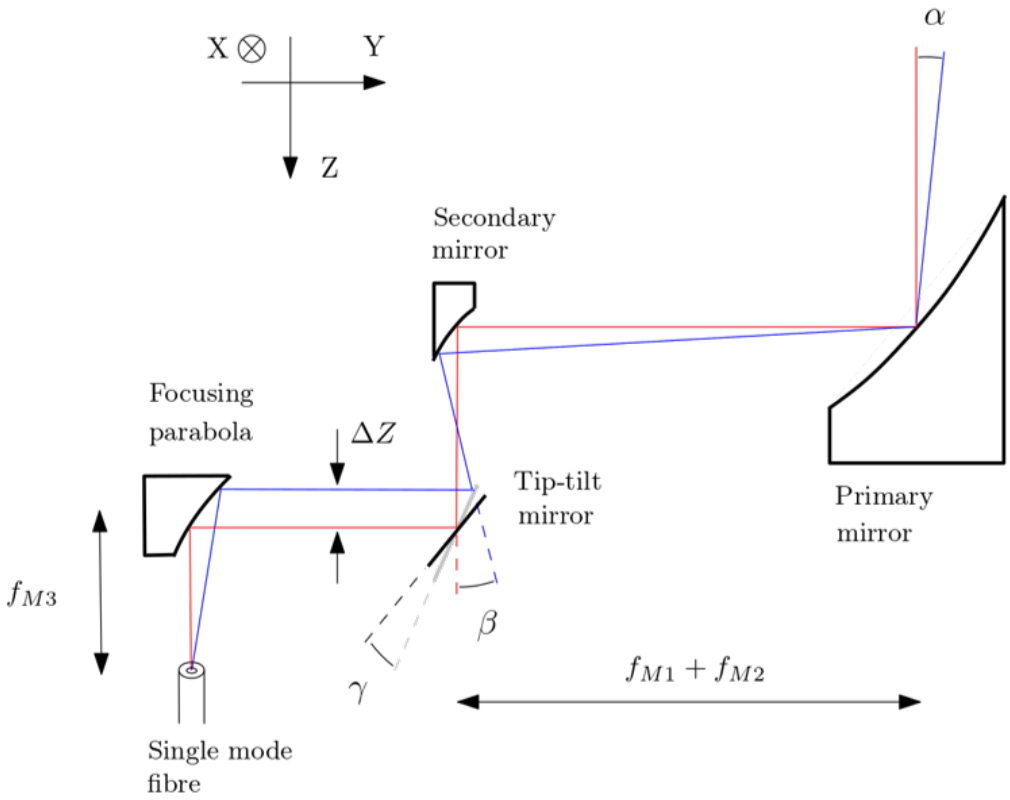

Figure 5.1: Representation of the overall interferometer arm structure implemented in CodeV. The system of axes used for the calculation is represented in the top left part of the scheme. The illustration comprises only the chief ray (centre of the light beam) for the nominal pointing situation (red ray) and a pointing error α (blue ray).

The angle "α" represents the pointing direction (in blue) of the telescope relative to the optimal line of sight (shown in red) which is defined by the position of the star in the observed system. Once photons enter the telescope with such angle α they will be reflected by the secondary mirror with an angle "β" compared to the ideal situation (red ray). It may be useful to point out that the blue and red beams illustrated here represent different pointing situations and therefore do not correspond to simultaneous illuminations but rather to distinct exposures. The tip-tilt mirror, therefore, adapts to every different situation and redirects the incident beam constantly in the same direction. To do this, it has to rotate by an angle "γ" proportional to the previous β deviation. I also specify that the drawing here is in 2D to facilitate the reader's understanding but the system used is actually in 3D. Propagation errors, therefore, occur in and out of the Y-Z plane shown on the drawing. Each of the angles defined above can thus be split based on this system of axes in an X and Y component. The tip-tilt corrections also generate a beam shift ΔZ (and/or ΔX). Finally, the beams are reflected on a last off-axis parabola of focal length $f_3 = 14.46$ mm which focuses the light in a fibre.

The formalism used by CodeV is shown in Figure 5.2. The Y-Z axes form a plane parallel to the baseline of the interferometer. The X-axis is perpendicular to this plane (following a right-hand convention) as shown in the figure. The incidence angles α, associated with misalignments of the telescope (meaning the observed star is no longer centred on the pupil), are separated

into an α_x and α_y angle. The first angle is defined positively for a left-handed rotation around the reference +X axis. The second one is considered positive for a right-handed rotation around the +Y axis (or left-handed around -Y). The beta and gamma angles are defined according to the same convention.

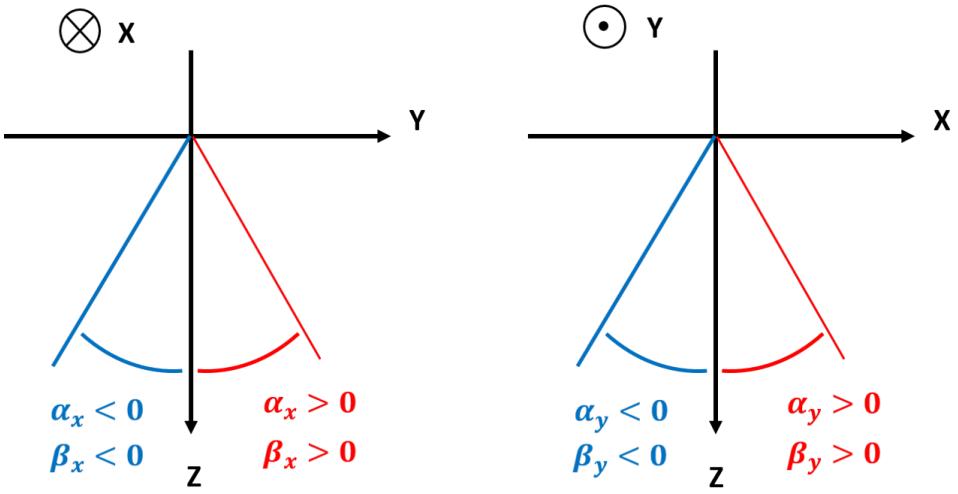

Figure 5.2: Representation of incidence angle α (assimilated to pointing errors) and reduced collimated beam angle after reduction β in function of CodeV formalism. Rays are coming from $-Z$ and the primary mirror is in the $+Z$ direction.

5.1 CodeV primary result

The first parameter to be checked once the complete system has been specified is its ability to focus the light on a fibre with a core diameter of less than 10 μm. CodeV has a "Spot diagram" function that allows visualising the spot-size at the focus of the beam under the paraxial approximation (geometrical optics). It also gives the shape of the Airy disk (resulting from the diffraction phenomenon). For the system to be diffraction-limited, the geometrical aberrations must be included in the Airy disk. Figure 5.3 shows three spots for rays with different angles of incidence. The first one corresponds to the optimal alignment and we see that the rays land on a single point at the centre of the fibre core (represented by the small grey circle). The large circle represents the Airy disk which has a radius $R_{Airy} \simeq 12.5$ μm. The spot sizes are given using two notations, the RMS value which corresponds to the spot root mean square diameter centred on the beam centroid, and the 100% value which gives the minimum circle enclosing all the geometrical rays. One further notices that the system uses only reflecting surfaces therefore there is no path variation between the different wavelengths.

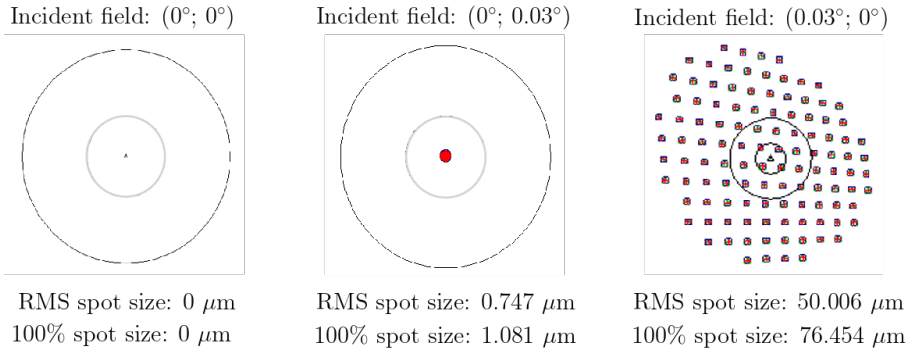

Figure 5.3: System spot size for different incident angles with the use of strictly parabolic mirrors. The small grey circle corresponds to the fibre core radius while the larger one is the shape of the Airy disk. The range of wavelengths considered is [2-4] μm

The second spot corresponding to a positive field (or pointing error) angle in the $-$Y direction (α_x) also shows good light focusing properties. On the other hand, for a positive α_y angle (left-handed around the +X axis of the reference frame), the dimension of the spot is way too large. It is not focused on the fibre core and therefore a large part of the signal will be lost. This poor focusing is due to astigmatism inherent in parabolic mirrors and is difficult to get rid of. Since such geometrical aberrations are not acceptable, it is necessary to move to aspherical surfaces to improve the optical performance. Thus, by using CodeV to optimise the shapes of the primary, secondary and focusing mirror in the fibre, we obtain the spots of Figure 5.4. Now all fields are correctly focused and the spot size variation in function of pointing errors is depicted in Figure 5.5.

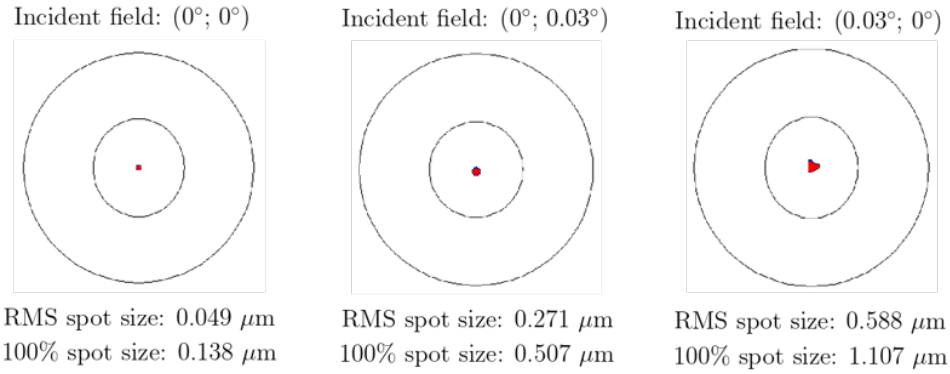

Figure 5.4: System spot size for different incident angles with the use of aspherical mirrors. The small grey circle corresponds to the fibre core radius while the larger one is the shape of the Airy disk. The range of wavelength considered is [2-4] μm

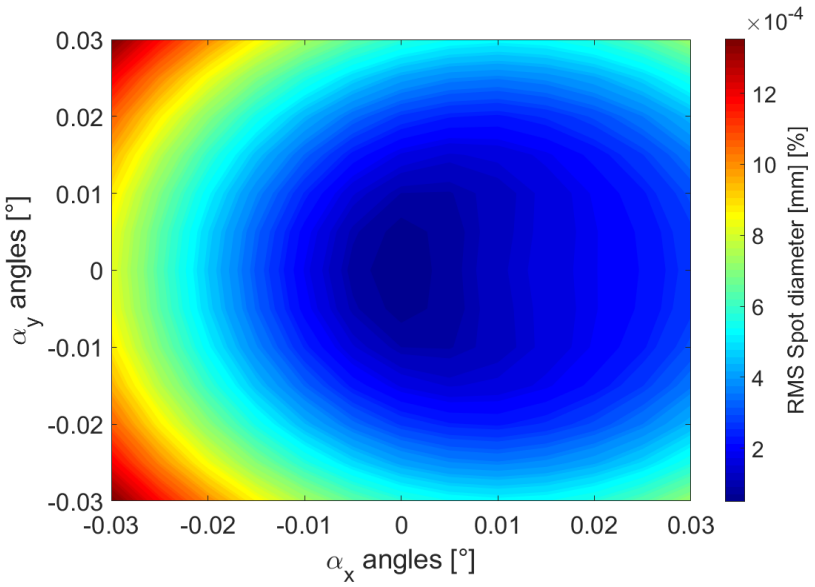

Figure 5.5: Evolution of the RMS geometrical spot size in function of the telescope departure from nominal pointing in X and Y direction. The variation is symmetrical for α_y pointing errors. The maximum spot size is 1.37 μm and corresponds to an off-axis illumination of $(\alpha_x, \alpha_y) = (-0.03; \pm 0.03)$.

5.1.1 Beam width variation

The initial design of the telescope was made to achieve a reduced beam size of 4 mm diameter using off-axis parabolic mirrors. However, the asphérisation of the surfaces impacts the beam dimensions. Moreover, the beam is not exactly radially symmetrical. In fact, for central illumination, CodeV allows the extraction of the focal ratio of the beam in the X-Z and Y-Z planes being $F_{XZ} = 3.4514$ and $F_{YZ} = 3.2084$. The apparent focal length being $f = 14.459$ mm, we can obtain the beam width in the X and Y direction

$$D_X = f/F_{XZ} = 4.189 \text{ mm},$$
$$D_Y = f/F_{YZ} = 4.506 \text{ mm}.$$

These two values are different and therefore imply that the beam is not circular but rather with an oval or elliptical shape. However, since we are using fibre coupling formulas based on the assumption of a radially symmetric Gaussian profile (see Sec.4.9.2), we will approximate the beam shape by a circular contour whose diameter will be the mean between both values. We thus obtain a beam with diameter $D_{new} = 4.3478$mm and an associated f-number $F_{new} = 3.325$.

This new f-number no longer corresponds to the one for which the fibre was optimised. The latter had a maximum coupling efficiency for $F_{old} = 3.614$. A faster focusing will therefore deteriorate the energy transmitted in the fibre (since we have a departure from the optimal wavefront shape). To deal with this problem of coupling reduction there are two possible solutions. Either adapt the fibre to maximise its coupling at the new focal ratio F_{new} or optimise the mirrors' surface with a constraint on the f-number such that it remains at its old value. The first solution has been chosen here in order to avoid an additional complexification of mirrors curvature, but the second option could also have been investigated. Thus, adapting the fibre for a focal ratio of 3.285 can be done by adapting the fibre numerical aperture such that

$$F_{num} = \frac{V_c \lambda_c}{4NA\beta_{max}\lambda_{mid}} \left(0.65 + \frac{1.619}{V_{mid}^{3/2}} + \frac{2.879}{V_{mid}^{6}}\right), \tag{5.2}$$

where $V_{mid} = \frac{V_c \lambda_c}{\lambda_{mid}}$ is a constant. The only variable in the equation is thus the numerical aperture. For the value of $F_{new} = 3.325$ we obtain the numerical aperture that maximises the coupling efficiency, $NA = 0.1737$ which is slightly greater than the old value. The design parameters initially presented in Table 4.8 are now adapted on Table 5.1 for the newly optimised fibre.

Design parameter	Value
NA	0.1737
λ_c	2 μm
λ_{mid}	3 μm
a_{core}	4.407 μm
F#	3.285
ω_g	7.1262 μm

Table 5.1: Design parameters adapted.

5.2 Tip-tilt mirror design

Considering a range of pointing errors of the satellite of ± 0.03 degrees (based on the typical PROBA-type satellites accuracy discussed in Section 4.4) in every direction with respect to the line of sight, this section aims at defining the impacts of such inaccurate pointing over the light propagation direction in the optical system. More precisely, the objective is to find a relation between the angle of incidence of the beam at the aperture of the system (α) and the involved deviation angle from nominal propagation after the beam has been reduced (β). These deviations will give the range of angles over which the tip-tilt mirror must operate.

The calculations were carried out based on the ray passing through the middle of the aperture stop, also known as the chief ray. Since the beam is assumed collimated after reflection on the secondary mirror, every ray across the pupil is therefore reflected in the same direction with a given angle β. The analysis was therefore made using variations in the angle of incidence of the chief ray to determine the evolution of the angles at the exit of the beam reducer using the CodeV formalism previously presented.

Figures 5.6a and 5.6b illustrate the impact of a pointing error around the X and Y axis, respectively on reflected angle β_y in the X-Z plane and β_x in the Y-Z plane after the secondary mirror. It can be seen that a pointing error α_x in the plane of the interferometer (Y-Z plane) generates a change in the beam propagation direction in the Y-Z plane (β_x) as well but not in the X-Z plane (β_y). On the other hand, varying the angle of incidence of the chief ray around the Y-axis (α_y) creates a deflection β_y of the reduced beam in the same X-Z plane but also a slight deflection β_x in the Y-Z plane. Thus, one can see that there is a small coupling between the angles α_y and β_x (which is highlighted in Figure A.1 of the Appendices) but not for the angles α_x and β_y.

Such a relationship is a direct result of the design of the mirrors. The primary and secondary mirrors are indeed off-axis parabolic surfaces. They both have an axis of symmetry which is

Z. They are 2D parabolas (in the Y-Z plane) transformed into 3D paraboloids by a revolution around this Z-axis. Their curvature in the X-Y plane is therefore circular (which is one of the main causes of astigmatism). The surface being off-axis only in the +Y direction means that it also has axial symmetry around this Y-axis. The combination of the 2 parabolas is confocal, so that this symmetry is preserved for both mirrors. Rays directed perpendicularly to the X-axis will therefore always "see" this symmetry, whereas rays with an angle in the X-Z plane will no longer perceive this symmetry. Thus, rays contained in a plane parallel to the Y-axis will always focus on the Z-axis (due to the symmetry) whereas rays in a plane parallel to the X-Z axes will focus on a point slightly shifted from the main optical axis in Z and X. This very small displacement is at the origin of the β_x and β_y output components of the α_y input angles.

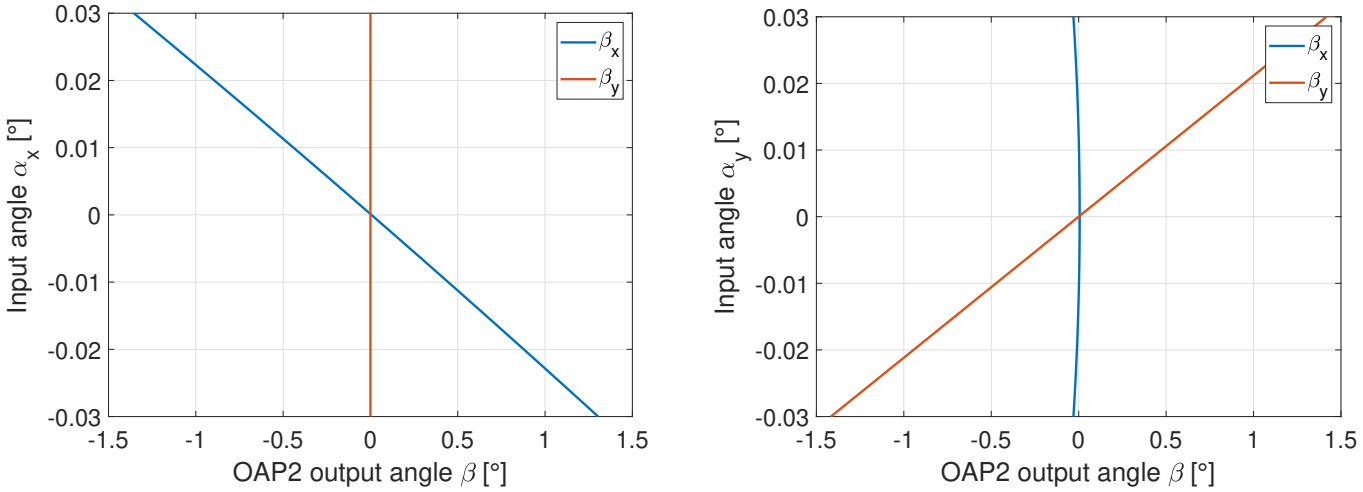

(a) Pointing errors α_x only produce deviation of the reflected beam (after reduction) in the Y-Z plane (around X axis) as illustrated by the blue curve β_y. The red curve represents the angle β_x (in the Y-Z plane of reference, see Figure 5.1) which equals zero for all α_x.

(b) Pointing errors α_y produce deviation of the reflected beam (after reduction) in the Y-Z plane (β_x, in blue) and in the X-Z plane (β_y, in red). Nevertheless, the angle β_x remains very small.

Figure 5.6: Relation between the incidence angles at the telescope aperture and the reduced beam propagation direction (in terms of deviation angle β).

These relationships linking the input and output angles can be represented by the following equations obtained using a curve fitting with second-order polynomials

$$\beta_x(\alpha_x, \alpha_y) = -32.37 \cdot \alpha_x^2 - 44.39 \cdot \alpha_x - 37.64 \cdot \alpha_y^2, \tag{5.3}$$

$$\beta_y(\alpha_y) = 47.23 \cdot \alpha_y. \tag{5.4}$$

with a root mean square error $e_{rms}^{\beta_x} = 0.0034°$ and $e_{rms}^{\beta_y} = 0.0023°$ meaning the angle β is known thanks to those equations with a precision smaller $1/100$ of a degree. These expressions also show that β_x angle scale with the square of α and has an opposite sign (considering left-handed angles as positive) while β_y angle scales with α_y. Giving that the pointing errors are comprised between $-0.03°$ and $0.03°$ in every directions the resulting β deviations for the complete range of angles α are illustrated on Figures 5.7a and 5.7b where the largest deviation $\beta_x = -1.392°$ occurs for an incident field angle of $(\alpha_x;\alpha_y) = (0.03°; \pm 0.03°)$ and $\beta_y = \pm 1.419°$ for $(\alpha_x;\alpha_y) = (0.03; \pm 0.03°)$.

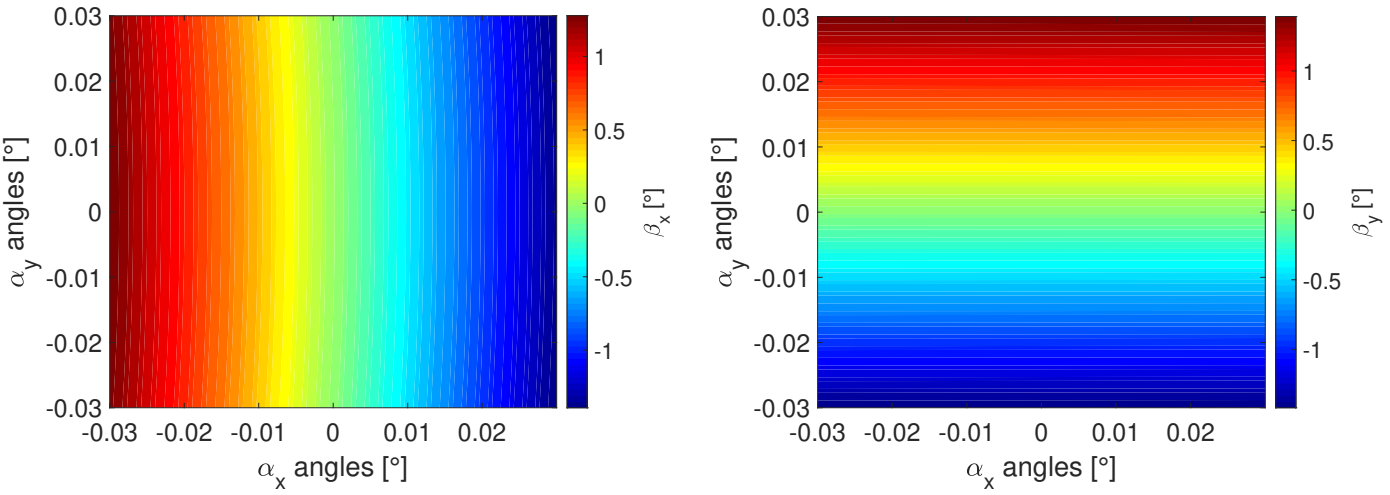

(a) Secondary mirror output beam angle (β_x) for various pointing errors.

(b) Secondary mirror output beam angle (β_y) for various pointing errors.

Figure 5.7: Secondary mirror output angle deviation from nominal path (0°,0°) for various combinations of pointing errors around X and Y axes (α_x and α_y).

5.2.1 Tip-tilt mirror choice

The tip-tilt mirror must therefore be able to correct deviations from the nominal optical path of 1.392° around X-axis and 1.419° around Y-axis. The tip-tilt mirror is positioned in such a way that it reflects the light (when the nominal configuration is considered) at 90° meaning that the angle of incidence of the beam onto the mirror surface is 45° in the ideal situation. The correction process carried out by the tip-tilt mirror is illustrated in Figure 5.8 from CodeV, which clearly demonstrates the impact it has on the direction of propagation of the beams.

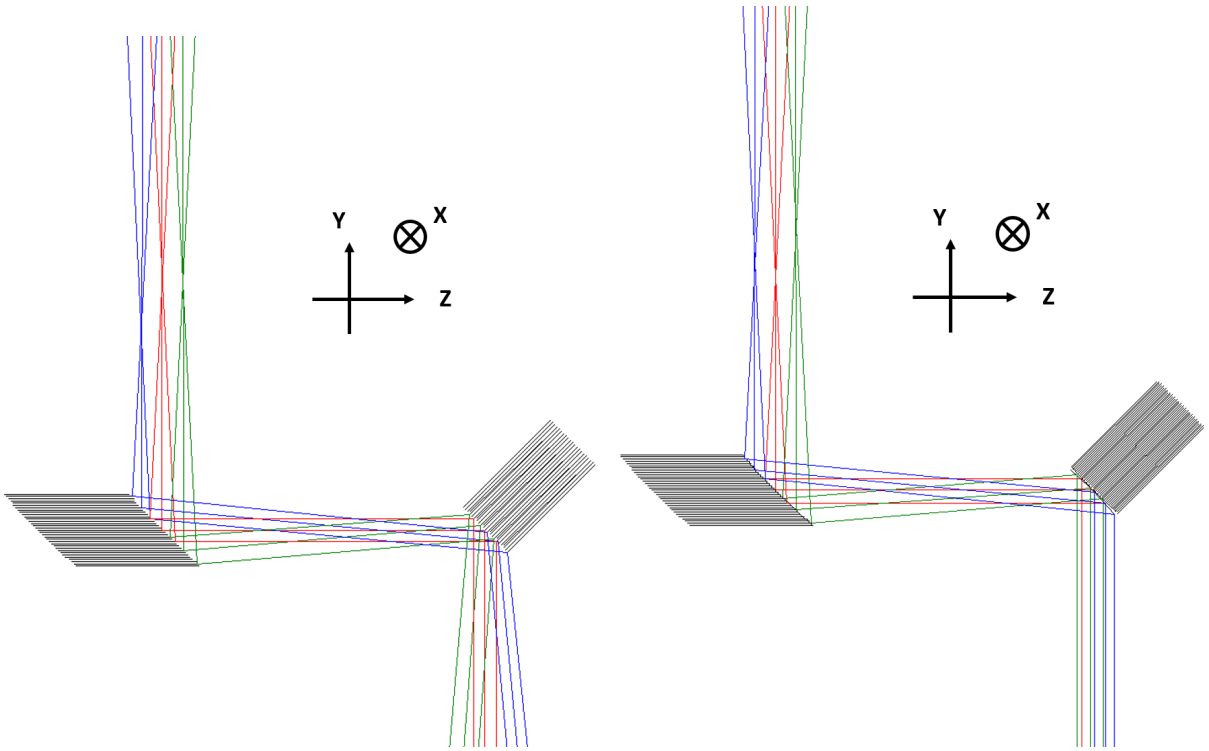

(a) Rays propagation without tip-tilt mirror correction.

(b) Rays propagation with corrections made by the tip-tilt mirror.

Figure 5.8: Role of the tip-tilt mirror in redirecting the light beam. Rays propagate downward. The red ray corresponds to nominal pointing. The blue and green rays are for pointing error $\alpha_x = +0.1°$ and $\alpha_x = -0.1°$ respectively for illustration.

The corrections made by the tip-tilt mirror are of prime necessity in order to keep the same direction of propagation in every situation (for the considered pointing errors). By simple geometry, one can obtain that for incident angles on the tip-tilt mirror varying by $(\beta_x, \beta_y) = (\pm 1.392°, \pm 1.419°)$ the range of angular variation that must be achieved by the tip-tilt mirror is $(\gamma_x, \gamma_y) = (\beta_x/2, \beta_y/2) = (\pm 0.696°, \pm 0.7095°)$. Therefore the ideal steering mirror should have a diameter around 8 mm and be able to rotate ±12.1 milliradians around the reference X-axis and ±12.4 milliradians around the reference Y-axis. Two examples of possible mirrors proposed by "The PI Group" are presented in Table 5.2.

Mirror reference	S-335.2SHM1	S-334
Maximum tip/tilt angle	± 17.5 mrad	120 mrad
Tip/tilt resolution	0.1 μrad (open loop)	0.2 μrad
Mirror diameter	12.5 mm	$\leq$ 12.5 mm

Table 5.2: Examples of suitable tip-tilt mirrors for correction of the optical path deviations computed. [74]

5.3 Optical path length variation

Pointing errors necessarily imply a difference in the optical length travelled by the rays. In addition, the corrections made by the tip-tilt mirror also affects the optical path. Therefore this

section aims at identifying the magnitude of the optical path length variation when misalignments of the telescope occur. The software CodeV allows to extract the intersection points of different rays on the optical surface and thus to determine the path length of these rays through the complete system.

We first focus on the optical path length (OPL) variations of the chief ray (which is the ray passing by the centre of the aperture stop). The OPL for central illumination is 2261.9 mm and the departure from this distance in function of pointing error is shown in Figure 5.9.

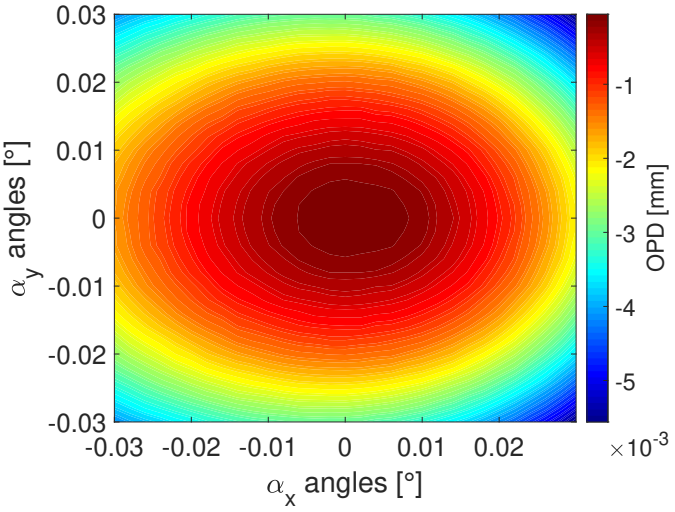

Figure 5.9: Chief ray optical path difference in function of telescope pointing error with respect to nominal situation where OPL = 2261.9 mm.

It can be noticed that all values are negatives which correspond to a shorter path length. Therefore, as soon as misalignments occur, the optical path length of the central beam is reduced. The most important variation is -5.1 μm and takes place for angles $(\alpha_x; \alpha_y) = (0.03°; \pm 0.03°)$. Since we want to keep a constant path length for both interferometer arms, we need a delay line capable of working on this deviation in length and correcting it accurately enough so that it can be removed (typically an accuracy of $\lambda/100$ is required). The path length also appears to be more sensitive to positive (than negative) axial angles.

For good recombination of the beams of each arm, it must be guaranteed that they arrive at the same time from the beam combiner. However, it is also necessary to ensure that the wavefront structure is identical for both arms, in order to ensure the correct superposition of the light beams of the two telescopes. A relative deformation of the wavefront between the two arms during recombination causes a loss of temporal coherence. The wavefront corresponding to a light emission source at time "t" will interfere with a light front produced at a different time. The superimposed images are no longer coherent because they belong to different times and are therefore in reality two different images.

In order to avoid this, the symmetry of the wavefronts between the two telescopes must be guaranteed. For this purpose, we study again only one arm and assume that the results obtained can also be assimilated to the second telescope. The variation of the optical paths as a function of the input incidence field angles for rays located at the edge of the entrance pupil is calculated. More precisely, we consider here the meridional rays (entering the pupil edge at the top (+Y)

and the bottom (-Y)) and the sagittal rays (entering the pupil left-edge (+X) and right-edge (-X)). The optical path variations are illustrated on Figure 5.10a and 5.10b for meridional rays and on Figure 5.10c and 5.10d for sagittal rays.

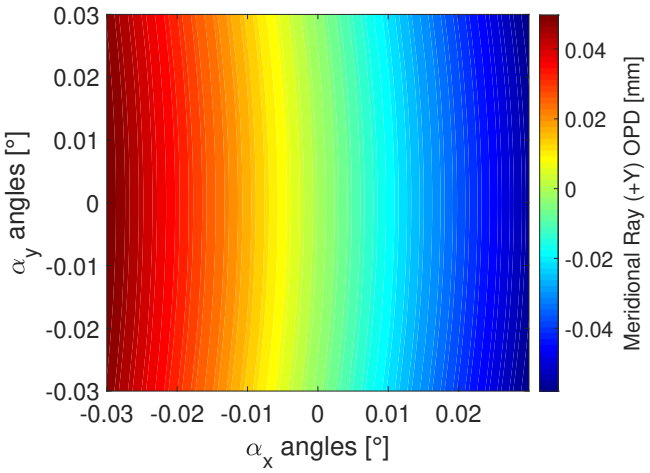

(a) Meridional ray (+Y direction) optical path length variation.

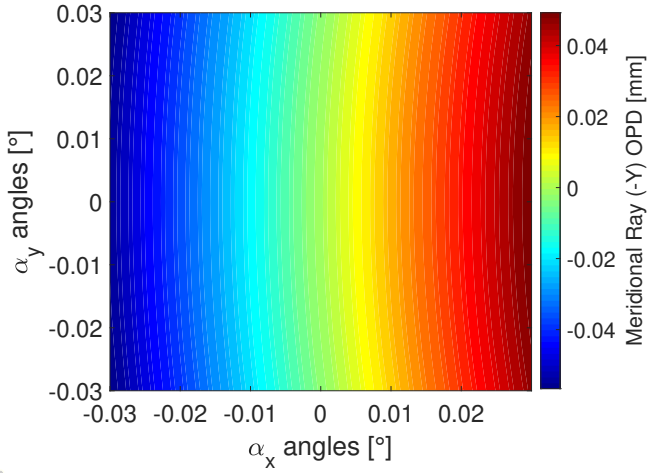

(b) Meridional ray (-Y direction) optical path length variation.

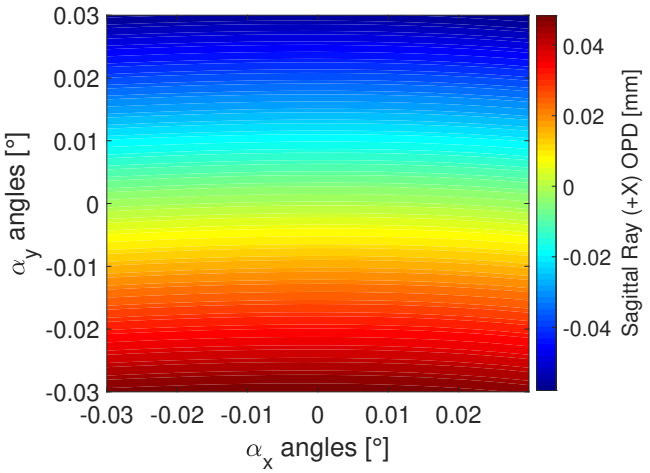

(c) Sagittal ray (+X direction) optical path length variation.

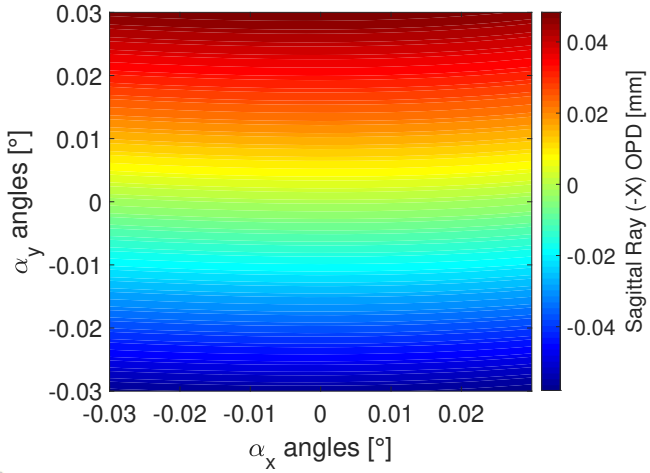

(d) Sagittal ray (-X direction) optical path length variation.

Figure 5.10: Representation of the variation of the optical path length difference for rays entering the pupil at different positions in function of the telescope pointing errors. The central illumination does not generate any optical path length difference between the four different rays.

The OPL difference between the chief ray and other rays across the pupil is not a big issue if this difference is kept the same for both telescopes across their own pupil plane. What really matters is the optical path length variations induced by the pointing errors. These pointing errors affect differently separate rays across the pupil. If the OPL of one ray from the first telescope is not the same as the OPL of its counterpart ray in the second telescope, then we have incoherent recombination. Therefore, we want to keep track of this optical path differences between the two telescopes and get rid of them. Since the structure of the satellite is assumed symmetrical, this problem simplifies to correctly suppressing the OPL variations of a specific ray in function of pointing errors for both arms individually. The range of OPL variations for

the four rays previously considered (two meridional and two sagittal rays) are summarised in Table 5.3.

Ray	Nominal path length	Maximum increase/ decrease	Corresponding pointing error (α_x, α_y)
Chief	2261.9635 mm	$\sim$ / -5.56 μm	$\sim$ / (0.03;$\pm$0.03)
Meridional (+Y)	2262.9635 mm	50.79 μm / -57.99 μm	(-0.03;0) / (0.03;$\pm$0.03)
Meridional (-Y)	2262.9635 mm	50.3 μm / -55.62 μm	(0.03;0) / (-0.03;$\pm$0.03)
Sagittal (+X)	2262.9635 mm	49.37 μm / -57.9 μm	(-0.002;-0.03) / (0.03;0.03)
Sagittal (-X)	2262.9635 mm	49.37 μm / -57.9 μm	(-0.002;0.03) / (0.03;-0.03)

Table 5.3: Identification of the maximum optical path length deviation for 4 different rays (sagittal and meridional) and the related telescope pointing error. The nominal path length corresponds to perfect satellite pointing.

Since these variations of OPL are not constant across the pupil, a deformable mirror is required to compensate them. The greatest variation being of 57.99 μm it must have a stroke of 29 μm to compensate it. This value is larger than the usual 15 μm achievable by common deformable mirrors.

5.3.1 Delay Line choice

The optical path length variation computed in the previous section must be corrected to guarantee a clean detection. This is the job of the delay line. Considering the chief ray OPL change of 5.56 μm it must be able to generate a maximum time delay of $18.533 \cdot 10^{-15}$ sec (18.533 fs) with nanometer accuracy. An example of existing product characteristics, provided by MKS Newport [75], are summarised in Table 5.4

Delay line reference	DL125	S-334
Maximum travel range	125 mm (416 ps)	99 mm (330 ps)
Minimum incremental motion	75 nm	300 nm
Weight	2.8 kg	

Table 5.4: Example of possible optical delay line choice for precise interferometric measurements.

5.4 Beam transverse deviation/shift

As described previously, the tip-tilt mirror corrects the beam propagation such that whatever the initial pointing errors (in the range $\pm 0.03°$), the beam after reflection on the tip-tilt mirror will always exhibit the same propagation direction. However, such correction comes at the expense of another type of error: the shift of the beam perpendicularly to its propagation direction. These transverse shifts are directly related to the tip-tilt variations performed by the mirror and are identifiable in Figure 4.8. The quantification of this displacement can be done geometrically and its evolution in function of angles α_x and α_y is shown in Figure 5.11 for X and Z-oriented shifts respectively.

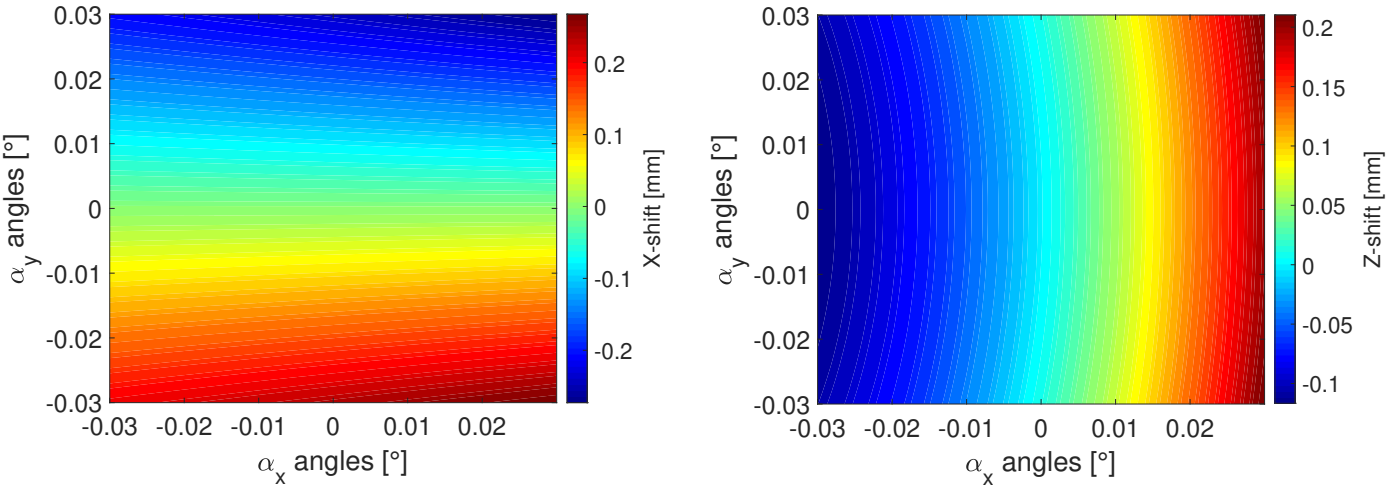

(a) Centroid displacement in X direction (ΔX) in mm.

(b) Centroid displacement in Z direction (ΔZ) in mm.

Figure 5.11: Transverse displacement of the chief ray (or centroid) in function of telescope pointing errors α_x and α_y.

One can see that the α_x angles slightly affect the X-shift and strongly impact the Z-shift while it is the opposite case for α_y angles. The relation between the shifts and the pointing errors can be approximated by a quadratic equations:

$$\Delta X \simeq -7.967\alpha_y - 36.62\alpha_x\alpha_y \qquad \text{with } e_{rms} = 0.2219\ \mu\text{m}, \tag{5.5}$$

$$\Delta Z \simeq 5.258\alpha_x + 45.95\alpha_x^2 + 15\alpha_y^2 \qquad \text{with } e_{rms} = 0.2632\ \mu\text{m}, \tag{5.6}$$

where e_{rms} designates the root mean square error between the reals values of the shifts and the approximated values computed using a polynomial quadratic curve fitting on Matlab. Figure 5.12 shows the range of shifts along X and Z axes in function of pointing errors. The maximum relative deviation from nominal pointing is 0.3465 mm and occurs for incidence angles $(\alpha_x, \alpha_y) = (0.03°; \pm 0.03°)$.

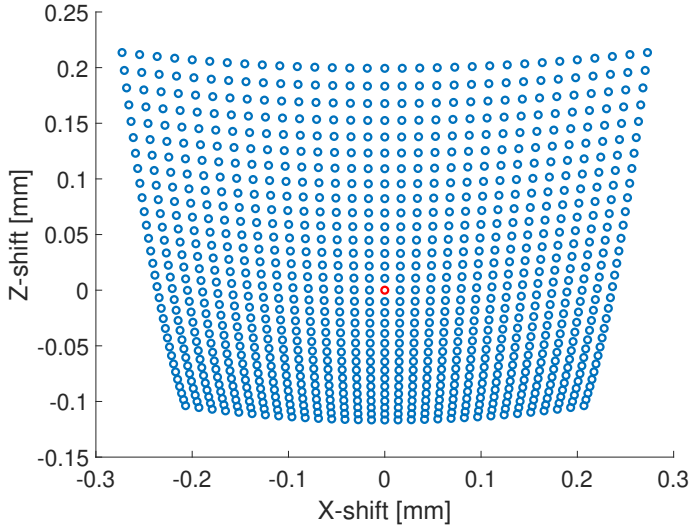

Figure 5.12: Range of collimated beam centroid (chief ray) deviations in X and Z direction after tip-tilt correction for $\pm 0.03°$ incidence angles α_x, α_y. The red circle corresponds to nominal illumination $(\alpha_x, \alpha_y) = (0°; 0°)$

5.4.1 Effect on focalisation and coupling efficiency

The chief ray transverse displacement after tip-tilt correction changes the point at which it will be reflected by the last mirror focusing into the fibre as shown on Figure 4.20 of the previous chapter. Now that we know the magnitude of this displacement in X and Z we can determine the variation in the apparent focal length of a certain incident beam as a function of its X and Z displacements (resulting from α_x and α_y pointing errors). Taking into account an approximate constant beam diameter $D_{new} = 4.4025$ mm (see Sec.5.1.1) we deduce the range of variation of the focal ratio depicted on Figure 5.13.

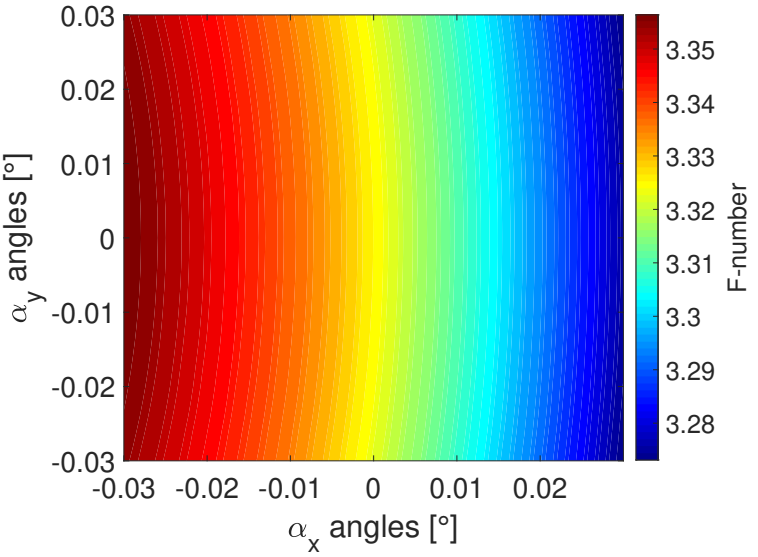

Figure 5.13: Variation of the F-number of the beam being focused on the single-mode fibre in function of the telescope pointing errors α_x, α_y and assuming a constant beam diameter $D_{beam} = 4.4025$ mm.

Since the expression of the coupling efficiency in Equation 4.15 is a function of the focal ratio and the wavelength, its theoretical evolution is shown in Figure 5.14. As the variations of the F-number are between 3.273 and 3.357, it can be guaranteed that the coupling efficiency values obtained will lie within the black rectangle also shown in the figure.

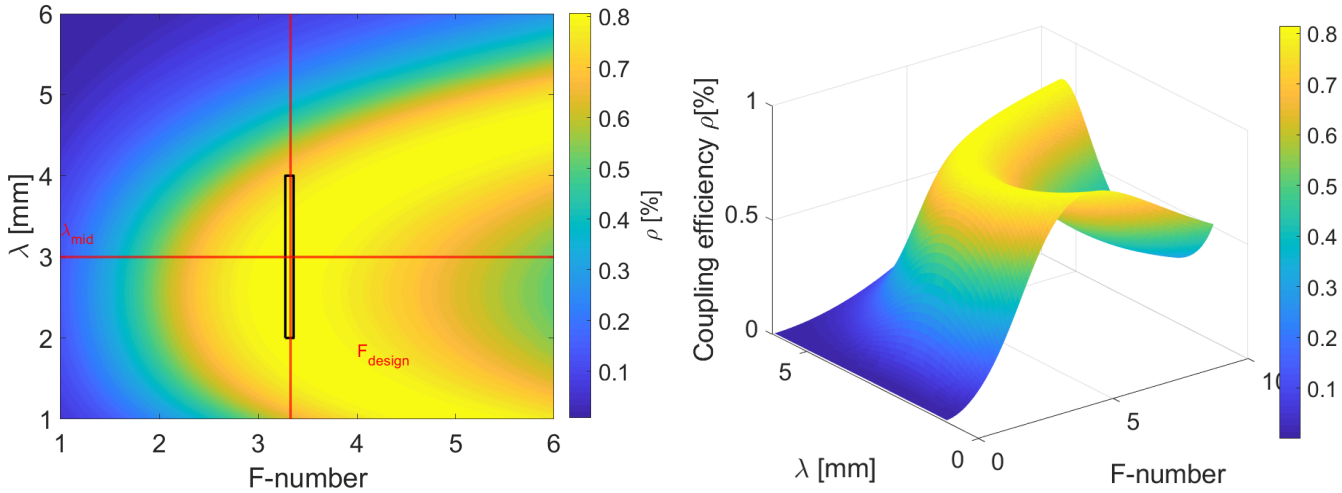

(a) 2D view of coupling efficiency variation in function of λ and F-number.

(b) 3D view of coupling efficiency variation in function of λ and F-number.

Figure 5.14: Dependence of the fibre coupling efficiency on λ and F-number for a core radius $a = 4.784\mu m$ and Numerical aperture $NA = 0.16$.

Inside this rectangle, the value of the coupling efficiency is approximated constant over the F-numbers considered. The most impacting parameter is the wavelength. As a matter of fact, the central wavelength $\lambda = 3$ μm is propagated in the fibre with an 81.45% efficiency

whereas $\lambda_c = 2$ μm and $2\lambda_c = 4$ μm are respectively coupled with an efficiency of 72.5% and 81.4%. Considering now individually the 2, 3 and 4 μm wavelengths, we can express their coupling efficiency as a function of the telescope alignment errors. Figure 5.15 show that the central wavelength is indeed optimised for $F_{design} = 3.325$ and therefore decreases as soon as misalignments occur. For λ_c and $2\lambda_c$ this is not the case. We notice that both wavelengths will be slightly better propagated in the fibre when positive α_x depointing errors occur.

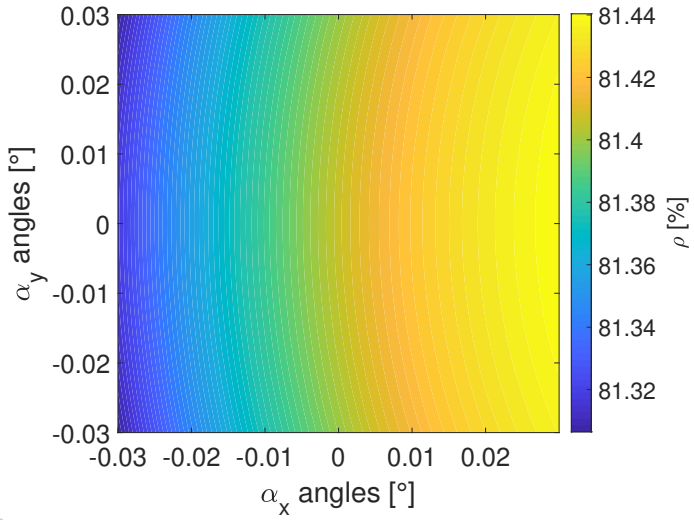

(a) Coupling efficiency in function of pointing errors for $\lambda = \lambda_c = 2\mu$m

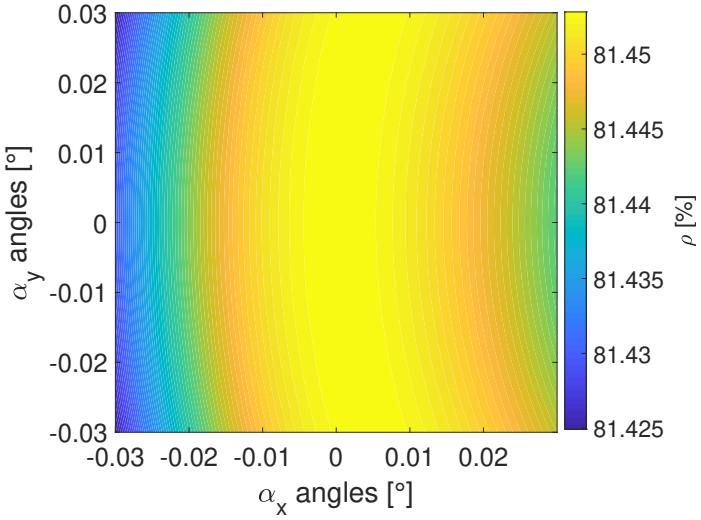

(b) Coupling efficiency in function of pointing errors for $\lambda = 3\mu$m

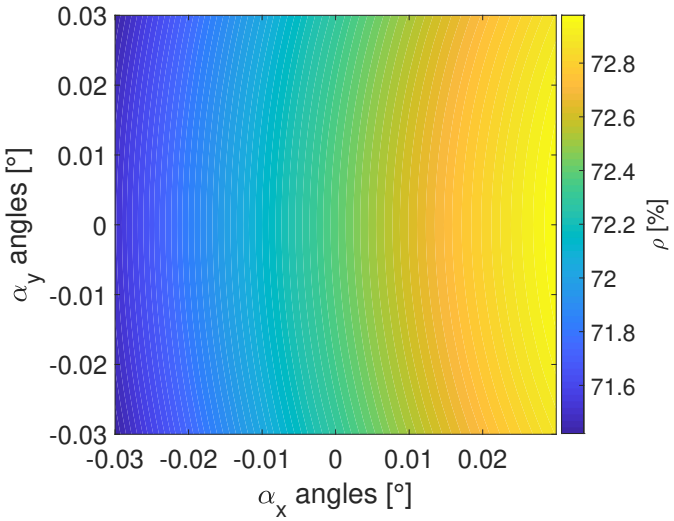

(c) Coupling efficiency in function of pointing errors for $\lambda = 2\lambda_c = 4\mu$m

Figure 5.15: Impact of telescope pointing errors (α_x, α_y) on fibre coupling efficiency (ρ) for different wavelengths.

5.5 Aberrations impact on Extinction

The extinction level of an interferometer has to reach a value near to 10^{-5} to ensure the correct cancellation of the starlight and the retrieval of the planet signal with a sufficiently high signal to noise ratio. The extinction is a quantity sensitive to the incoming wavefront structure, which is affected by the quality of the optical surfaces, their good positioning, heat turbulence, and other factors. Therefore aberrations resulting in distortion of the wavefront will degrade the level of extinction and it is necessary to quantify how much imprecision in the knowledge of the wavefront is acceptable before the loss of the signal of interest. To represent the different types of aberrations that can affect a wavefront the Zernike polynomials are used. The expression of the extinction ratio in function of a given aberration is derived from [30] based on the following definition,

$$\text{Ext} = \frac{E_{residual}}{E_{collected}} \tag{5.7}$$

where the collected energy is the energy per unit surface area (E_S) times the collecting area, which is here made of 2 apertures such that

$$E_{\lambda,collected} = E_{S,\lambda} \cdot 2\pi R_{M1}^2 \tag{5.8}$$

The variable R_{M1} designates the primary mirror aperture radius which is 10 cm. $E_{S,\lambda}$ is the energy per unit surface at one wavelength and is assumed to be equal to one here for convenience. The quantity of residual energy depends on the intensity of the mismatch between the two recombined wavefronts from both arms of the interferometer. The larger the relative distortion between the two, the greater the residual energy and therefore the worse the extinction ratio. This residual energy at one wavelength is mathematically expressed by

$$E_{\lambda,residual} = \int\int |\Psi_{recomb}(r,\theta)|^2 \, r dr d\theta \tag{5.9}$$

where $\Psi_{recomb}(r,\theta)$ represents the complex amplitude of the recombined beams. This recombined complex amplitude can be developed such that the expression becomes

$$E_{\lambda,residual} = RT \int_0^{2\pi} \int_0^{R_{pup}} \left|\Psi_a(r,\theta) + \Psi_b(r,\theta) e^{i\pi}\right|^2 r dr d\theta \tag{5.10}$$

where R and T are the reflection and transmission coefficient of the beam splitters assumed to be used here for a proper recombination process in the pupil plane with adequate π phase shift as presented in Section 2.4 for the AIC and the Mach-Zehnder interferometer. This π phase shift is considered here to be applied on the arm of the interferometer denoted by the subscript "b" and in terms of waves complex amplitudes is written $e^{i\pi}$. The notation $\Psi_a(r,\theta)$ and $\Psi_a(r,\theta)$ represents the signal complex amplitude propagating in arms a and b of the interferometer. Each wave travels along a particular optical path. The two wave fronts are therefore affected by deformations, and thus by a spatial phase distribution $\phi(r,\theta)$

$$\Psi_a(r,\theta) = P(r,\theta) \cdot e^{i\phi_a(r,\theta)}, \tag{5.11}$$

$$\Psi_b(r,\theta) = P(r,\theta) \cdot e^{i\phi_b(r,\theta)}, \tag{5.12}$$

with $P(r,\theta)$ the pupil function equal to 1 inside the pupil and 0 outside. The extinction ratio becomes

$$Ext_\lambda = \frac{RT}{2\pi R_{pup}^2} \int_0^{2\pi} \int_0^{R_{pup}} \left| e^{i\phi_a(r,\theta)} - e^{i\phi_b(r,\theta)} \right|^2 r dr d\theta. \tag{5.13}$$

We consider now an aberration on the wavefront of arm "a" such that it can be expressed in terms of Zernike polynomials

$$\phi_a(r,\theta) = a_i \cdot Z_i(r,\theta) \tag{5.14}$$

where a_i is the weight associated with the Zernike polynomial Z_i in radians. The second wave is considered here free of aberration ($\phi_b = 0$). The evolution of the extinction level in function of the aberration strength of individual effects such as tip-tilt (Z2 and Z3), defocalisation (Z4), astigmatism (Z5 and Z6) and coma (Z7 and Z8) are presented in Figure 5.16.

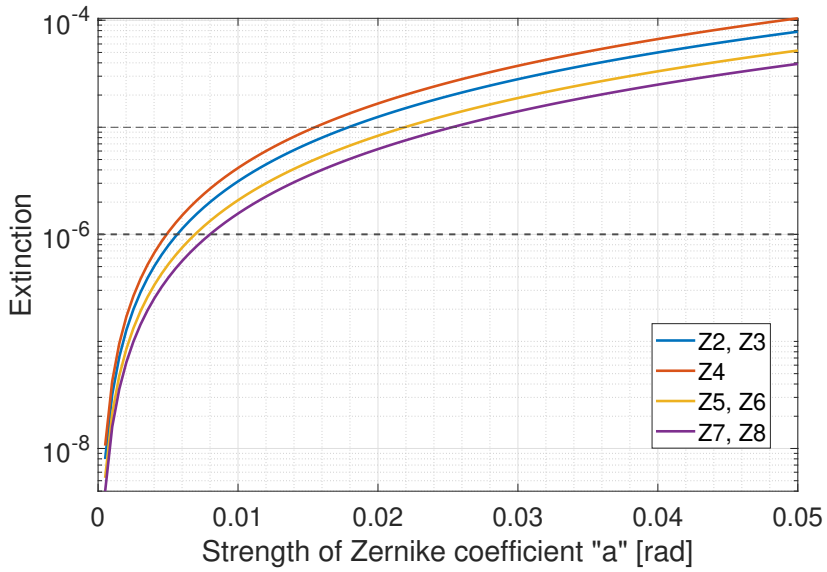

Figure 5.16: Extinction ratio in function of aberration strength for different aberration types described by Zernike polynomials. Here, one arm has been considered aberrated while the other remained free of aberrations.

To correctly discriminate the planet from its star, the energy ratio at the output of the combiner must be 10^{-5} or even 10^{-6}. This implies a maximum authorised value for the wavefront defects listed in Table 5.5 according to the Zernike polynomial considered.

Zernike polynomial	a_i for $Ext = 10^{-6}$ [rad]	a_i for $Ext = 10^{-5}$ [rad]
Z_2, Z_3	0.0056	0.0178
Z_4	0.0044	0.0156
Z_5, Z_6	0.0067	0.0222
Z_7, Z_8	0.0078	0.0256

Table 5.5: Maximum Zernike weight coefficient a_i for different Zernike polynomials (from 2 to 8) in order to have an extinction ratio $Ext \leq 10^{-5}$ and $Ext \leq 10^{-6}$.

When relaxing the requirements from 10^{-6} to 10^{-5} the maximum weight of Zernike polynomials increases on average by 3. The tip-tilt and defocalisation are the aberrations degrading

the most the wavefront for a given aberration strength and according to [30][28] they are also the most present and constraining residual phase defects in interferometric systems in space. One solution is therefore to use modal filtering thanks to the use of single-mode fibres. Considering that we remain in the small aberration domain, which means that we work with a weakly aberrated incoming wavefront, the use of a single-mode waveguide will filter the wavefront and clean it from every aberration. The wavefront exiting the fibre will be free of wavefront defects and have the shape of the fundamental mode propagated by the fibre. In the scope of such small defects, the null depth (or extinction) is described by Equation 2.12 which is represented by the green curve in Figure 5.17.

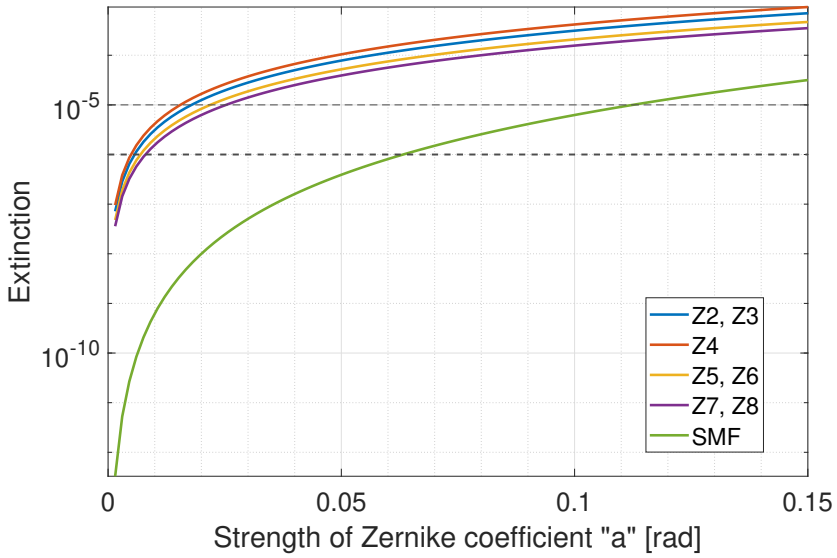

Figure 5.17: Illustration of the effect of modal filtering by a single mode fibre onto the Extinction sensitivity to wavefront defects expressed in terms of Zernike polynomials.

The maximum authorised Zernike weights are now a = 0.06 rad and a = 0.11 rad for an extinction Ext = 10^{-6} and Ext = 10^{-5} respectively. This highlights the interest in using a single-mode fibre to decrease the extinction sensitivity to optical aberrations. Now that we have a maximum aberration strength admissible we can compute the impact of different Zernike polynomials on the coupling efficiency of the system for different wavelengths considering this maximum defect value of 0.11 rad. This is shown on Figure 5.18.

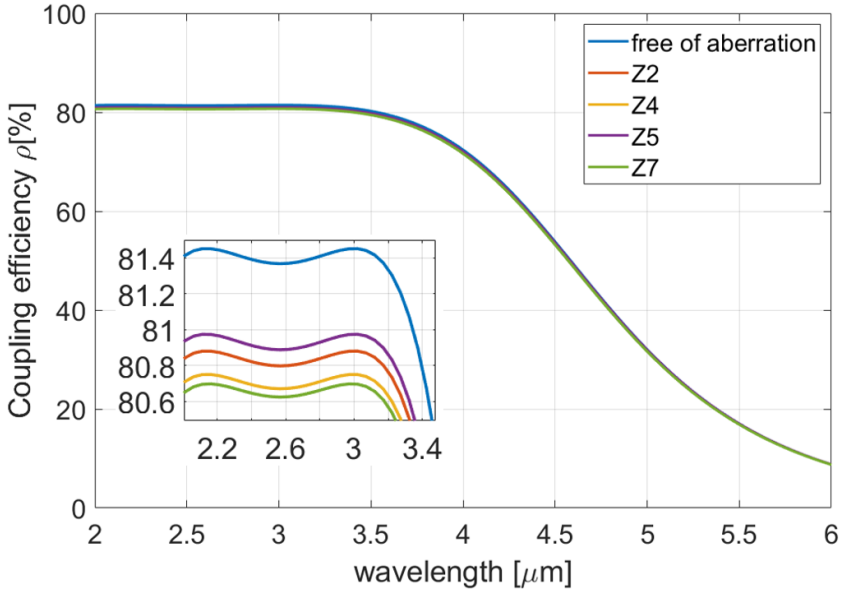

Figure 5.18: Impact of different Zernike polynomials on coupling efficiency in function of wavelength with fixed weight $a_i = 0.11$ rad (corresponds to a null depth $N = 10^{-5}$).

The coupling efficiency of the fibre is much less sensitive to wavefront deformations than the extinction ratio. Each individual effect of the eight first Zernike polynomials generates a decrease in coupling efficiency smaller than 1% which is almost negligible compared to their impact on the extinction ratio. Moreover, the fibre seems, in opposition to the extinction ratio, more sensitive to higher-order Zernike polynomials as coma (Z_7, Z_8) and defocus (Z_4) seem the most damaging deformations.

Additionally, the single-mode fibre permits wavefront cleaning up to a Zernike weight coefficient $a_i = 0.11$ rad for 10^{-5} nulling. Considering the central wavelength of observation $\lambda = 3$ μm, the maximum strength of the Zernike polynomial translates into a maximum relative phase shift between telescopes of $\Delta\phi = 0.11\lambda/(2\pi) = 52.52$ nm. Larger wavefront distortion will create poor levels of extinction and decrease coupling efficiency leading to a weak photon flux. Such greater aberration must therefore be corrected for instance, by the use of a deformable mirror.

5.6 Detectable system

The type of observable system is defined by the angular resolution of the interferometer. Using Equation 2.2 for the central wavelength and a baseline of 4 meters, we obtain $\theta = 375$ mrad $= 77$ mas. This corresponds to the angular separation between the fringes created by the interferometer transmission map (illustrated in Figure 2.4). Therefore, to detect a planet around a star, the angular separation between the two bodies should not be smaller than 77 mas. For instance, we consider the Proxima Centauri system situated at a distance of 4.2441 light-years from Earth with its 2 planets Proxima Centauri b and c. The interferometer is able to place a planet orbiting the star on a constructive interference as soon as its relative distance is greater than 0.1 AU. Therefore, the system is able to detect Proxima Centauri c which is 1.489 AU away from its host star but not Proxima Centauri b which is at a closer distance of 0.0486 AU and therefore never ends up on a constructive part of the transmission map.

Chapter 6

System optimisation

6.1 Tip-tilt mirror position

After reflection on the second mirror, the mispointed beams propagate at an angle β with respect to the optimal direction as discussed in Section 5.2.We have seen that despite a correction of the direction of propagation, an offset perpendicular to the direction of propagation of the beam is generated after reflection. This offset is proportional to the distance the beam travels before reflecting on the tip-tilt as shown on Figure 6.1.

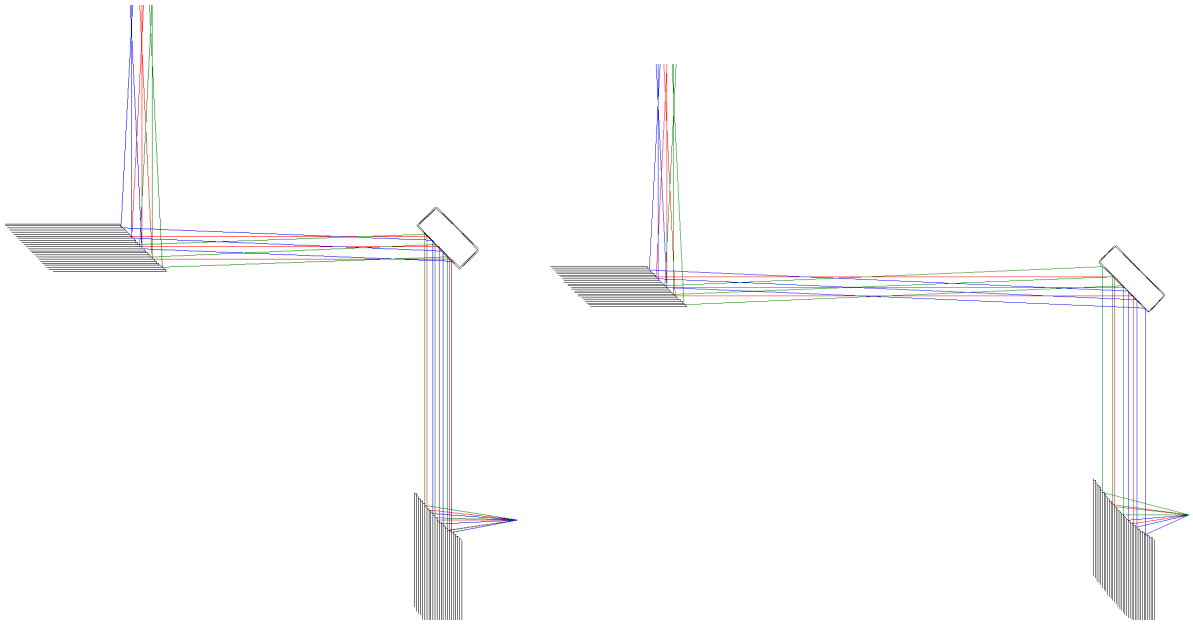

(a) Distance between secondary and tip-tilt is set to 5 cm.

(b) Distance between secondary and tip-tilt is set to 10 cm.

Figure 6.1: Effect of distance between secondary mirror and tip-tilt mirror on the beam propagation offset.Red rays corresponds to ideal situation. Green and blue are for pointing errors $\alpha_y = -0.03°$ and $\alpha_y = +0.03°$ respectively. (Rays propagate downward)

This offset implies that the rays from an initial depointing error will meet the last mirror (which focuses in the fibre) at different point of its surface. Such rays displacement across the mirror surface implies a variation of distance to the focal point. In other words, this beam offset modifies the apparent focal length of the last optical surface and therefore reduces the final cou-

pling efficiency as presented in Section 5.4.1. Moreover, in Figure 6.1b, the angle of incidence of the beam on the fibre varies over a larger range, which can be defined by a cone with a larger base. However, the fibre can only correctly couple rays within its acceptance cone defined by the numerical aperture (see Equation 4.9). This maximum angle is 10° and it is, therefore, necessary to control the transverse displacements of the beam to avoid reaching this limit angle of incidence.

The beam displacement generated by the tip-tilt mirror can be minimised by correctly adapting its distance with respect to the previous secondary off-axis mirror. This optimum distance corresponds to the position that minimises the sum of the squares of the distances of the deflected beams from the main optical axis. Thus computing the evolution of the average rays distance from optical axes with distance from the secondary mirror we obtain a minimum at 45.96 mm from this mirror. Therefore placing the tip-tilt mirror at this exact position, should decrease the beam X and Z-shifts after reflection on the tip-tilt mirror. These transverse displacements are shown on Figure 6.2 where the maximum deviation is now smaller than 60 μm in the X direction and 90 μm in the Z direction. This enhances the superposition of the beams at the recombination stage to produce a deeper null.

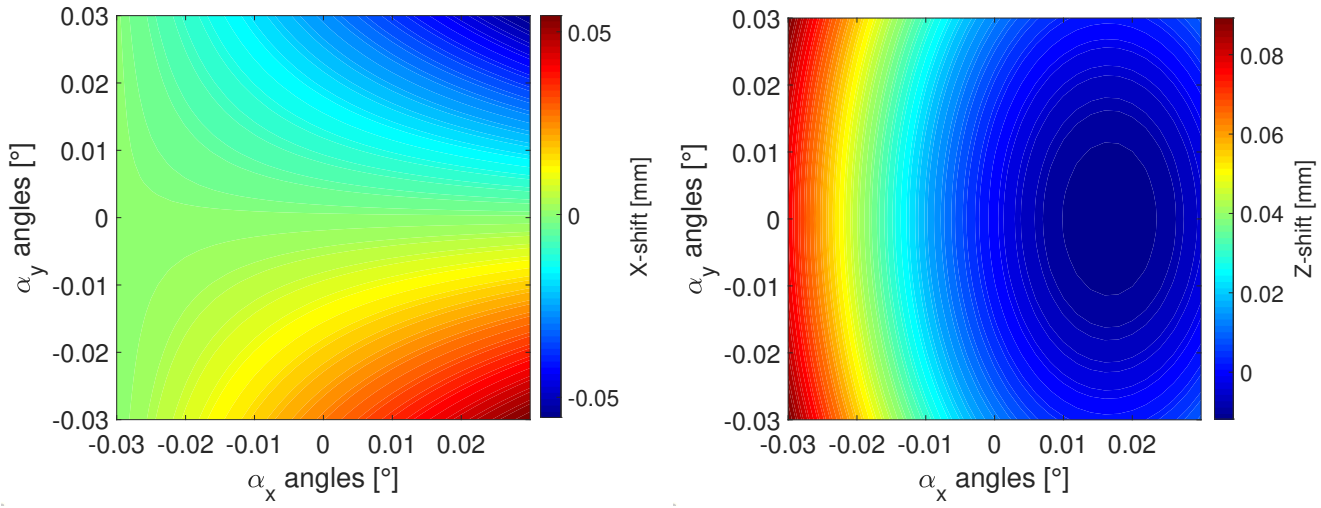

(a) Displacement along the X-axis. Positive values correspond to displacements along the +X direction.

(b) Displacement along the Z-axis. Positive values correspond to displacements along the +Z direction.

Figure 6.2: Beam's centroid displacement in function of pointing errors after tip-tilt mirror re-positioning.

Furthermore, this adaptation also stabilises the optical path length of the chief-ray which now varies from less than 1 μm as displayed in Figure 6.3.

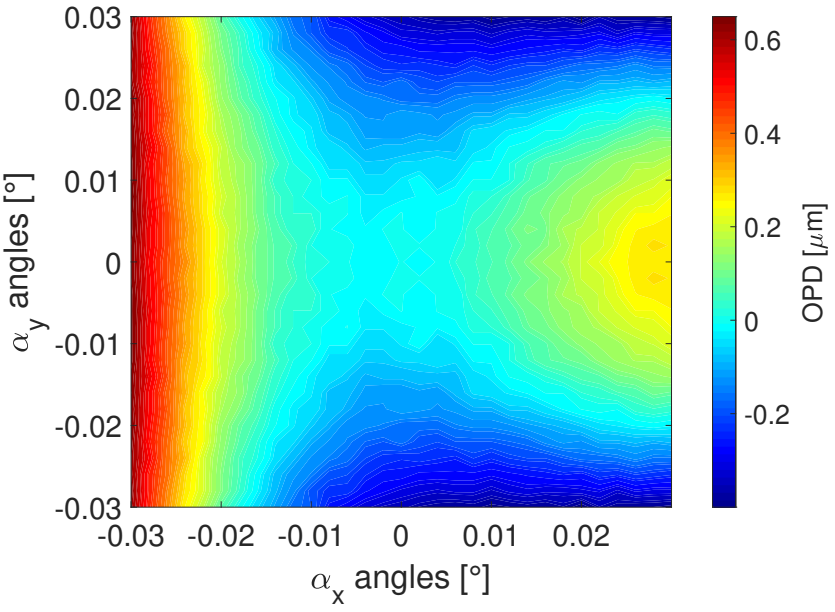

Figure 6.3: Chief ray optical path length variation in function of pointing errors after tip-tilt mirror re-positioning.

The less smooth variation of optical path length on the figure is due to the very small order of magnitude of the deformations which make them more sensitive to computation rounding errors. This structure may also be a consequence of the asphérisation of the surfaces generating thus a more irregular profile which can also impact the optical path length at smaller scales.

6.2 Further development

As a result of the different sensitivity measurements carried out, it appears that the main constraints of the system are related to the tip-tilt of the wavefront when pointing errors occur. Indeed, for aberrations of ± 0.03 degrees the sagittal and meridional rays exhibit optical path length variations of about 50 μm. Such a path length variation leads to a 1.37 degree of inclination of the wavefront (considering 4.35 mm beam width) with respect to the propagation axis that can strongly damage the recombination stage.

As a matter of fact, during recombination, the wavefronts must be as symmetrical as possible to maintain temporal coherence and thus sufficient null depth. This variation in optical path length is unfortunately not eradicable as it is a result of the intrinsic geometry of the telescope and more precisely of the primary and secondary mirror confocal configuration. As a matter of fact, *S. Chang* (2015 and 2016) [76] [77] show that the use of off-axis two-mirror telescopes with common parent mirrors axis as represented in Figure 6.4 does not get rid of the linear first-order astigmatism aberration.

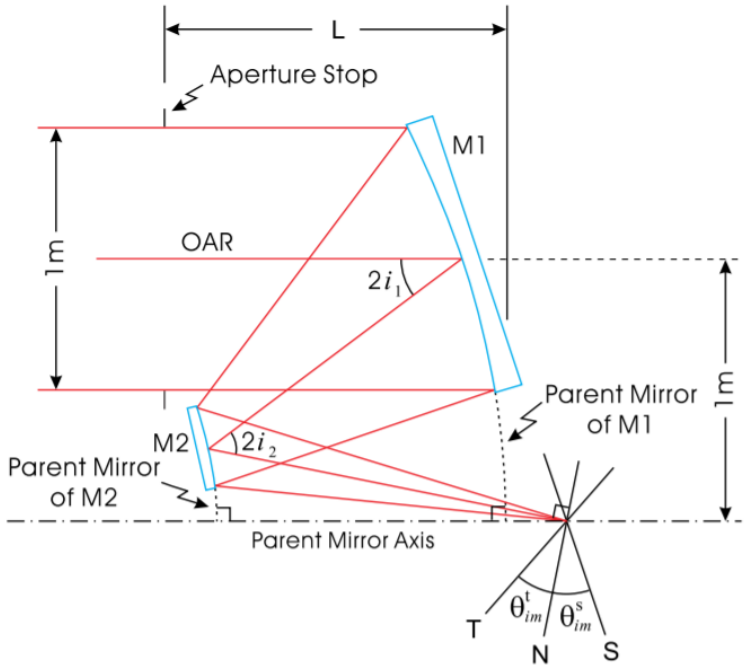

Figure 6.4: Representation of a two-mirror of axis telescope which does not suppress linear astigmatism aberration. The optical axis ray (OAR) is the ray passing by the centre of the aperture stop. It is reflected by an angle $2i_1$ on the primary mirror M1 and $2i_2$ on the secondary M2. Both surfaces have a common focus and are an extension of their parent mirror whose axis of symmetry is represented by the dash-doted line. The tangential, sagittal and normal to OAR image planes are denoted by T, S and N with θ^S_{im} and θ^T_{im} being their relative tilt with respect to the OAR image plane.[76]

To suppress such astigmatism, the telescope has to respect the following condition, also known as linear-astigmatism-free (LAF) condition [77],

$$(1 + m_1)m_2 \cdot tan(i_1) + (1 + m_2) \cdot tan(i_2) = 0, \tag{6.1}$$

where i_1 and i_2 denote the angle between the incoming ray and the local normal to the primary and secondary mirror surface respectively. The parameters m_1 and m_2 represent the ray magnification between two surfaces such that, in our case $m_1 = 0$ since the object is approximated at infinity and $m_2 = f_2/f_1$. The evolution of this relation between i_1 and i_2 for a two different magnifications ($m_2 = 0.1$ and $m_2 = 0.02$) is displayed on Figure 6.5.

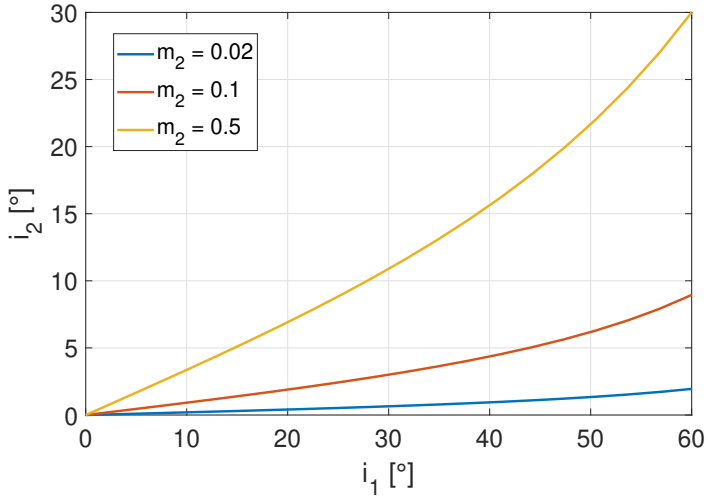

Figure 6.5: Representation of the LAF condition dependence between the incidence angle on the primary mirror i_1 and the incidence angle on the secondary mirror i_2.

In this work, the parameter m_2 is equal to 0.02 and the angle of incidence of the chief ray on the primary mirror surface is 45 degrees. This gives a value for the incidence angle on the secondary mirror of $i_2 = 1.12°$. Thus for a correct cancellation of the linear astigmatism, the ray must intercept the secondary mirror with an angle of 1.12 degree with respect to the surface normal. However, the design was considered such that this angle i_2 is equal to 45 degree, which means that the LAF condition is not verified for the system previously designed. To comply with the condition, the secondary mirror off-axis parabola has to be tilted by a certain angle, while maintaining the two parabolas confocal, similarly as in the illustration of Figure 6.6.

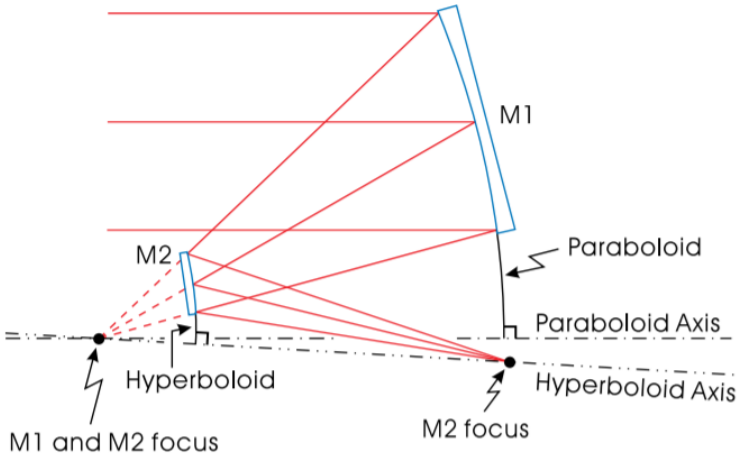

Figure 6.6: Representation of a two-mirror of axis telescope which does respect the LAF condition and therefore suppresses the linear astigmatism aberration. The two mirrors share a common focus but do not have the same parent mirror axis of symmetry.

However, such a small angle of reflection of 1.12 degrees is not practically feasible for the telescope considered in this work. As a matter of fact, the light beam would almost be reflected perpendicularly and therefore returned toward the extremities of the interferometer arm (where it originally comes from). Furthermore, such almost perpendicular reflection leads to difficulties

in arranging the reflective surfaces while avoiding to cause obstruction. Such arrangement limitations reduce the compactness of the design. This last criterion being one of the main threads of this study, leads to a different choice of design. Indeed, to respect the LAF condition while working with more acceptable reflection angles, it is necessary to consider a magnification closer to 1 and therefore mirrors with similar focal lengths.

This conclusion poses a real problem because mirrors with similar focal lengths do not allow a sufficiently large reduction in beam diameter for scientific measurements to be made. Thus, meeting this LAF condition requires the use of a third optical surface to collimate the beam to a reduced size. Furthermore, the magnification ratio of the first two mirrors must be close to 1, which leads to the use of a system of two confocal off-axis parabolas whose reflection angle must be minimised in order to guarantee good compactness. This tends towards the reduction of the beam at the end of the interferometer arm rather than at the centre as defined so far.

It is, therefore, the arrangement of the two off-axis confocal parabolas that causes this optical path length variation when rays arrive at different angles on the primary mirror. However, this LAF condition can also be ignored. Indeed, the current design can probably be adapted more simply to obtain wavefront distortions manageable by a deformable mirror. The current design requires the use of at least 2 deformable mirrors in series with an individual stroke of about 15 μm. Such accumulation of deformable surfaces is a functional solution although it is impractical. The most practical way to remove this wavefront distortion induced by field-of-view angles is therefore to add an extra surface to the telescope by making the design somewhat more complex. Another idea worth exploring is to change the orientation of the second parabola so that it propagates in the -Z direction, for instance. According to *C. Brückner, 2008*[78], playing with the orientation of the parabolas with respect to one another can impact the level of astigmatism and distortion of the system.

One must furthermore notice that increasing the diameter of the collimated beam does not correct these distortions, nor does changing the angle of reflection of the last parabola focusing in the fibre. A future study could therefore focus on improving this design by adding an optical surface and modifying the beam reduction. This would preferably be applied at the tip of the interferometer arm or the centre using an additional flat optical surface to redirect the beam towards the centre of the satellite. It should be noted that this is a solution that has been explored by the BETTII mission [79]. This project consists of an interferometer with an 8 m baseline, 20 cm telescope, and an operating wavelength range between 30 and 90 μm. Although the satellite is pointed with an accuracy of 1.5 arcsec, a depointing of 1 arcsec generates an OPL variation of 40 μm. This is of the order of the optical path variations obtained in this study for the sagittal and meridional rays.

Finally, if the design remains like it currently is, one way to make it operational, considering current technologies, is to increase the stability of the satellite. In fact, reducing the pointing errors to 0.02 degrees, for instance, gives rise to optical path length variations for the different sagittal and meridional rays of about 25 μm. To restore a flat wavefront, a deformable mirror with a stroke of 12.5-15 microns is therefore sufficient, which is much more reasonable given the current products available on the market.

Chapter 7

Conclusion

The motivation behind this report is based on the need to establish the limiting factors of stellar interferometry when applied on a satellite with a reduced design. This is done in order to reduce the development costs of a potential scientific mission. The objective of this work was therefore to evaluate the performance achievable by an interferometer of similar size to a PROBA-type satellite. This translates into the use of a 4 m baseline interferometer with 20 cm in diameter primary mirrors. Based on these dimensional constraints, the probability of detecting exoplanets as a function of the observation wavelength revealed that it is preferable to work with wavelengths between 1 and 5 μm. Considering these parameters, a choice of telescope design has been proposed with the main goal of simplifying the beam recombination process by minimising the number of surfaces required and the compactness of the design.

A review of previous missions and projects aiming at exoplanets detection through the use of nulling interferometry has given an idea of the types of constraints and performance achievable by each design. The choice of the interferometer structure was then made on the basis of these missions and the previously defined guidelines. The choice was finally made to reduce the beam using two off-axis confocal parabolas in order to avoid loss of light intensity due to obstruction. The primary mirror was defined to reflect the light directly towards the satellite centre. This allows the second mirror to be placed near the centre of the satellite and therefore avoids the use of additional relay optics when beam reduction is performed at the end of the arm. In addition, this allows the beam to pass through a focus before reaching the secondary mirror, which allows a field stop to be placed to limit the angles of the beams propagated inside the interferometer and thus reduce the stray light.

The system was then subjected to various pointing errors ranging from 0° to 0.03° with respect to the main optical axis. Chapter 4 is devoted to the study of the impact of these pointing errors on beam propagation. The deviation angle caused by alignment errors of the telescope after reflection on the secondary mirror is compensated by the addition of a tip-tilt mirror. This mirror must be able to tilt by 0.7 degrees in all directions from its initial position. The propagation angles are therefore all eliminated after reflection on the tip-tilt mirror. However, although the beams all propagate in the same direction, transverse displacement (perpendicular to the propagation axis) is generated. To minimise this error, the distance between the secondary mirror and the tip-tilt mirror is optimised to ensure that the two interferometer beams correctly superimpose at the recombination stage. This distance of 46 mm corresponds to the point on the optical axis where the sum of the squares of the distances of the deviated beams from this axis is minimum.

The focusing in a single mode fibre is also studied in Chapter 5 to perform modal filtering of the wavefront and thus reduce the sensitivity of the system to aberrations. I has been demonstrated that the coupling efficiency of the fibre is slightly affected by the range of alignment errors considered. The mirror realising the focus in the fibre being an off-axis parabola, it therefore focuses all parallel rays to the optical axis of its parent mirror to the same point. Thus, only a slight variation of f-number is generated. However, the coupling efficiency remains above 81% for the cut-off wavelength $\lambda_c = 2$ μm and the central wavelength $\lambda_{mid} = 3$ μm. The 4 μm wavelength remains above 71%.

We also study the evolution of the star's extinction profile as a function of the aberrations of the system expressed via the use of Zernike polynomials. We see that a Zernike polynomial strength greater than 0.01 radians increases the null depth (or the extinction level) above 10^{-6}. However, it is also shown that the use of a single-mode fibre makes it possible to reduce the sensitivity of the system to wavefront deformations. Indeed, an extinction of 10^{-6} is possible for Zernike coefficients strength up to 0.06 radians and an extinction of 10^{-5} allows to reach values of 0.11 radians. The coupling efficiency in the fiber can be computed based on these maximum aberration strengths. The coupling efficiency is very slightly impacted. The star extinction ratio is therefore a more sensitive parameter than the coupling efficiency to wavefront distortions.

Finally, the system faces a significant astigmatism generating differences in optical paths between the sagittal and meridional rays of 50 μm. This value seems to be difficult to compensate by a deformable mirror with nowadays technology. However, two deformable mirrors are sufficient. If we consider the system equipped with only a single deformable mirror capable of correcting optical path differences across the pupil of ± 30 μm (therefore being able to deform by ± 15 μm), then the maximum authorised pointing errors are 0.02 arcsec. To reduce the sensitivity of the system to larger fields of view, an additional optical surface must be added (making the design slightly more complex). This surface can be placed after the secondary mirror so that the latter is no longer used for collimation of the light beam. With such an additional surface, the system should be able to get rid of linear astigmatism (first order) and therefore decrease its sensitivity to pointing errors.

List of acronyms

ADCS Attitude Determination and Control System. 42

AIC Achromatic Interferential Coronograph. iii, 16, 17, 20, 75

CHARA Center for High Angular Resolution Astronomy. 10

CHEOPS CHaracterising ExOPlanet Satellite. 4

CoRoT Convection Rotation and planetary Transits. 3

FLUOR (Fiber Linked Unit for Optical Recombination. 10

HATNet Hungarian Automated Telescope Network. 3

LBTI Large Binocular Telescope Interferometer. 10

MATISSE Multi-Aperture mid-Infrared SpectroScopic Experiment. 10

NOMIC Nulling Optimized Mid-Infrared Camera. 10

OPD Optical Path Difference. 20

OPL Optical Path Length. 68–70, 84

PROBA PRoject for On-Board Autonomy. 32, 34, 42, 64

SMF Single Mode Fibre. 54

SPECULOOS Search for Planets EClipsing ULtra-cOOl Stars. 3

TESS Transiting Exoplanet Survey Satellite. 4

TRAPPIST TRAnsiting Planets and PlanetesImals Small Telescope. 3

VLTI Very Large Telescope Interferometer. 10

Appendix A

Appendices

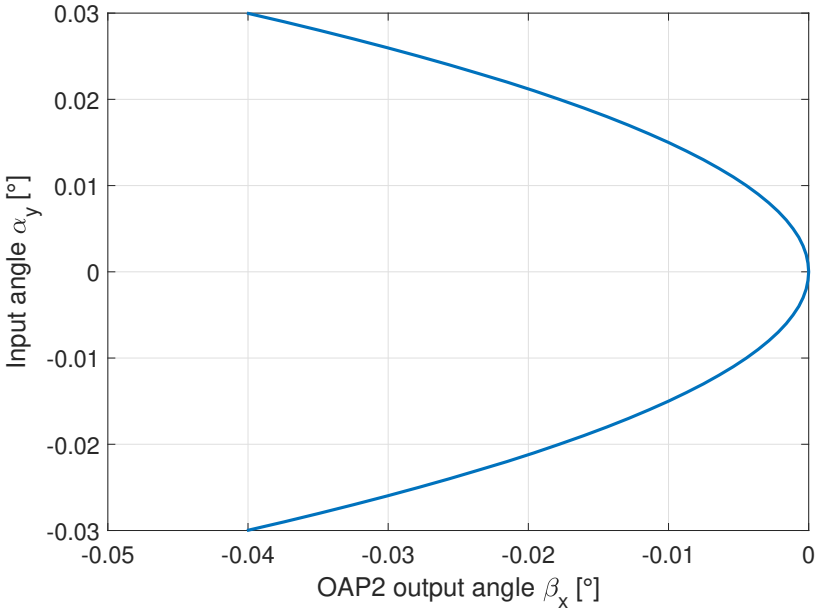

Figure A.1: Pointing error direction cross dependence

i	n	m	Z_i	Description
1	0	0	1	Piston
2	1	-1	$2rcos(\theta)$	Horizontal tilt
3	1	1	$2rsin(\theta)$	Lateral tilt
4	2	0	$\sqrt{3}(2r^2-1)$	Defocus
5	2	-2	$\sqrt{6}r^2sin(2\theta)$	Astigmatism
6	2	2	$\sqrt{6}r^2cos(2\theta)$	Astigmatism
7	3	-1	$\sqrt{8}(3r^3-2r)sin(\theta)$	Coma
8	3	1	$\sqrt{8}(3r^3-2r)cos(\theta)$	Coma
9	3	-3	$\sqrt{8}r^3sin(3\theta)$	Trefoil
10	3	3	$\sqrt{8}r^3cos(3\theta)$	Trefoil
11	4	0	$\sqrt{5}(6r^4-6r^2+1)$	Spherical
12	4	-2	$\sqrt{10}(4r^4-3r^2)cos(2\theta)$	Astigmatism (2nd order)

Table A.1: List of the 12 first Zernike polynomials according to Noll ordering.[55]

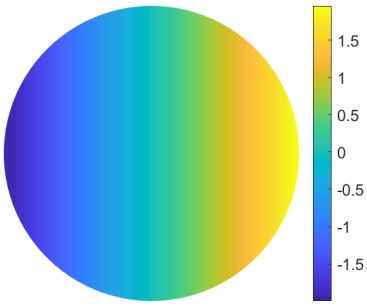

(a) Z_2, n=1, m=-1

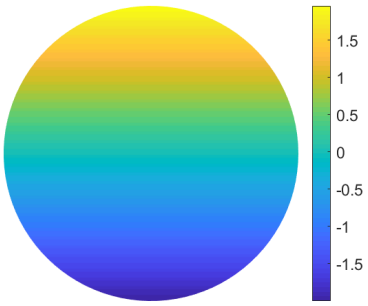

(b) Z_3, n=1, m=1

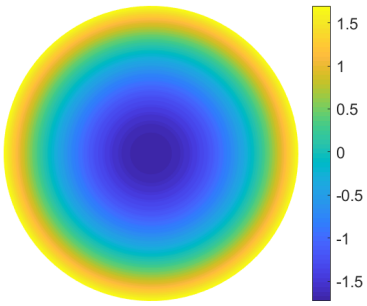

(c) Z_4, n=2, m=0

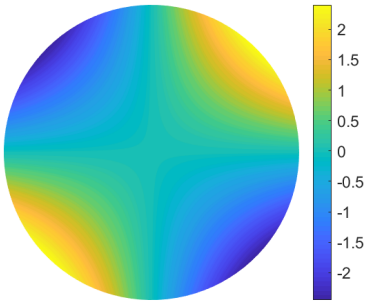

(d) Z_5, n=2, m=-1

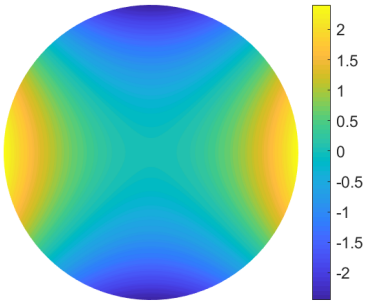

(e) Z_6, n=2, m=1

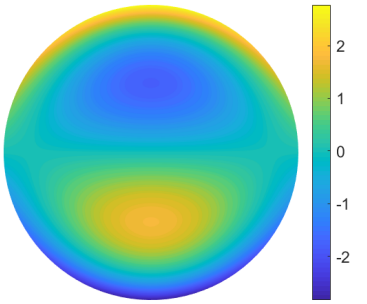

(f) Z_7, n=3, m=-1

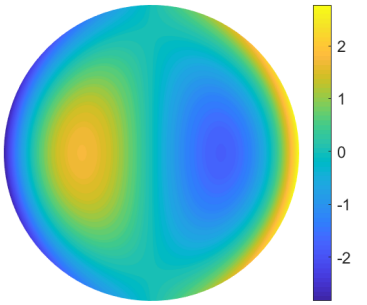

(g) Z_8, n=3, m=1

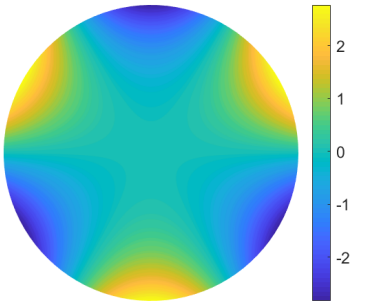

(h) Z_9, n=3, m=-3

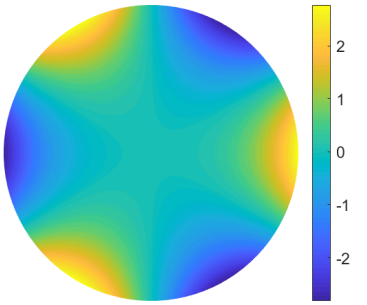

(i) Z_10, n=3, m=3

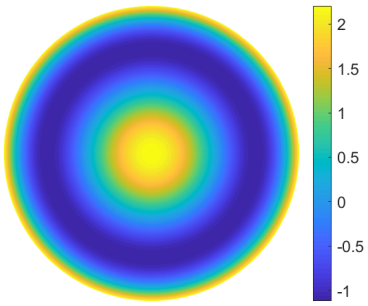

(j) Z_11, n=4, m=0

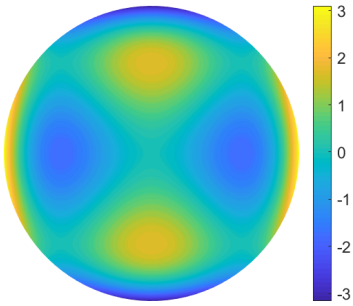

(k) Z_12, n=4, m=-2

Figure A.2: Graphical representation of the 12 first Zernike polynomials across a circular pupil.

References

[1] N. C. Administrator. *Viking Mission Overview*. 2012. https://www.nasa.gov/redplanet/viking.html (cit. on p. 1).

[2] A. Wolszczan and D. Frail. "A planetary system around the millisecond pulsar PSR1257 + 12". In: *Nature* 355 (1992), pp. 145–147 (cit. on p. 1).

[3] M. Mayor and D. Queloz. "A Jupiter-mass companion to a solar-type star". In: *Nature* 378.6555 (Nov. 1995), pp. 355–359. DOI: 10.1038/378355a0. https://doi.org/10.1038/378355a0 (cit. on p. 1).

[4] M. Johnson. *Kepler Mission Overview*. 2018. https://www.nasa.gov/mission_pages/kepler/overview/index.html (cit. on pp. 1, 4).

[5] *NASA Exoplanet Exploration:5 Ways to Find a Planet*. https://exoplanets.nasa.gov/alien-worlds/ways-to-find-a-planet/ (cit. on pp. 2, 3, 5).

[6] K. C. Schlaufman. "Evidence of an Upper Bound on the Masses of Planets and Its Implications for Giant Planet Formation". In: *The Astrophysical Journal* 853.1 (Jan. 2018), p. 37. DOI: 10.3847/1538-4357/aa961c. https://doi.org/10.3847/1538-4357/aa961c (cit. on p. 2).

[7] R. Cardenas. "FINDING NEW WORLDS: DIDIER QUELOZ AND MICHEL MAYOR'S NOBEL PRIZE IN PHYSICS 2019". In: *Revista Cubana de Fisica* 36 (Dec. 2019), p. 152 (cit. on p. 2).

[8] D. Fischer et al. *Exoplanet Detection Techniques*. https://www2.mpia-hd.mpg.de/homes/ppvi/chapter/fischer.pdf (cit. on pp. 2, 3, 5).

[9] *The Transit Photometry Method*. https://www.planetary.org/articles/down-in-front-the-transit-photometry-method (cit. on p. 3).

[10] N. E. Archive. *Exoplanet and Candidate Statistics*. https://exoplanetarchive.ipac.caltech.edu/docs/counts_detail.html (cit. on p. 3).

[11] M. Deleuil and M. Fridlund. "CoRoT: The First Space-Based Transit Survey to Explore the Close-in Planet Population". In: *Handbook of Exoplanets* (2018), pp. 1135–1158. DOI: 10.1007/978-3-319-55333-7_79. http://dx.doi.org/10.1007/978-3-319-55333-7_79 (cit. on p. 4).

[12] E. S. Agency. *Detecting exoplanets with microlensing*. http://www.esa.int/ESA_Multimedia/Images/2019/02/Detecting_exoplanets_with_microlensing (cit. on p. 4).

[13] I. A. Bond et al. "OGLE 2003-BLG-235/MOA 2003-BLG-53: A Planetary Microlensing Event". In: *The Astrophysical Journal* 606.2 (Apr. 2004), pp. L155–L158. DOI: 10.1086/420928. https://doi.org/10.1086/420928 (cit. on p. 4).

[14] A. Mallama, B. Krobusek, and H. Pavlov. "Comprehensive wide-band magnitudes and albedos for the planets, with applications to exo-planets and Planet Nine". In: *Icarus* 282 (2017), pp. 19–33. ISSN: 0019-1035. DOI: https://doi.org/10.1016/j.icarus.2016.09.023. https://www.sciencedirect.com/science/article/pii/S0019103516301014 (cit. on p. 5).

[15] D. Defrère. "Space Interferometry Basics, history, configuration, design issues, prospects." In: *SPAT0073-1: Space Optics, 2019-2020 (Pr. J. Loicq)* (2019) (cit. on pp. 6, 7).

[16] P. Labeye. "Composants optiques intégrés pour l'Interférométrie astronomique". Theses. Institut National Polytechnique de Grenoble - INPG, Feb. 2008. https://tel.archives-ouvertes.fr/tel-00870937 (cit. on p. 8).

[17] R. N. BRACEWELL. "Detecting nonsolar planets by spinning infrared interferometer". In: *Nature* 274.5673 (Aug. 1978), pp. 780–781. DOI: 10.1038/274780a0. https://doi.org/10.1038/274780a0 (cit. on p. 8).

[18] O. Absil. "Astrophysical studies of extrasolar planetary systems using infrared interferometric techniques". In: *Institut d'Astrophysique et de Géophysique de Liège* (Mar. 2006) (cit. on pp. 8, 11).

[19] C. Dandumont et al. "Exoplanet detection yield of a space-based Bracewell interferometer from small to medium satellites". In: *Journal of Astronomical Telescopes, Instruments, and Systems* 6.03 (Sept. 2020). DOI: 10.1117/1.jatis.6.3.035004. https://doi.org/10.1117/1.jatis.6.3.035004 (cit. on pp. 9, 34).

[20] V. C. du Foresto et al. "FLUOR fibered beam combiner at the CHARA array". In: *Interferometry for Optical Astronomy II*. Ed. by W. A. Traub. SPIE, Feb. 2003. DOI: 10.1117/12.459942. https://doi.org/10.1117/12.459942 (cit. on p. 10).

[21] M. Benisty et al. "An integrated optics beam combiner for the second generation VLTI instruments". In: *Astronomy & Astrophysics* 498.2 (Mar. 2009), pp. 601–613. DOI: 10.1051/0004-6361/200811083. https://doi.org/10.1051/0004-6361/200811083 (cit. on p. 10).

[22] https://sites.google.com/a/lbto.org/lbti/home/cameras (cit. on p. 10).

[23] C. Paladini. "MATISSE User Manual". In: 4 (Mar. 2020). https://www.eso.org/sci/facilities/paranal/instruments/matisse/doc/VLT-MAN-ESO-289268_P105.pdf (cit. on p. 10).

[24] Schöller, M., Wilhelm, R., and Koehler, B. "Modeling the imaging process in optical stellar interferometers". In: *Astron. Astrophys. Suppl. Ser.* 144.3 (2000), pp. 541–552. DOI: 10.1051/aas:2000229. https://doi.org/10.1051/aas:2000229 (cit. on p. 10).

[25] O. Lay. "Systematic errors in nulling interferometers". In: *Optical Society of America* (2004) (cit. on p. 12).

[26] M. Ollivier. "Contribution a la recherche d'exoplanetes coronographie interferentielle pour la mission darwin". In: (1999). 1999PA112392, 223 p. http://www.theses.fr/1999PA112392 (cit. on p. 12).

[27] B. Chazelas. "Contribution à l'étude de l'interférométrie annulante, pour la recherche d'exoplanètes". Theses. Université Paris Sud - Paris XI, Jan. 2007. https://tel.archives-ouvertes.fr/tel-00140623 (cit. on pp. 12, 13).

[28] B. Mennesson, M. Ollivier, and C. Ruilier. "Use of single-mode waveguides to correct the optical defects of a nulling interferometer". In: *J. Opt. Soc. Am. A* 19.3 (Mar. 2002), pp. 596–602. DOI: 10.1364/JOSAA.19.000596. http://josaa.osa.org/abstract.cfm?URI=josaa-19-3-596 (cit. on pp. 13, 77).

[29] E. Serabyn. "Nulling interferometry: symmetry requirements and experimental results". In: *Interferometry in Optical Astronomy*. Ed. by P. J. Lena and A. Quirrenbach. Vol. 4006. International Society for Optics and Photonics. SPIE, 2000, pp. 328–339. DOI: 10.1117/12.390223. https://doi.org/10.1117/12.390223 (cit. on pp. 13, 19, 20).

[30] L. Escarrat. "Contribution au mode coronographique de la mission Darwin". In: (Nov. 2003). https://tel.archives-ouvertes.fr/tel-00011592 (cit. on pp. 14, 16, 17, 75, 77).

[31] J. D. Monnier. "Optical interferometry in astronomy". In: *Reports on Progress in Physics* 66.5 (Apr. 2003), pp. 789–857. ISSN: 1361-6633. DOI: 10.1088/0034-4885/66/5/203. http://dx.doi.org/10.1088/0034-4885/66/5/203 (cit. on p. 21).

[32] R. Davies and M. Kasper. "Adaptive Optics for Astronomy". In: *Annual Review of Astronomy and Astrophysics* 50.1 (2012), pp. 305–351. DOI: 10.1146/annurev-astro-081811-125447. eprint: https://doi.org/10.1146/annurev-astro-081811-125447. https://doi.org/10.1146/annurev-astro-081811-125447 (cit. on p. 21).

[33] I. Klein, M. Guelman, and S. G. Lipson. "Space-based intensity interferometer". In: *Appl. Opt.* 46.20 (July 2007), pp. 4237–4247. DOI: 10.1364/AO.46.004237. http://ao.osa.org/abstract.cfm?URI=ao-46-20-4237 (cit. on p. 21).

[34] L. project. *LIFE space mission*. https://www.life-space-mission.com/outreach/ (cit. on pp. 22, 23).

[35] S. P. Quanz et al. *Large Interferometer For Exoplanets (LIFE): I. Improved exoplanet detection yield estimates for a large mid-infrared space-interferometer mission*. 2021. arXiv: 2101.07500 [astro-ph.EP] (cit. on p. 23).

[36] W. Danchia and R. Barry. "The Fourier-Kelvin Stellar Interferometer (FKSI) — Infrared Detection and Characterization of Exozodiacal Dust to Super-Earths: A Progress Report". In: *SPIE: Optical and Infrared Interferometry II* 7734 (2010). DOI: 10.1117/12.858129 (cit. on pp. 23–25).

[37] A. Léger et al. "Could We Search for Primitive Life on Extrasolar Planets in the Near Future?" In: *Icarus* 123.2 (1996), pp. 249–255. ISSN: 0019-1035. DOI: https://doi.org/10.1006/icar.1996.0155. https://www.sciencedirect.com/science/article/pii/S0019103596901554 (cit. on pp. 25, 26).

[38] E. S. Agency. *Darwin overview*. http://www.esa.int/ESA_Multimedia/Images/2019/02/Detecting_exoplanets_with_microlensing (cit. on p. 26).

[39] P. R. Lawson and W. Traub. *Earth-Like Exoplanets:The Science of NASA's Navigator Program*. NASA STI/Recon Technical Report N. Oct. 2006 (cit. on pp. 26, 27).

[40] P. R. Lawson et al. *Terrestrial Planet Finder Interferometer Science Working Group Report*. NASA STI/Recon Technical Report N. Mar. 2007 (cit. on pp. 26, 27).

[41] O. P. Lay, S. R. Martin, and S. L. Hunyadi. "Planet-finding performance of the TPF-I Emma architecture". In: *Techniques and Instrumentation for Detection of Exoplanets III*. Ed. by D. R. Coulter. Vol. 6693. International Society for Optics and Photonics. SPIE, 2007, pp. 97–105. DOI: 10.1117/12.732230. https://doi.org/10.1117/12.732230 (cit. on pp. 27, 28).

[42] P. Lawson et al. "Terrestrial Planet Finder Interferometer (TPF-1) Whitepaper for the AAAC Exoplanet Task Force". In: (Apr. 2007), p. 9 (cit. on p. 28).

[43] F. Cassaing et al. "Towards a laboratory breadboard for PEGASE, the DARWIN pathfinder". In: *International Conference on Space Optics — ICSO 2006*. Ed. by E. Armandillo, J. Costeraste, and N. Karafolas. Vol. 10567. International Society for Optics and Photonics. SPIE, 2017, pp. 138–144. DOI: 10.1117/12.2308162. https://doi.org/10.1117/12.2308162 (cit. on p. 29).

[44] ESA. *COSMIC VISION 2015-2025 PROPOSALS*. https://sci.esa.int/s/wQejlkw (cit. on p. 29).

[45] M. Ollivier et al. "PEGASE, an infrared interferometer to study stellar environments and low mass companions around nearby stars". In: (2009). DOI: 10.1007/s10686-008-9133-6 (cit. on p. 29).

[46] M. C. Noecker et al. "Cold interferometric nulling demonstration in space (CINDIS)". In: *Techniques and Instrumentation for Detection of Exoplanets*. Ed. by D. R. Coulter. Vol. 5170. International Society for Optics and Photonics. SPIE, 2003, pp. 113–128. DOI: 10.1117/12.508013 (cit. on pp. 30, 31).

[47] F. Mackenzie and A. Lerman. "Heat Balance of the Atmosphere and Carbon Dioxide". In: vol. 25. Jan. 2006, pp. 61–88. ISBN: 978-1-4020-4044-3. DOI: 10.1007/1-4020-4238-8_3 (cit. on p. 33).

[48] D. Des Marais et al. "Remote Sensing of Planetary Properties and Biosignatures on Extrasolar Terrestrial Planets". In: *Astrobiology* 2 (Feb. 2002), pp. 153–81. DOI: 10.1089/15311070260192246 (cit. on p. 33).

[49] L. Shifano. "Développement d'un interféromètre spatial pour la détection et la caractérisation d'exoplanètes". In: (June 2018). http://hdl.handle.net/2268.2/5548 (cit. on p. 38).

[50] C. Brückner, G. Notni, and A. Tünnermann. "Optimal arrangement of 90° off-axis parabolic mirrors in THz setups". In: *Optik - International Journal for Light and Electron Optics* 121 (Jan. 2010), pp. 113–119. DOI: 10.1016/j.ijleo.2008.05.024 (cit. on p. 39).

[51] S. R. Starin and J. Eterno. "Attitude Determination and Control Systems". In: (Jan. 2011). DOI: 20110007876 (cit. on p. 41).

[52] G. Kerschen and V. Broun. "AERO0025-1: Satellite engineering". In: (2020). https://www.programmes.uliege.be/cocoon/20202021/cours/AERO0025-1.html (cit. on p. 42).

[53] S. Dibartolomeo. "Observation Strategy: Interferometric Small Sat to Observe Exoplanets". In: (2019). http://hdl.handle.net/2268.2/6754 (cit. on p. 42).

[54] F. Aït Hocine. "Coupling of a single-mode fiber with a deformable mirror in a space-based nulling interferometer". In: (2020). http://hdl.handle.net/2268.2/10470 (cit. on pp. 45, 47, 54).

[55] R. J. Noll. "Zernike polynomials and atmospheric turbulence∗". In: *J. Opt. Soc. Am.* 66.3 (Mar. 1976), pp. 207–211. DOI: 10.1364/JOSA.66.000207. http://www.osapublishing.org/abstract.cfm?URI=josa-66-3-207 (cit. on pp. 46, III).

[56] C. B. Hogge and R. R. Butts. "Effects of using different wavelengths in wave-front sensing and correction". In: *J. Opt. Soc. Am.* 72.5 (May 1982), pp. 606–609. DOI: 10.1364/JOSA.72.000606. http://www.osapublishing.org/abstract.cfm?URI=josa-72-5-606 (cit. on p. 47).

[57] *Adaptive Optics in Astronomy*. Cambridge University Press, 1999. DOI: 10.1017/CBO9780511525179 (cit. on p. 48).

[58] J. Feinleib, S. G. Lipson, and P. F. Cone. "Monolithic piezoelectric mirror for wavefront correction". In: *Applied Physics Letters* 25.5 (1974), pp. 311–313. DOI: 10.1063/1.1655486. https://doi.org/10.1063/1.1655486 (cit. on p. 48).

[59] P.-Y. Madec. "Overview of deformable mirror technologies for adaptive optics and astronomy". In: *Adaptive Optics Systems III*. Ed. by B. L. Ellerbroek, E. Marchetti, and J.-P. Véran. Vol. 8447. International Society for Optics and Photonics. SPIE, 2012, pp. 22–39. DOI: 10.1117/12.924892. https://doi.org/10.1117/12.924892 (cit. on pp. 48, 49).

[60] T. Bifano, S. Cornelissen, and P. Bierden. "MEMS deformable mirrors in astronomical adaptive optics". In: *1st AO4ELT conference - Adaptive Optics for Extremely Large Telescopes*. Ed. by Array. 2010, p. 06003. DOI: 10.1051/ao4elt/201006003. https://doi.org/10.1051/ao4elt/201006003 (cit. on p. 49).

[61] E. S. Douglas et al. "Wavefront sensing in space: flight demonstration II of the PICTURE sounding rocket payload". In: *Journal of Astronomical Telescopes, Instruments, and Systems* 4.1 (2018), pp. 1–10. DOI: 10.1117/1.JATIS.4.1.019003. https://doi.org/10.1117/1.JATIS.4.1.019003 (cit. on p. 49).

[62] G. Allan et al. *The Deformable Mirror Demonstration Mission (DeMi) CubeSat: optomechanical design validation and laboratory calibration*. 2018. arXiv: 1807.02649 [astro-ph.IM] (cit. on p. 49).

[63] M. Campbell. "Adaptive optic demonstrators for extremely large telescopes". PhD thesis. June 2011 (cit. on p. 51).

[64] J. W. Beletic et al. "A new CCD designed for curvature wavefront sensing". In: *Optical Detectors For Astronomy II: State-of-the-Art at the Turn of the Millennium*. Ed. by P. Amico and J. W. Beletic. Dordrecht: Springer Netherlands, 2000, pp. 283–309. ISBN: 978-94-011-4361-5. DOI: 10.1007/978-94-011-4361-5_28. https://doi.org/10.1007/978-94-011-4361-5_28 (cit. on p. 52).

[65] I. Shatokhina, V. Hutterer, and R. Ramlau. "Review on methods for wavefront reconstruction from pyramid wavefront sensor data". In: *Journal of Astronomical Telescopes, Instruments, and Systems* 6.1 (2020), pp. 1–39. DOI: 10.1117/1.JATIS.6.1.010901. https://doi.org/10.1117/1.JATIS.6.1.010901 (cit. on p. 52).

[66] V. Hutterer, R. Ramlau, and I. Shatokhina. "Real-time adaptive optics with pyramid wavefront sensors: part I. A theoretical analysis of the pyramid sensor model". In: *Inverse Problems* 35 (2018), p. 045007 (cit. on p. 52).

[67] J. Hayes. *The Fiber Optics Technician's Manual*. 3rd edition. Delmar Cengage Learning, 2005. ISBN: 1418028754 (cit. on p. 53).

[68] P. Schäfter + Kirchhoff GmbH - Optics and Metrology. *TYPICAL EFFECTIVE NUMERICAL APERTURES*. https://www.sukhamburg.com/support/technotes/fiberoptics/cablebasics/NAefftypvalues.html (cit. on p. 54).

[69] E.-G. Neumann. "Single-Mode Fibers: Fundamentals". In: 57 (1988). DOI: 10.1007/978-3-540-48173-7 (cit. on p. 55).

[70] S. Shaklan and F. Roddier. "Coupling starlight into single-mode fiber optics". In: *Appl. Opt.* 27.11 (June 1988), pp. 2334–2338. DOI: 10.1364/AO.27.002334. http://ao.osa.org/abstract.cfm?URI=ao-27-11-2334 (cit. on p. 55).

[71] J. Janssen. "A Study of Degraded Light Coupling into Single-mode Bers". In: 2007 (cit. on p. 55).

[72] C. Fayt. "Study of waveguides for achromatic pi-phase shift in the region between 1 and 5 microns." In: (June 2021) (cit. on p. 59).

[73] A. Dubuc. "Design of a reflective infrared spectrograph for exoplanet spectroscopy". In: (June 2021) (cit. on p. 59).

[74] T. P. Group. *Piezo Flexure Tilting Mirrors.* https://www.pifrance.fr/fr/produits/platines-de-nanopositionnement-a-structure-deformable/plateformes-tip-tilt-piezo-pour-miroirs/ (cit. on p. 67).

[75] M. Newport. *Optical Delay Lines.* https://www.newport.com.cn/f/delay-line-stages (cit. on p. 70).

[76] S. Chang. "Linear astigmatism of confocal off-axis reflective imaging systems with N-conic mirrors and its elimination". In: *J. Opt. Soc. Am. A* 32.5 (May 2015), pp. 852–859. DOI: 10.1364/JOSAA.32.000852. http://josaa.osa.org/abstract.cfm?URI=josaa-32-5-852 (cit. on pp. 81, 82).

[77] S. Chang. "Compact wide-field off-axis two-mirror system with field corrector". In: *Novel Optical Systems Design and Optimization XIX*. Ed. by A. J. Davis, C. F. Hahlweg, and J. R. Mulley. SPIE, Sept. 2016. DOI: 10.1117/12.2238308. https://doi.org/10.1117/12.2238308 (cit. on pp. 81, 82).

[78] C. Brückner, G. Notni, and A. Tünnermann. "Optimal arrangement of 90° off-axis parabolic mirrors in THz setups". In: *Optik - International Journal for Light and Electron Optics* 121 (Jan. 2010), pp. 113–119. DOI: 10.1016/j.ijleo.2008.05.024 (cit. on p. 84).

[79] M. J. Rizzo et al. "Building an interferometer at the edge of space: pointing and phase control system for BETTII". In: *Space Telescopes and Instrumentation 2014: Optical, Infrared, and Millimeter Wave*. Ed. by J. M. O. Jr. et al. Vol. 9143. International Society for Optics and Photonics. SPIE, 2014, pp. 1050–1061. DOI: 10.1117/12.2055016. https://doi.org/10.1117/12.2055016 (cit. on p. 84).

[80] QuestTel. *Numerical aperture in fiber optics.* https://questtel.com/wiki/numerical-aperture-in-fiber-optics.

[81] J. Sasián. "Method of confocal mirror design". In: *Optical Engineering* 58.01 (Jan. 2019), p. 1. DOI: 10.1117/1.oe.58.1.015101. https://doi.org/10.1117/1.oe.58.1.015101.